Compressed Sensing Accelerated Magnetic Resonance Spectroscopic Imaging

by

Rohini Vidya Shankar

A Dissertation Presented in Partial Fulfillment
of the Requirements for the Degree
Doctor of Philosophy

Approved July 2016 by the
Graduate Supervisory Committee:

Vikram D. Kodibagkar, Chair
James Pipe
Rosalind Sadleir
John Chang
David Frakes

ARIZONA STATE UNIVERSITY

August 2016

ABSTRACT

Magnetic resonance spectroscopic imaging (MRSI) is a valuable technique for assessing the *in vivo* spatial profiles of metabolites like N-acetylaspartate (NAA), creatine, choline, and lactate. Changes in metabolite concentrations can help identify tissue heterogeneity, providing prognostic and diagnostic information to the clinician. The increased uptake of glucose by solid tumors as compared to normal tissues and its conversion to lactate can be exploited for tumor diagnostics, anti-cancer therapy, and in the detection of metastasis. Lactate levels in cancer cells are suggestive of altered metabolism, tumor recurrence, and poor outcome. A dedicated technique like MRSI could contribute to an improved assessment of metabolic abnormalities in the clinical setting, and introduce the possibility of employing non-invasive lactate imaging as a powerful prognostic marker.

However, the long acquisition time in MRSI is a deterrent to its inclusion in clinical protocols due to associated costs, patient discomfort (especially in pediatric patients under anesthesia), and higher susceptibility to motion artifacts. Acceleration strategies like compressed sensing (CS) permit faithful reconstructions even when the k-space is undersampled well below the Nyquist limit. CS is apt for MRSI as spectroscopic data are inherently sparse in multiple dimensions of space and frequency in an appropriate transform domain, for e.g. the wavelet domain. The objective of this research was three-fold: firstly on the preclinical front, to prospectively speed-up spectrally-edited MRSI using CS for rapid mapping of lactate and capture associated changes in response to therapy. Secondly, to retrospectively evaluate CS-MRSI in pediatric patients scanned for various brain-related concerns. Thirdly, to implement prospective CS-MRSI

acquisitions on a clinical magnetic resonance imaging (MRI) scanner for fast spectroscopic imaging studies. Both phantom and *in vivo* results demonstrated a reduction in the scan time by up to 80%, with the accelerated CS-MRSI reconstructions maintaining high spectral fidelity and statistically insignificant errors as compared to the fully sampled reference dataset. Optimization of CS parameters involved identifying an optimal sampling mask for CS-MRSI at each acceleration factor. It is envisioned that time-efficient MRSI realized with optimized CS acceleration would facilitate the clinical acceptance of routine MRSI exams for a quantitative mapping of important biomarkers.

TABLE OF CONTENTS

LIST OF FIGURES

CHAPTER 1

MAGNETIC RESONANCE SPECTROSCOPIC IMAGING

1.1 Introduction

Magnetic resonance spectroscopic imaging (MRSI, also known as chemical shift imaging or CSI), which was first introduced by Brown et al [1] and later developed further by Maudsley et al [2], is a key non-invasive imaging technique for measuring and monitoring metabolic profiles *in vivo* in conjunction with other anatomical and functional sequences [3, 4]. MRSI can identify and quantify the metabolic differences between healthy and diseased tissue, thus, providing prognostic and diagnostic information to the clinician that could improve treatment strategies. Proton (^{1}H) MR spectroscopy has been extensively employed to probe tissue metabolism in tumor models of the brain, breast and prostate over the last couple of decades [5-14]. For example, increased levels of choline and reduced NAA (N-acetyl aspartate) are typically seen in brain tumors [7, 8, 12], while malignant breast lesions express raised concentrations of total choline [5, 6, 9, 10]. Cancers of the prostate are associated with decreased citrate levels along with an increase in choline, phosphocholine, lactate, and phosphoethanoamine [11, 13, 14].

MRSI can also establish direct correlations with anatomical imaging and can be linked to physiological measurements such as perfusion and diffusion imaging [15]. While *in vivo* MRSI has been demonstrated with other nuclei, ^{1}H MRSI is the spectroscopic imaging technique of choice for imaging in the clinic because of greater hydrogen abundance and commercially available equipment, as compared to ^{13}C, ^{31}P, and ^{23}Na MRSI. Nevertheless, these other nuclei are also very useful in investigating specific

1

metabolic processes [16-20]. Although MRSI can monitor clinically relevant biomolecules, its clinical use is limited by the extremely long acquisition time, limited spatial coverage, and low signal-to-noise ratio (SNR).

1.2 Localization Techniques in MRS

Localization methods in MR spectroscopy utilize reference anatomical images from MRI to define the desired volume of interest (VOI) for spatially selective acquisition of spectra [21]. Ideal MRS pulse sequences should acquire good quality spectra from within the VOI, with minimal interference from unwanted signals outside the desired volume. However, the *in vivo* detection and accurate quantification of metabolites is complicated by several factors such as the presence of huge resonances from water and lipid, low spectral resolution due to heterogeneity in the B_0 field distribution, and low signal to noise ratio (SNR). MRS localization techniques in the clinic rely on the B_0 gradients (phase encoding and slice selection) employed in MRI to achieve spatial selectivity, along with spatial saturation bands and signal cancellation procedures for effective outer volume suppression [21].

1.2.1 Single Voxel Spectroscopy

In single voxel spectroscopy (SVS), the desired tissue VOI is defined by the gradient selection of three orthogonal planes or slices. A single spectrum is then acquired from the selected VOI. This localization along three dimensions can be achieved using the point resolved spectroscopy (PRESS) and stimulated echo acquisition mode (STEAM) pulse sequences. Both techniques use three frequency selective radio

2

frequency (RF) pulses to excite the volume of interest, as depicted in Figure 1.1. However, the timing diagram of the two sequences, along with the flip angles of the RF pulses and placement of the spoiler gradients are different, even though both share the principles of volume selection [21]. The two sequences also differ in the achievable SNR ($SNR_{STEAM} = SNR_{PRESS}/2$), the minimum TE that can realized, water suppression, artifacts resulting from chemical shift, and sensitivity to motion. Additional chemical shift selective saturation (CHESS) pulses are employed to suppress the huge interfering signals from water and lipid.
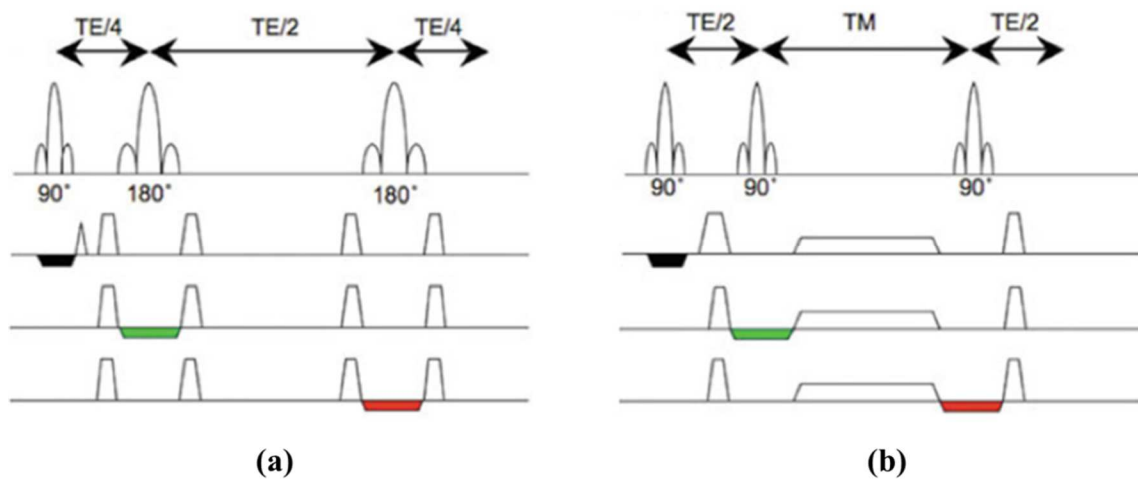
Figure 1.1 SVS localization sequences. (a) The PRESS MRS sequence timing diagram. Both the 90º excitation pulse and the two 180º refocusing pulses are slice-selective and are applied in orthogonal directions to achieve spatial localization. (b) The STEAM sequence that uses three 90º slice-selective pulses for spatial localization. Reproduced from [22].

SVS pulse sequences are currently employed in the clinic since a single averaged spectrum can be quickly acquired from the desired VOI, such as from a region containing a tumor. Depending on the selected sequence parameters such as the repetition time (TR), number of averages, and the volume size, the scan time can be as less as a few seconds to

acquire a quantitatively good spectrum. Furthermore, SVS is popular due to its ease of implementation and simplicity, better water suppression, more homogeneous B_0 shimming achievable on smaller voxels, lack of artifacts from voxel-to-voxel bleed, and immediate analysis and interpretation of the spectra. However, as only a single spectrum can be obtained at a time from the defined volume, multiple measurements might be necessary when evaluating several regions of the anatomy [21]. This limits the benefit of SVS in accessing voxel-to-voxel variations in metabolite concentrations in a single measurement.

1.2.2 Chemical Shift Imaging

CSI combines the features of both spectroscopy and imaging by acquiring multiple spectra from adjacent voxels in a single scan. There is no readout gradient applied in MRSI during data collection, and phase encoding gradients are applied in either one (1D), two (2D), or three (3D) directions to achieve spatial localization [21]. A three dimensional fast Fourier transform (FFT) is then applied to reconstruct the MRSI data. Following reconstruction, the acquired spectral data is post processed and displayed as spectra or metabolite maps overlaid on the anatomical reference image. Figure 1.2 illustrates a conventional volume-selective 2D MRSI pulse sequence based on the PRESS excitation scheme, along with representative spectra and metabolite maps from a clinical MRSI dataset. The PRESS volume is excited using three slice-selective RF pulses and gradients G_x, G_y, and G_z. The second half of the echo produced at TE_2 is sampled. A 3D (k_x, k_y, t) matrix is generated by applying phase encoding gradients along the x and y directions to spatially encode the echo.

4

Due to the availability of spectra from multiple contiguous voxels, MRSI aids the comparison of metabolic profiles from different types of tissues. For e.g. in cancer patients, spectra from normal and tumor tissue can be simultaneously acquired to evaluate heterogeneity in metabolite concentrations. Multiple voxels acquired from within the tumor region can also be used to assess whether there is any heterogeneity in metabolite distributions in the same lesion [21]. Multiple adjacent voxels can also be combined to replicate the shape of the tumor and subsequently combine the corresponding spectra.

However, MRSI has its share of problems, the primary one being the long scan time even when acquiring a low resolution spectroscopic grid, for e.g. a 16 x 16 matrix with a TR of 1.5 s and one signal average would require a scan time of 6.4 minutes. A long TR > 1 s is required since most metabolites have long T_1 recovery times. Multiple averages are often required in regions that are inherently SNR limited, causing a further increase in the acquisition time. Variations in magnetic susceptibility are encountered since a relatively large excitation volume is selected in MRSI, leading to non-uniform water suppression and poor shimming. This in turn affects the point spread function (PSF), giving rise to spectral contamination from the resulting voxel bleed that could give rise to errors in spectral interpretation [21]. Furthermore, the complete analysis of MRSI data requires several processing steps that might also vary between different data types [23]. A lack of standardization in MRSI acquisition protocols and non-availability of common processing and analysis tools for a simple and quick evaluation of metabolite concentrations makes this technique less appealing to the radiologist for routine clinical investigations.

5
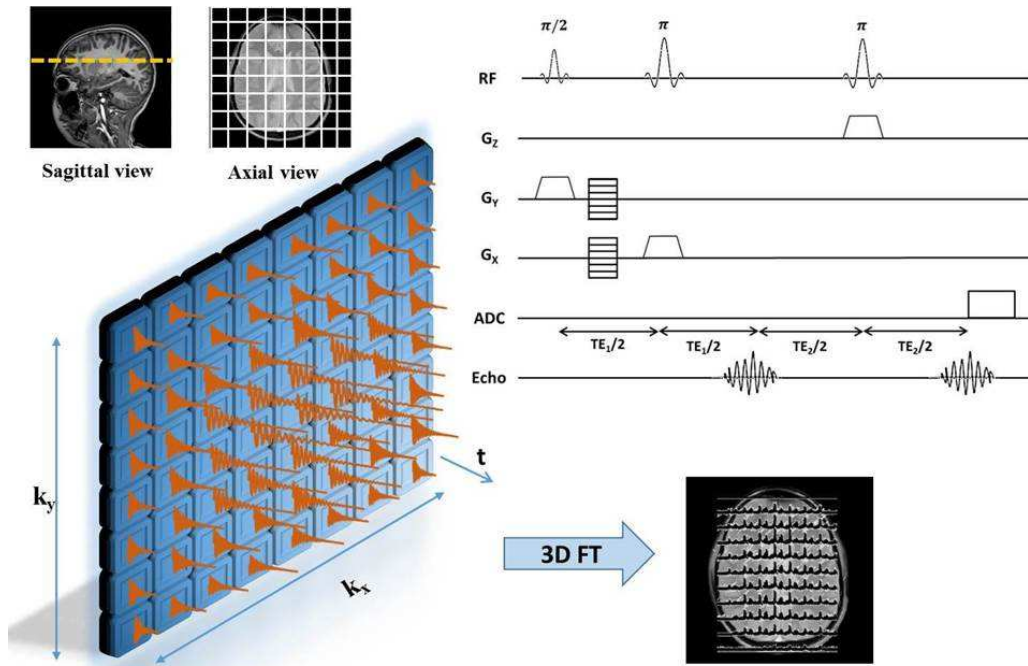
(a)
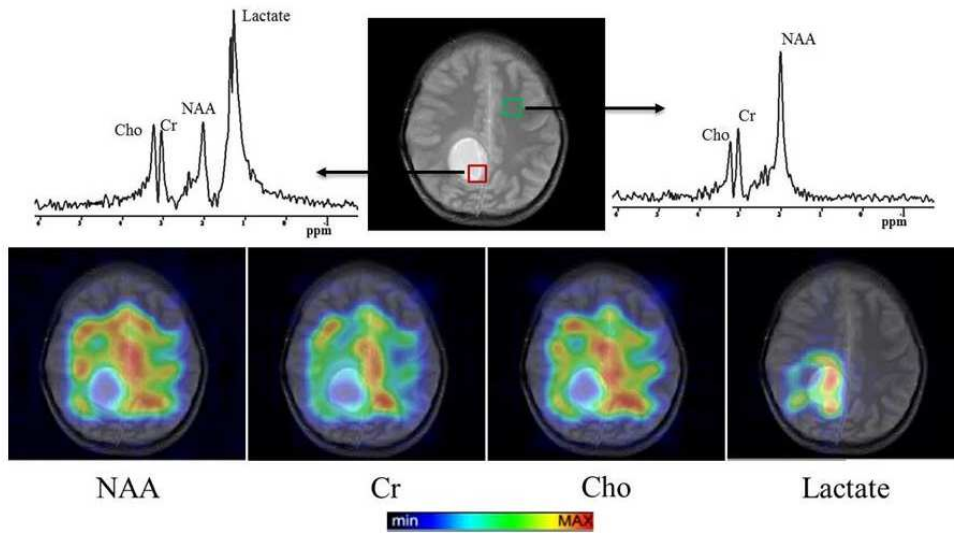
(b)

Figure 1.2 Conventional MRSI data acquisition. **(a)** A PRESS-based volume selective 2D MRSI pulse sequence. The second half of the second echo at time TE_2 is sampled. The total acquisition time in 2D MRSI for a slice in the z direction would be N_x x N_y x N_{avg} x TR, where, N_x and N_y are the number of phase encodes along the x and y directions, respectively, N_{avg} is the number of signal averages, and TR is the repetition time of the pulse sequence. **(b)** Representative metabolite maps of the major brain metabolites NAA, creatine (Cr), choline (Cho), and lactate seen in a brain tumor patient with spectra from normal and tumor voxels.

1.3 Key Metabolites Observed in ^{1}H MRS/MRSI

1.3.1 N-acetylaspartate

The methyl (CH_3) group of N-acetylaspartate (NAA) gives rise to a prominent singlet at 2.01 ppm in the proton spectrum observed in MRS/MRSI. Three doublet-of-doublets are also found centered at 2.49 ppm, 2.67 ppm, and 4.38 ppm (from the CH_2 and CH groups), with a broad temperature-sensitive resonance at 7.82 ppm (from the exchangeable amide NH proton). NAA is found exclusively in the peripheral and central nervous systems, with different parts of the brain showing varied concentrations [4, 21, 24]. Higher concentrations are found in gray matter (~8-11 mM) as compared to that found in white matter (~6-9 mM). NAA has been found to play an important role in (1) fatty acid and myelin synthesis, (2) osmoregulation, and (3) in being the break down product of the neurotransmitter NAAG. NAA does not play a vital role in the energy metabolism of glucose in the resting brain as evidenced by the slow NAA turnover observed in ^{13}C NMR spectroscopy. The average concentration of NAA in the normal adult brain varies between 7.5 – 17.0 mM/L [4, 21, 24], while that in the rat brain is in the range of 4.5 – 9 mmol/L [4, 21, 24].

The NAA resonance is primarily viewed as a marker of neuronal density. Dynamic changes in NAA concentrations are suggestive of neuronal dysfunction as opposed to neuronal loss. Several brain disorders like stroke, temporal lobe epilepsy, multiple sclerosis, and hypoxic encephalopathy exhibit a decrease in NAA levels [25]. In multiple sclerosis, both visible lesions as well as normal appearing regions of while matter show reduced NAA concentration [26]. NAA loss is also observed in malignant brain tumors due to destruction of neurons, particularly in extra-axial meningiomas [25].

Brain abscesses and secondary (metastatic) neoplasms may show reduced or completely absent signal from NAA [26]. In ischemia or hypoxia, NAA is used as a concentration maker, as the acute metabolic disturbances in these diseases do not significantly alter its concentration [24].

1.3.2 Creatine

The methyl and methylene protons of Cr and phosphorylated creatine (PCr) give rise to singlet resonances at 3.03 ppm and 3.93 ppm, respectively. Both glial and neuronal cells in the brain contain Cr and PCr. Creatine is mostly synthesized in the liver and kidneys. Total creatine (tCr), which is the sum of Cr and PCr, plays an important role in the energy metabolism of tissues, along with adenosine triphosphate (ATP) [4, 24]. PCr, in combination with creatine kinase, plays two major roles: (1) maintains constant ATP levels via the creatine kinase reaction, serving as an energy buffer, and (2) it functions as an energy shuttle by diffusing from energy producing regions like the mitochondria to energy consumption sites like the muscle and brain. The concentration of Cr and PCr in the normal human brain has been reported to be $4.5 - 6.0$ mM and $4.0 - 5.5$ mM, respectively [4, 24]. Lower levels are found in white matter ($5.2 - 5.7$ mM) as compared to that in gray matter ($6.4 - 9.7$ mM) [4, 24].

TCr is frequently employed as an internal concentration reference as levels remain relatively constant in various diseases, with no changes being observed even with age. However, any internal concentration reference must be used with caution as regional and individual variations in concentration are likely. Chronic phases of various tumors and stoke have displayed a decrease in Cr levels. Increased metabolic activity in certain

high-grade gliomas may reduce the total creatine concentration [25]. As Cr is not generated in the brain, other diseases like renal diseases may affect creatine levels in the brain [25]. Reduced or absent creatine signal has been observed in various conditions like seizures, brain abscesses, AIDS, autism, and mental retardation [27]. Prostate cancers have shown higher creatine levels as compared to normal prostate tissue [28].

1.3.3 Choline

The methyl protons of choline-containing compounds give rise to a prominent singlet at 3.2 ppm in the ^{1}H MRS spectrum. This peak is the signal from 'total choline' (tCho), which contains contributions from free choline, phosphorylcholine (PC), and glycerophosphorylcholine (GPC). The peak at 3.2 ppm has a significant contribution from betaine in tissues present outside the central nervous system (CNS). In the normal adult human brain, the concentration of total choline is approximately 1 – 2 mM, with a non-uniform distribution in the brain [24]. Choline-containing compounds are reflective of membrane turnover, as they are involved in the phospholipid synthesis and degradation pathways [24].

Fluctuations in the levels of the tCho peak have been seen in various diseases. Increased choline concentration has been observed in various brain, breast, and prostate cancers, in Alzheimer's disease, and in demyelinating autoimmune diseases like multiple sclerosis [24]. On the other hand, reduced choline signal has been detected in stroke and liver disease [24]. Multiple contributions to the observed total choline signal tend to complicate an accurate interpretation of changes in tCho. In malignant tumors and (primary and secondary/metastatic) neoplasms, increased cellularity causes an increase in

9

the total choline concentration [25]. Various factors at the cellular level contribute to an

elevated choline signal, such as destruction of normal cells or increased cell membrane

turnover due to tumor growth. The choline signal has been found to be absent in brain

abscesses, while a very prominent choline peak has been reported in the lymphoma in

AIDS [25].
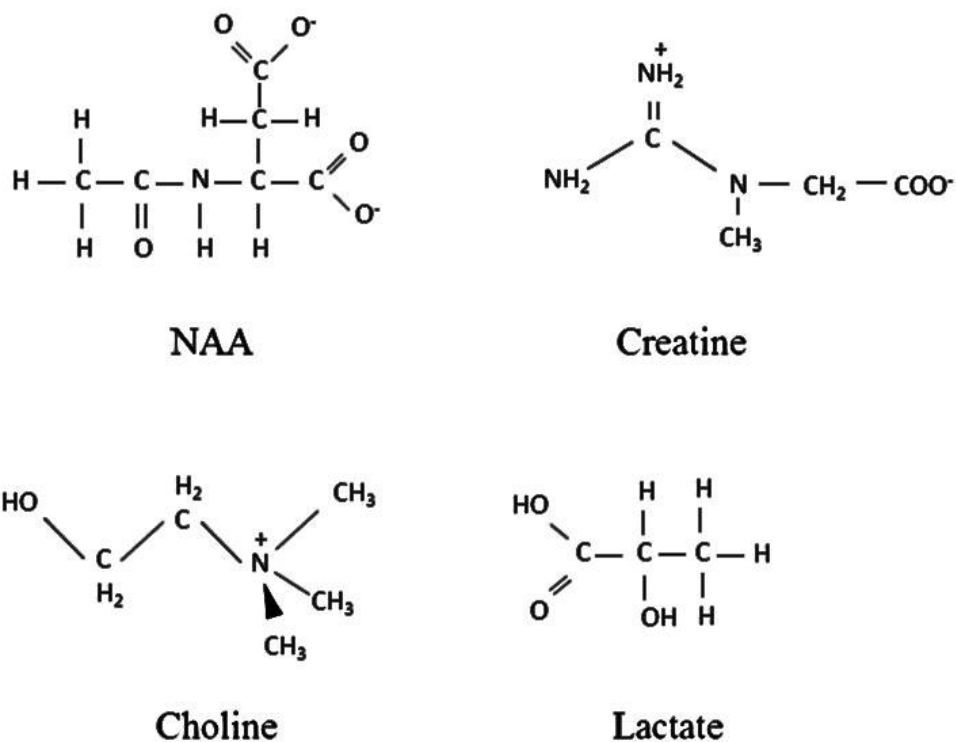
Figure 1.3 Chemical structure of major metabolites observed in the 1H MRS/MRSI
spectrum [29].

1.3.4 Lactate

The three equivalent methyl (CH$_3$) protons of the lactate molecule produce a

doublet at 1.31 ppm, while the single methine (CH) group gives rise to a quartet at 4.10

ppm. Large resonances from the lipid molecules tend to overlap with the lactate doublet,

particularly in regions with poor localization. Under such circumstances, specialized spectral editing techniques need to be employed for improved detection of the lactate peak [24]. Lactate is present in very low concentrations (~0.5 ppm) in normal resting tissues and is the end-product of anaerobic glycolysis. According to the astroglial-neuronal lactate shuttle (ANLS) hypothesis, neurotransmitter cycling and metabolism is linked to astroglial glucose uptake and metabolism via the lactate molecule [24].

High lactate concentrations have been found in various diseases like brain abscesses, brain ischemia, primary and secondary neoplasms, seizures, and in regions of acute inflammation, as signified by macrophage accumulation [25]. In all the above mentioned conditions, a failure in the aerobic oxidation process leads to an increased uptake and conversion of glucose to lactate by the Warburg effect, leading to increased lactate accumulation [30]. Furthermore, poor washout mechanisms in cystic and necrotic tumors lead to higher lactate levels in malignant lesions. Functional activation and hyperventilation in the human brain has also been found to cause a transient increase in the lactate signal [24].

1.3.5 Other Important Metabolites

A detailed description of NAA, creatine, choline, and lactate was provided in the previous sections as these metabolites were observed and quantified in the studies presented in Chapters 3, 4, and 5 of this dissertation. Other metabolites that are key biomarkers in various diseases are also observed in the MRS spectrum, such as alanine, citrate, γ-Aminobutyric Acid (GABA), glutamate, glutamine, glycine, and myo-Inositol. An increase in alanine levels has been found in ischemia and in meninigiomas [24], while

in prostate cancer, increased oxidation due to a drop in zinc levels leads to a significant decrease in the citrate concentration [24]. Altered concentrations of GABA are have been detected in several psychiatric and neurological disorders, such as depression and epilepsy [24]. Both glutamate and glutamine play an important role in the neurotransmitter cycle, while glycine functions as an antioxidant and inhibitory neurotransmitter [24]. Variations in myo-Inositol levels have been detected in brain injury and Alzheimer's disease, with osmotic regulation being another role played by this metabolite in the kidney [24]. Figure 1.4 shows the metabolites that can be detected in the ^{1}H MRS spectrum.
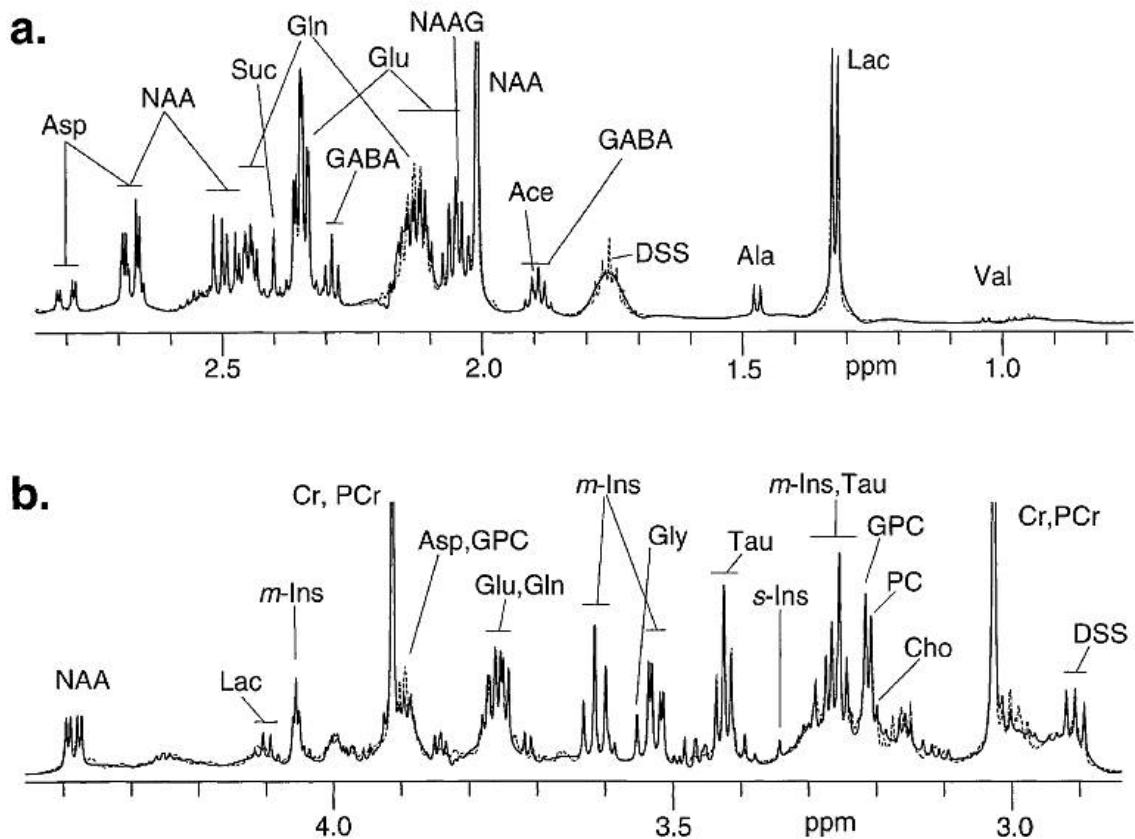
Figure 1.4 Metabolites seen in the 1H MRS spectrum in the (a) 0.75 – 2.85 ppm range, and (b) 2.85 – 4.45 ppm range. Reproduced from [29].

1.4   Data Processing in MRS/MRSI

The acquired MRSI data are processed and analyzed in order to determine absolute/relative metabolite concentrations, and to present the metabolic information in an easily interpretable format to the radiologist. Various processing steps that can be applied to manipulate the MRSI data in either the time or frequency domain are briefly outlined below [21].

(1) DC Offset Correction

A DC offset present in the FID signal will produce a spike at zero frequency (0 Hz/ppm) in the corresponding spectrum. The offset is estimated from the baseline of the FID data and subtracted before applying the Fourier transform to eliminate the spike.

(2) Zero-filling

The FID can be zero-filled in order to improve the spectral resolution, thus, facilitating a better discrimination of various spectral features, like peak positions and amplitudes. Zero-filling should be applied with caution, as this might lead to baseline artifacts in the resulting spectrum when the FID has not completely decayed to the noise floor.

(3) Apodization

The FID signal is usually multiplied with a filter function to improve the SNR and reduce any truncation artifacts. For e.g. a decaying exponential filter like the Gaussian filter suppresses the noise at the end of the FID. This helps in improving the SNR while causing a broadening of the spectral peaks (which depends on the line broadening constant of the applied filter). Step-like signal discontinuities are also eliminated as the

filter smooths the FID signal decay to zero, removing sinc-like side lobes in the resulting spectrum.

(4) Phase Correction

Prior to quantification, the real and imaginary components of the complex spectrum need to be accurately determined from the pure absorption and dispersion modes. A constant or zero-order phase correction φ_0 is applied when all signal components experience the same phase shift, for e.g. if the transmitted and received RF signals have a fixed phase difference. A linear or first-order phase correction φ_1 is required when various signal components experience different phase shifts. Both φ_0 and φ_1 are varied independently to get the best separation between the absorption and dispersion modes.

(5) Baseline Correction

The baseline of a MR spectrum should be flat and free of distortions for accurate estimation of peak areas. Baseline distortions are more pronounced in spectra obtained at short TE, especially when the residual water signal is not properly subtracted during post processing. Other distortions are introduced by immobile nuclei such as macromolecules, which give rise to broad plateaus in the MRS spectrum. Polynomial or cubic-spline based fitting is used to approximate and correct for any distortions in the baseline.

(6) Removal of Residual Water

A significant residual water peak remains in the spectrum in regions where the localization and OVS suppression was poor, for e.g. in the peripheral regions of the brain where the magnetic field may not be homogeneous. This residual water peak has to be eliminated prior to metabolite fitting and quantification. Techniques like the singular

value decomposition (SVD) and the Hankel-Lanczos variant (HLSVD) [31] allow reliable automatic suppression of any residual water, with little to no user input required.

(7) Spectral Fitting & Quantification

The final step in the processing and analysis of MRS/MRSI data involves fitting the various peaks of interest in the spectrum to known line shape functions such as the Gaussian (more common for solids), Lorentzian, or a combination of two or more functions [21]. Spectral components can be estimated using various quantification algorithms such as AMARES (Advanced Method for Accurate, Robust and Efficient Spectral fitting) [32], HLSVD [31], HTLS [33], and QUEST (QUantitation based on QUantum ESTimation) [34, 35]. A priori information like the frequency range, full width at half maximum (FWHM), peak positions and amplitudes can be specified to obtain a good peak fit. The best fit between the measured and theoretical curves is then determined using an iterative curve fitting algorithm. Curve fitting techniques can be applied in either the frequency or time domain. After post processing, results are displayed either as an individual spectrum (in case of SVS), or as individual metabolite maps overlaid/co-registered on the anatomical reference image in MRSI.

CHAPTER 2

FAST DATA ACQUISITION STRATEGIES IN MRSI

Fast scan strategies could potentially facilitate increased adoption of MRSI into routine clinical protocols with minimal addition to the current acquisition times. Not surprisingly, a lot of effort has been devoted to the development of faster MRSI techniques that aim to capture the same amount and quality of information as conventional MRSI in greatly reduced time. This chapter examines the current techniques and advances in high-speed MRSI in 2- and 3-dimensions and their applications. Since encoding of position in conventional MRSI itself is an extension of that in MRI, most of these acceleration techniques are not MRSI-specific. All discussed acceleration approaches have initially been applied and tested in MRI before their adoption in MRSI. However, each acceleration technique has been suitably modified to accurately capture the challenges and nuances of spectroscopic imaging. The advantages and limitations of each state-of-the-art technique have been reviewed in detail, concluding with a note on future directions and challenges in the field of fast spectroscopic imaging.

2.1 Conventional MRSI

A PRESS-based volume selective conventional 2D MRSI sequence has previously been described in Chapter 1. The data acquisition process in conventional MRSI is tedious, which is a deterrent for its integration into current clinical protocols. A large number of phase encoding gradients need to be played out to sample all points in k-space, leading to long scan times. Parameters like the TR of the MRSI pulse sequence,

size of the spectroscopic imaging grid, and the number of signal averages required to achieve good SNR determine the total acquisition time. For e.g. for a TR of 1.5 s and one signal average, the clinical acquisition of a 16 x 16 x 2048 spectroscopic imaging grid would require a scan time of 6 min 24 s. While on the other hand, one can realize a shorter scan time in MRI by applying frequency encoding along one direction, with phase encoding along the remaining dimensions.

There is often a further increase in the scan time due to the need for higher signal averaging to ensure acceptable SNR and/or when high resolution MRSI data are acquired. 3D MRSI datasets cannot be acquired in patients, especially in the pediatric setting, due to the prohibitive scan time. E.g. the acquisition of a 16 x 16 x 16 spatial matrix would require a scan time of $\sim$ 1.14 hours, considering one signal average and a TR of 1 s. The total imaging time is further increased as it is also necessary to collect reference anatomical information in every study. Another limitation to be considered in MRSI is the inherent low SNR, which arises from the MR visible metabolites having low concentrations in the range of <0.1 to 16.6 mM [29], as compared to 55 M of water in the human body. One can potentially lower the resolution and utilize the time gained to increase the SNR. This would, however, cause a volume averaging of the voxels and potentially lower the contrast to noise ratio (CNR) of the target metabolite with respect to the other metabolites. On the other hand, higher averages at the same resolution would lead to a further increase in the scan time.

The above discussed limitations do not make conventional MRSI a feasible option to the clinician for regular *in vivo* investigations. Increased volume coverage at acceptable SNR and imaging speed are critical to the incorporation of MRSI in the clinic.

To this end, numerous fast imaging strategies that have been developed to achieve acceleration in MRI have been accordingly modified and applied to MRSI to shorten the scan time. Acceleration techniques will facilitate the evaluation of serial changes in metabolite distributions and heterogeneity in spatial profiles in a clinically viable time frame [15]. Such innovative pulse sequences will not only reduce the scan time, but will ensure best use of the available magnetization to simultaneously achieve/preserve good SNR and spatial resolution. Parallel advances in the design of efficient gradients, multichannel RF coils, sophisticated reconstruction algorithms and post processing routines, and high field scanners will make a significant contribution to realizing these goals.

2.2   Fast MRSI with More Efficient K-space Traversal

A major approach to achieve acceleration in MRSI data acquisition is to traverse the k-space in a more time efficient manner i.e. effectively cover more k-space locations within the chosen TR. This includes novel k-space sampling schemes like non-Cartesian trajectories (spiral, radial, rosette, etc) and pulse sequences that acquire multiple lines of k-space within the same TR. Techniques that fall under this category usually gain speed at the cost of SNR loss and resulting coherent artifacts.

2.2.1 Turbo MRSI

One of the first acceleration techniques to accelerate MRSI data, particularly in the brain [36, 37], was multi-echo imaging. Duyn *et al* developed a multi-echo, multi-slice MRSI technique that enabled the acquisition of multiple spin echoes within the

same TR [36]. In conventional spectroscopic imaging, there is pronounced attenuation of the fat and water resonances arising from T_2 decay, as a single spin echo signal is commonly sampled at long echo time (TE). The metabolites of interest, such as NAA, creatine, and choline experience greater signal decay from intra voxel susceptibility effects as compared to T_2 decay. Thus, multiple spin echoes were acquired in the same TR to increase the efficiency of data collection, leading to a decrease in the scan time. An echo train length of 4 was used to achieve a 4X decrease in the acquisition time as compared to the single echo technique [36]. A fast spin echo based spectroscopic imaging sequence is illustrated in Figure 2.1.
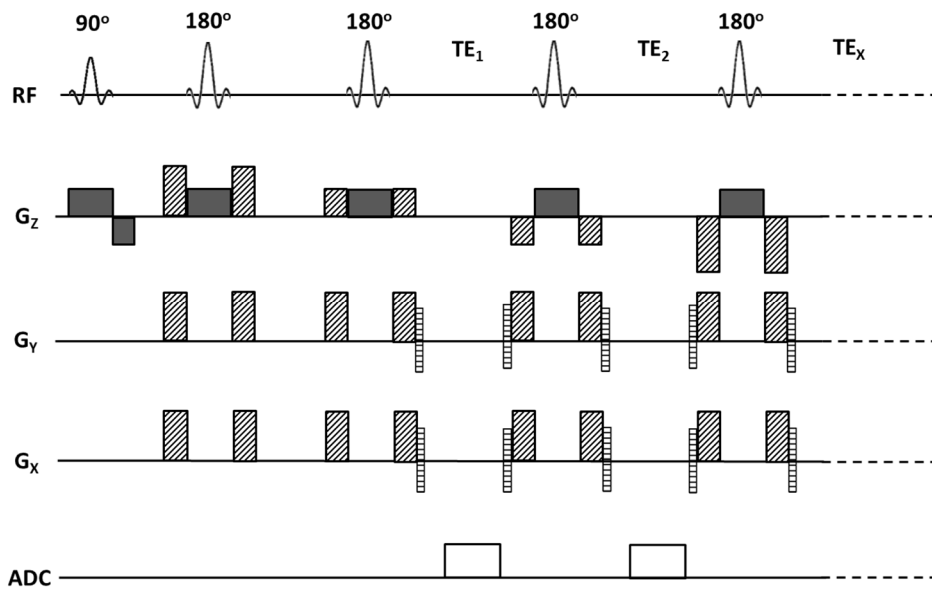
Figure 2.1 A turbo or fast spin echo spectroscopic imaging sequence. This sequence generates and acquires slice-selective spin echoes at echo times TE_1, TE_2, …,TE_X, in intervals between the 180º RF pulses. G_x, G_y, and G_z depict the gradient channels. Phase encoding gradients encode each individual echo in the acquisition interval. Crusher gradients (indicated by the diagonally shaded gradient pulses) around the 180º pulses suppress any unwanted signals. Any other unwanted coherences are suppressed with the help of phase encoding rewinders. Gradient pulses depicted by the solid gray boxes represent slice-selective gradients. Additional outer volume suppression (OVS) and water suppression modules can be added before the 90º pulse. Adapted from [36].

19

However, this technique does have several limitations. The data acquisition readout for spectroscopic imaging needs to be of the order of 0.3–1 s to maintain reasonable spectral resolution, and significant T_2 decay would have already occurred by the time the subsequent echoes are encountered [37]. Consequently, metabolites with short T_2 cannot be observed using this technique. This may force one to accept limited spectral resolution due to fewer echoes and smaller acquisition windows to gain speed. There is also considerable T_2 weighting of different echoes, and metabolites like lactate need to be imaged carefully taking into account the fact that the choice of TE modulates the signal appearance of these metabolites [37]. Also, for long echo train lengths, the minimum TR often needs to be increased to accommodate the long readout window required, which tends to offset the time gained in multi-echo encoding.

Other related multi-echo based fast MRSI techniques include the spectroscopic ultrafast low-angle rapid acquisition with relaxation enhancement (UFLARE) [38, 39], and the spectroscopic gradient and spin echo (GRASE) [40] imaging techniques (Figure 2.2). Spectroscopic UFLARE acquires "slices" of k-space by measuring all data points in the k_x-k_y plane at a given value k_ω after each signal excitation, i.e. within the TR using the fast imaging method UFLARE [41]. There are two different ways to encode the chemical shift. In the first approach, the beginning of the imaging sequence is shifted with respect to the RF excitation in subsequent measurements. Alternately, the time interval between the 90° excitation pulse and the imaging sequence is kept constant and the position of a refocusing 180° pulse, applied within that interval, is incremented to encode the chemical shift. In spectroscopic GRASE, after each signal excitation, all data points from N_{GE} gradient echoes k_x-k_y slices are acquired at different k_ω-values by using a

20

GRASE imaging sequence [42]. The delay between consecutive gradient echoes, which are measured with uniform phase encoding between consecutive refocusing pulses, is the inverse of the spectral width (SW). A refocusing 180° pulse, which is applied within a constant delay between excitation and the GRASE sequence, is shifted for subsequent measurements by an increment $N_{GE}/(2*SW)$ to cover the whole k_ω-k_x-k_y-space.
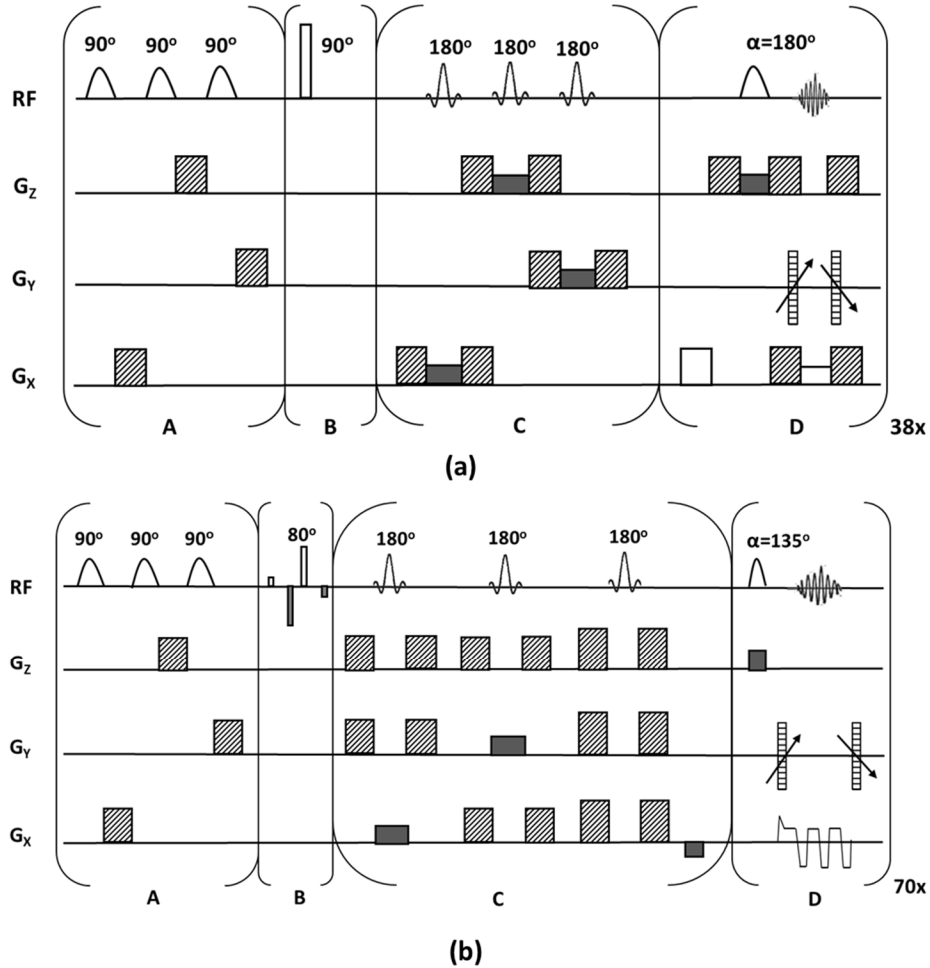
Figure 2.2 Spectroscopic (a) U-Flare and (b) GRASE imaging pulse sequences with a pre-saturation period (A), excitation and evolution (B), an optional localization period (C), and readout (D). Spoiler gradients are denoted by diagonally shaded gradient pulses, while solid gray and white boxes depict slice-selective and read-out gradients, respectively. The alternate phase-encoding scheme was employed for signal acquisition. Spectroscopic GRASE enables effective homonuclear decoupling, while achieving a lower minimum acquisition time (T_{min}) as compared to the spectroscopic U-Flare sequence. Adapted from [38] and [40].

2.2.2 Echo Planar Spectroscopic Imaging

EPSI (proton echo planar spectroscopic imaging or PEPSI in ^{1}H MRSI, Figure 2.3) was initially proposed by Mansfield [43], and further developed by Posse and co-workers [44-46]. The echo-planar imaging (EPI) method [43] was adapted by Mansfield in CSI to facilitate echo planar shift mapping (EPSM), which was faster than previously employed techniques like the 3D/4D Fourier transform [47] and the point-by-point topical magnetic resonance method [48]. The EPSI technique was later extended to 3D for spectroscopic imaging in the human brain at very short echo times (13 ms) [44, 46]. This resulted in acquisition times as low as 64 s, while maintaining an SNR that was comparable to that obtained using conventional MRSI techniques [44].
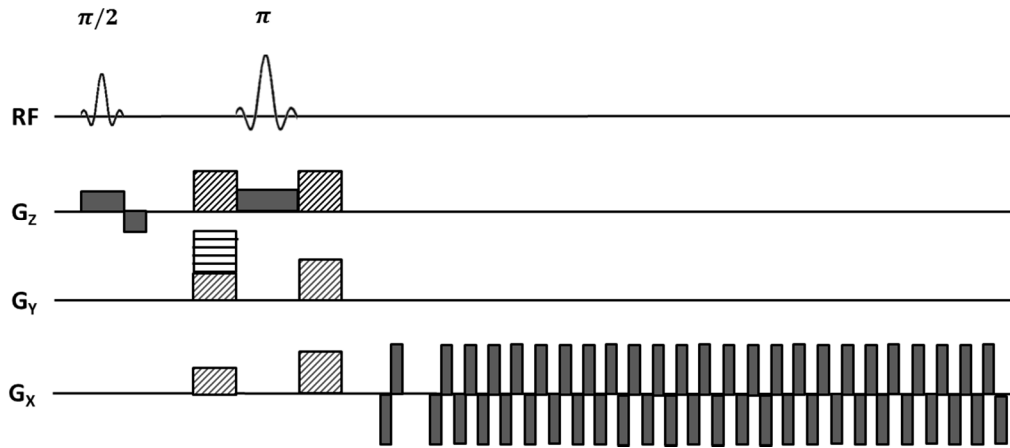
Figure 2.3 A PEPSI pulse sequence with a spin echo excitation section, and an echo-planar spectral readout. Additional outer volume suppression (OVS) and water suppression modules can be added before the 90° pulse. Adapted from [49].

The EPSI technique accelerates the filling of k-space (up to 3 spatial frequencies k_x, k_y, k_z, and time) by acquiring 2 (any one spatial frequency and time) of the possible 4 dimensions with each readout [50]. A frequency encoding gradient is rapidly switched during readout to acquire both spectroscopic and spatial data from any one k-space

dimension, which can subsequently be separated and re-gridded [50]. The acquired echoes can be separated into odd and even echoes, and each even (or odd) echo can be time-reversed and re-gridded to recover the free induction decays (FIDs) from the dimension that the echo planar readout was applied to. Information from the remaining two spatial dimensions can then be acquired using conventional phase encoding. Using EPSI acquisition in 3D, the time required to collect a 16x16x16 spectroscopic grid is only 16x16 s (assuming one second per signal acquisition and one average), reducing the scan time from 1 hr 16 min to approximately 4 min 16 s.

However, EPSI has its share of technical limitations. The use of rapidly oscillating read out gradients places high hardware demands on the gradient system, while the spectral bandwidth is limited by the gradient strength and slew rate [51]. Furthermore, only half the spectral bandwidth is used in conventional EPSI as the even and odd readout echoes are utilized separately during reconstruction. Limited spectral bandwidth is particularly a problem at higher magnetic field strengths (> 3 T) as chemical field dispersion effects increase leading to spectral aliasing [51]. Metabolic images tend to exhibit ghosting artifacts due to the off resonance effects, also commonly seen in echo planar imaging (EPI). This can be compensated for by using a cyclic unwrapping method, wherein the aliased portion of the spectrum is cyclically shifted and the region downfield is filled with zeros to obtain a modified spectral distribution [51].

There is a drop in the SNR during data acquisition due to the readout gradient and the associated short dwell times (resulting in increased bandwidth and hence noise) as compared to conventional MRSI [50]. Due to the stated limitations, increased averaging may be required to improve the SNR, which may neutralize the speed gain.

23

Nevertheless, EPSI may be useful in specific applications where loss of SNR is acceptable in favor of faster imaging, for e.g. in imaging hyperpolarized probes where one battles dynamic signal loss due to T_1 [52]. Over the last couple of decades, EPSI has been employed in numerous preclinical and clinical studies, also involving non proton nuclei such as ^{13}C and ^{31}P [52, 53].

2.2.3 Non-Cartesian MRSI

K-space is traversed in a rectilinear manner in conventional MRSI by the choice of phase encoding gradients, leading to long acquisition times. Non-Cartesian trajectories like the spiral, radial, and less common ones like the rosette, traverse k-space more efficiently enabling faster scans. Therefore, non-Cartesian k-space sampling has gained increased attention over the years in accelerating MRSI. Spiral MRSI, originally developed by Adalsteinsson $et\ al$ [54] traverses the (k_x, k_y) space in a spiral trajectory by applying gradient waveforms along the x and y axes. The (k_x, k_y, k_ω) space is traversed by these gradients with the evolution of time. Rewinding gradient lobes are added immediately after the spiral gradients to facilitate return to the k-space origin, as depicted in Figure 2.4.

Multiple spiral shots can be employed to map out the entire k-t space and collect all data points. The collected data are then interpolated onto a Cartesian k-space grid by employing a regridding algorithm for the use of conventional Fourier reconstruction techniques [54]. The SNR of the spectra reported by Adalsteinsson $et\ al$ was found to be comparable to that from conventional MRSI techniques using long echo times and

inversion recovery pulses for lipid suppression, demonstrating the value of spiral trajectories for rapid volumetric spectroscopic imaging.
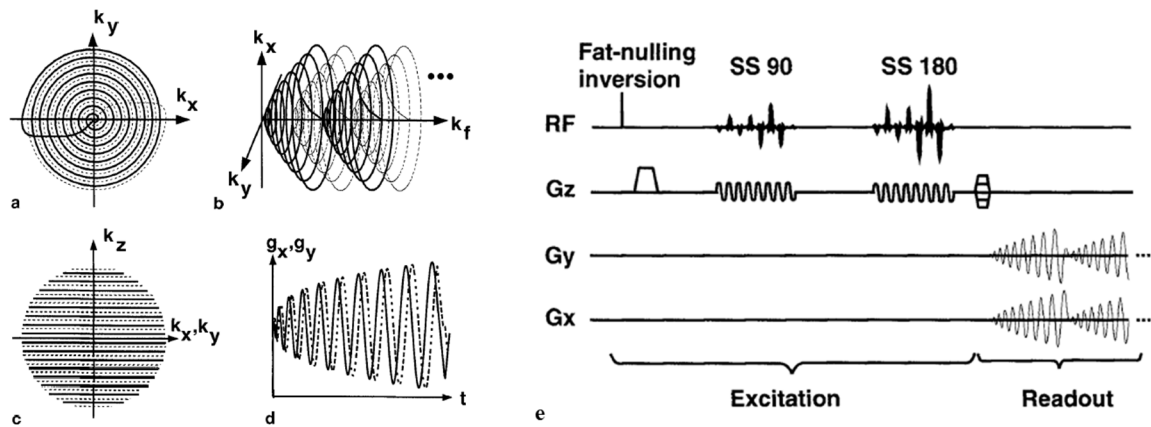
Figure 2.4 The spiral trajectory in k-space. (a) Trajectory with a rewinding path back to the origin, (b) the path traced by the trajectory in (k_x, k_y, k_f) space during the readout time, (c) phase encoding used to cover the k_z dimension (spherical or ellipsoidal coverage), (d) the gradient waveforms over one period, and (e) a pulse sequence diagram employing spiral gradients on G_x and G_y to simultaneously encode the x, y, and f dimensions. Reproduced from reference [54].

Spiral MRSI has similar constraints and limitations as PEPSI as discussed in the previous section, since it applies a readout gradient during data acquisition similar to that used in PEPSI. The spiral trajectory tends to be less demanding on the gradient system as compared to the EPI waveform. Artifacts can be minimized by carefully calibrating the gradient system [37]. The need for sophisticated reconstruction software and lack of widespread availability has resulted in limited application of spiral MRSI in the clinic as compared to EPSI. Nevertheless, MRSI sequences employing spiral k-space trajectories have found numerous applications over the years and continue to be researched and developed further.

Apart from spiral MRSI, there is also potential for developing different novel trajectories for the undersampling of k-space [55-58]. Concentrically circular [58], rosette

[56], and various other arbitrary k-space sampling trajectories have been investigated [55, 57] that can be adopted for MRSI.

2.3 Fast MRSI with Undersampling

The second major approach undertaken to speed-up MRSI data involves acquiring fewer points in k-space and subsequently recreating the complete spatial-spectral information either by zero-filling or by employing more advanced non-linear iterative reconstruction algorithms. This approach includes techniques like parallel imaging, compressed sensing, wavelet encoding, and elliptical sampling. These techniques are able to implement sparser sampling as the rectangular extent of the k-space and the properties of the Fourier transform allow accurate reconstructions even when certain regions of the k-space are not acquired [59]. The reconstructed data from these techniques can be viewed as an approximation to the "true" data acquired from transforming the full k-space. However, the fidelity of such approaches is validated by extensive statistical analyses of equivalence up to acceleration factors permitted by the inherent SNR of the data under consideration.

2.3.1 Circular & Elliptical Sampling

The circular sampling technique only measures and samples a circular region in k-space; the remaining points that have not been collected are zero-filled to produce a Cartesian grid for reconstruction using the fast Fourier transform (FFT) [3, 59]. Such a technique not only reduces the scan time, but also improves the profile of the point spread function (PSF). While circular sampling schemes slightly broaden the main lobe of the

26

PSF, a considerable reduction in the number of side lobes can be achieved by density weighting, thus, improving the PSF profile and reducing voxel bleeding [60]. However, this technique has its share of limitations. The spatial resolution essentially deteriorates and circular sampling creates a highly isotropic PSF, wherein the side lobes of the PSF are mainly propagated along the principle axis [3, 60]. Elliptical sampling provides better k-space coverage compared to circular sampling, particularly in cases where the spatial frequency extent is anisotropic. Spectral definition is accurately maintained, although there is a drop in the spatial resolution, similar to circular sampling.

2.3.2 Fast MRSI with Parallel Imaging

Parallel imaging utilizes multiple receiver coil arrays to permit k-space undersampling for accelerating data acquisition [61-63]. Reconstruction of raw undersampled k-space data into meaningful images in parallel imaging requires accurate knowledge of the coil sensitivities, and can be performed in either the image domain, as in sensitivity encoding (SENSE), or in k-space, as in simultaneous acquisition of spatial harmonics (SMASH) and generalized autocalibrating partially parallel acquisitions (GRAPPA) [63]. In parallel imaging, a typical tradeoff between data acceleration rate and the robustness of data reconstruction is an inherent loss in SNR dependent on the reduction factor R. An additional potential penalty is the geometry, or g-factor, which characterizes the ability of the measured coil sensitivity profiles to reconstruct the undersampled k-space raw data. Extensive details on the concepts and principles of parallel imaging can be found in the cited literature, and all these parallel imaging techniques can be used to speed up MRSI as well.

The application of SENSE to spectroscopic imaging is similar to anatomical imaging. In 2D SENSE MRSI, each k-space direction can be undersampled by R_x or R_y, resulting in a final undersampling factor of R_x x R_y [62]. This results in an effective n/R_x x n/R_y matrix from an originally n x n matrix, resulting in a reduced FOV. Because the effective FOV in SENSE MRSI is smaller than the true FOV, the reconstructed image is aliased (Figure 2.5) [62]. As in anatomical imaging, the unfolding process requires the collection of an accurate sensitivity map from each coil to determine the different weights in the superposed signal. Each voxel in the final image is a summation of signals from each coil multiplied by the sensitivity of that coil [62, 63]. In the spectral dimension, an aliased image at each sampling frequency needs to be unfolded. Using the notation followed in reference [61], if S denotes the sensitivity matrix, then the unfolding equation described by Pruessmann *et al* is given by:

$$U = (S^H \psi^{-1} S)^{-1} S^H \psi^{-1} \qquad (2.1)$$

Where, U is the unfolding matrix, ψ is the receiver noise matrix, and H is the transposed complex conjugate. The different weights derived from inaccurate coil sensitivity profiles would result in spurious signal artifacts [63].

In SENSE spectroscopic imaging, the loss in SNR is directly related to the reduction factor: the SNR drops by a factor of two when R = 4. The SNR is also affected by $1/g$, where g is the local geometry factor and is a function of the reduction factor as well as coil configuration. Optimal placement of the coils, which in turn is effected by trade-offs between single channel noise levels, coil coupling, and geometric and absolute sensitivity relations, can help ensure that g is almost close to 1. The SENSE technique is not applicable to a single channel coil, and the SNR usually drops for a lower number of

coil elements. SENSE encoding can be extended to the third dimension in 3D MRSI to obtain further decrease in the scan time. SENSE can also be combined with other high speed MRSI techniques like multi-echo MRSI to facilitate very fast imaging times.
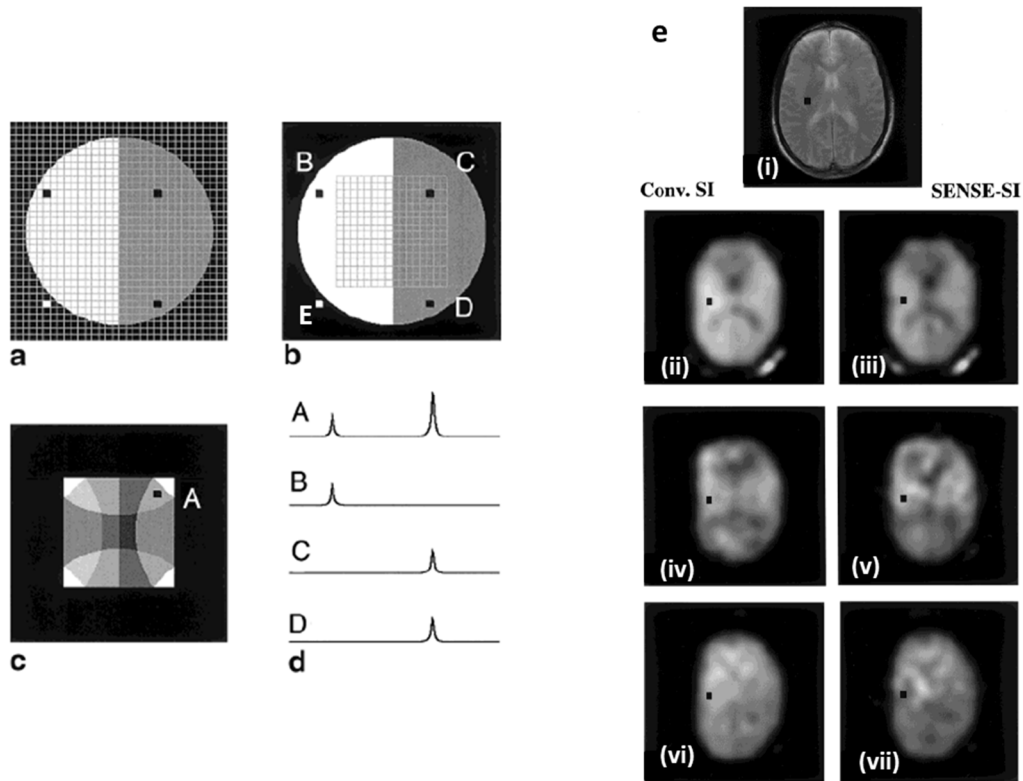
Figure 2.5 The basic principle behind SENSE MRSI. As an example, the object depicted contains two different metabolites as indicated by the color scheme (white and gray regions) in (a). A SENSE acquisition of a 16x16 grid shown in (b) results in a 4X decrease in the scan time as compared to a conventional 32x32 MRSI grid as only every fourth point in k-space is sampled. The resulting aliasing artifacts from Fourier reconstruction can be seen in (c). The SENSE reconstruction unfolds the data from voxel A, which is a weighted sum of the signal contributions from the four voxels highlighted in figure (b) into its components to obtain true signal C at that location. (e) Representative *in vivo* scout (A) and metabolite maps of NAA (B,C), Cr (D, E), and Cho (F, G) from conventional (left column, 26 min) and SENSE (right column 6.5 min) MRSI for a 32x32 spatial grid. The black voxel depicted in (e) was chosen for SNR comparisons between conventional and SENSE spectroscopic imaging. Adapted from reference [62].

GRAPPA requires the acquisition of the auto-calibration signal (ACS), which is essentially an additional calibration line that is collected along with the reduced data from each coil [64]. The data from multiple lines from all coils can be fit to the ACS line from a single coil, to generate the reconstruction weights that are used to estimate the missing lines. GRAPPA (Figure 2.6) has been tested in 2D and 3D in both ^{1}H and ^{31}P MRSI by various groups [65, 66].
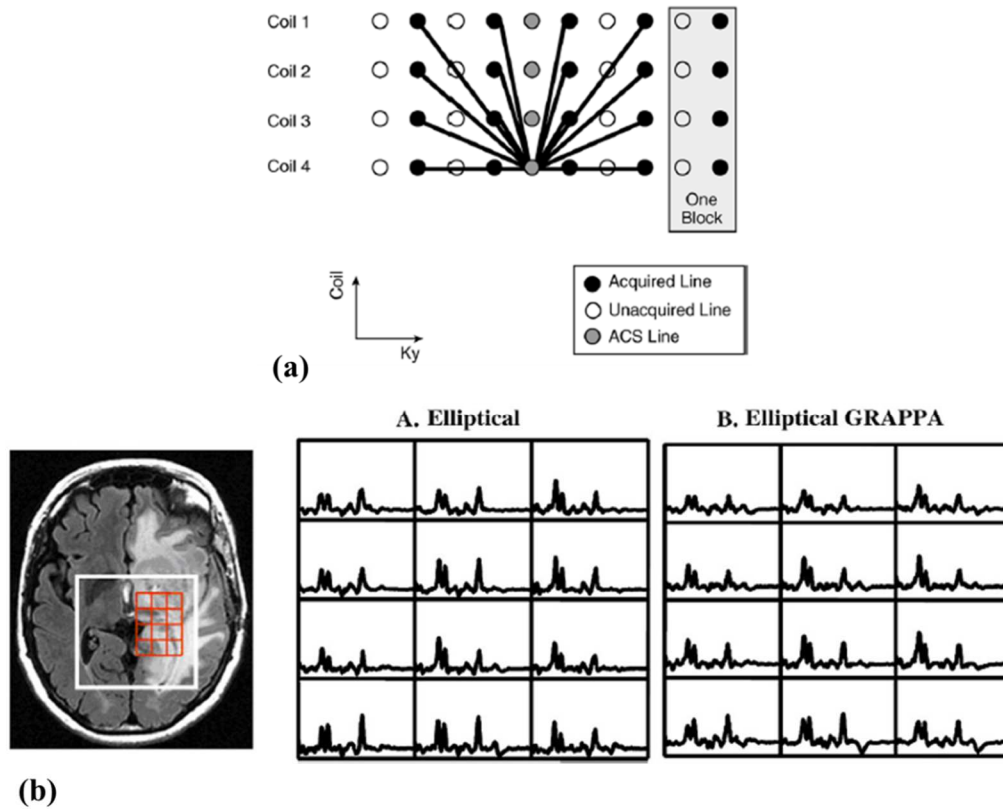
Figure 2.6 Fast MRSI acquisition using GRAPPA. **(a)** A schematic of the basic GRAPPA algorithm. In this example, a single ACS line in coil #4 is fitted using four acquired lines. In the GRAPPA technique, a single acquired line along with the missing lines present next to that line constitutes a block. A block has been depicted here for an acceleration factor of two. **(b)** An illustration of the application of GRAPPA to spectroscopic imaging in a glioma patient. Figure depicting spectra from the tumor region of the chosen PRESS volume of interest for (A) a 12x12x8 fully-sampled elliptical acquisition, and (B) a 16x16x8 elliptical GRAPPA acquisition. Reproduced from references [64] and [67].

2.3.3 Wavelet Encoded MRSI

The wavelet encoding technique employs prototype wavelet functions (the discrete wavelet transform, DWT) to identify defined regions in localized space using translations and dilations [68, 69]. The slice selective RF pulse profile is matched to a group of dilated and translated wavelets in MRSI. The spin echo sequence in 2D MRSI wavelet encoding has single and dual band slice selective excitation and refocusing pulses that have profiles similar to the Haar wavelets [68]. The dilations correspond to increases in the localization gradients, and translations correspond to the frequency shift of the RF pulses, which are represented using the Haar wavelets. The desired resolution can be achieved by employing a proportional number of dilations and translations. Successive MR signals are acquired from different locations housing regions of variable size, without the TR waiting time requirement between successive acquisitions, thus, reducing the total scan time [68]. The correct spatial distribution of the MR signal is subsequently obtained using an inverse wavelet transform.

Wavelet encoding permits the imaging of only a selected portion of the FOV in a noncontiguous manner. Different subspaces can be excited with no TR waiting time, accelerating data collection. As the excitation profiles of the RF pulses are modulated to resemble wavelet shapes, there is reduced pixel bleed in the spatial dimensions, which can be observed in the corresponding metabolite maps. The SNR in wavelet encoding is lower than that in Fourier encoding by almost a factor of two as this technique is limited by the length of the wavelet support [68]. In 2D wavelet MRSI, the SNR drops by a factor of ($((N^2 + 2)/6)^2$) * $(4/N^2)$ for an image of size N x N [68]. More averaging and/or less spatially localized wavelets can be employed to achieve a SNR comparable to that

31

found in conventional Fourier encoding. The wavelet encoding technique has also been extended to three spatial dimensions in MRSI by Young *et al* [69].

2.3.4 Compressed Sensing MRSI

CS is a novel approach that exploits the inherent sparsity of medical images in an appropriate transform domain to effectively undersample k-space. This in turn reduces the number of samples that are required for reconstruction in MRI and MRSI [70-72]. The CS theory successfully predicts that signals can be accurately recovered even when sampling well below the established Nyquist rate, if the signals under consideration are sparse in some transform domain (not just in the time or frequency domains) [73]. Data tend to be sparse in multiple dimensions of space and frequency in the wavelet transform domain, thus, making this technique particularly suitable for MRSI. Wavelets have been employed to achieve a sparse representation of MRSI data in both the spatial and spectral domains, facilitating the application of CS acquisitions in MRSI.

The CS based reconstruction of undersampled data has to fulfill three main requirements, namely, data sparsity, the implementation of pseudo-random undersampling, and a non-linear reconstruction algorithm for accurate recovery of the signals under consideration.

2.3.4.1 Transform Sparsity

A 'sparse' vector contains all information in a few non-zero coefficients, with all other coefficients being zero. 'Strong' sparsity is encountered when very few coefficients contain all the information in the signal. Most practical applications tend to exhibit

'weak' sparsity as a transition band exists been the few high-valued coefficients and the numerous non-zero coefficients. Most of the signal energy is restricted to these few non-zero coefficients, while the remaining measurements are essentially zero or close to zero [74]. A sparsifying transform operator can be applied to map the image vector under consideration to a sparse vector. For e.g. the Fourier transform of a direct current signal is a delta function in the frequency domain, which contains all the signal information. Thus, a sparse representation of a signal can be obtained by applying the appropriate transform operator. Similarly, most MR images tend to be sparse in some transform domain. For e.g. angiograms tend to be sparse in the finite differences domain as most of the important information is contained in the boundaries [70, 74]. Many sparsifying transforms have been developed over the years to facilitate sparse representations of different kinds of images [75]. Two particular transforms of interest are the wavelet transform and the discrete cosine transform (DCT), which provide a sparse representation of several real life images [76]. These transforms have been extensively employed in the field of image compression. A multi-scale representation of the image can be obtained using the wavelet transform. Fine-scale wavelet coefficients correspond to the high resolution image components while coarse-scale wavelet coefficients represent the low resolution components [70]. It is important to determine the minimum number of sparse coefficients that are required to obtain an accurate reconstruction of the MRSI data [74].

2.3.4.2 Pseudo-random Undersampling of MRSI Data

The second essential criterion in CS requires the random undersampling of the MRSI k-space in order to produce incoherent artifacts that resemble noise [70, 74].

Uniform k-space undersampling violates the Nyquist criterion producing coherent artifacts such as aliasing. While the random selection of k-space samples also violates the Nyquist limit, the resulting artifacts are sufficiently incoherent that they can be removed by denoising techniques. In the case of MRI/MRSI, the k-space is pseudo-randomly undersampled i.e. a certain fraction of the samples are placed at the center of k-space, while the remaining samples are randomly distributed in the peripheral k-space region. This is necessary as all the information and SNR is confined to the low frequency components, which are located at the k-space center. A truly random undersampling of the k-space also necessitates rapid gradient switching, which is constrained by the hardware and artifacts like eddy currents [71]. The number of required samples depends on the level of data sparsity and is usually five to eight times the number of sparse coefficients in the transformed data [71, 73]. Thus, identifying the number of sparse coefficients is critical to determining the acceleration limit of the CS reconstruction algorithm. Finding the 'optimal' sampling mask in MRSI continues to be an area of research and various approaches to identify the 'best' mask at a particular acceleration factor will be discussed in detail in Chapter 5 of this thesis.

2.3.4.3 Non-linear Iterative Reconstruction

The reconstruction of the acquired CS-MRSI data can be formulated as a constrained optimization problem, as illustrated in equation 2.2 below [70, 74]:

$$minimize \quad \|\psi m\|_1 \qquad\qquad (2.2)$$

$$such\ that \quad \|F_u m - y\|_2 < \varepsilon$$

34

Where, m is the desired MRSI data to be reconstructed, y is the acquired k-space data from the scanner, F_u is the undersampled Fourier operator, ψ is the transform operator that provides a sparse representation of the data, and the parameter ε controls the tolerance error of the reconstruction. $\|\ \|_1$ and $\|\ \|_2$ are essentially operators representing the l_1 norm and l_2 norm, respectively. Minimizing $\|\psi m\|_1$ enforces sparsity, while the data consistency constraint is enforced via $\|F_u m - y\|_2 < \varepsilon$. A total variation (TV) penalty is often included in the objective function in addition to a specific sparsifying transform operator. In such cases, the objective function ensures that the MRSI data has a sparse representation from both the specific transform as well as from finite differences. Equation 2.2 can then be reformulated to include the TV operator as follows [70]:

$$minimize \ \ \|\psi m\|_1 + \alpha TV(m) \tag{2.3}$$

$$such \ that \ \ \|F_u m - y\|_2 < \varepsilon$$

Wherein the operator α trades the sparsity from the finite differences and the ψ operator. Employing the Lagrange method, Equation 2.3 can recast as an unconstrained optimization problem that involves minimizing the following equation [70, 74]:

$$argmin \ \ \|F_u m - y\|_2^2 + \lambda_1 \|\psi m\|_1 + \lambda_2 TV(m) \tag{2.4}$$

Where, λ_1 and λ_2 are regularization parameters that need to balance the data consistency and sparsity terms. An iterative non-linear reconstruction algorithm such as the steepest descent method or the non-linear conjugate gradient technique can be employed to solve for the desired MRSI data m in Equation. For e.g. in the conjugate gradient algorithm, Equation is differentiated to determine the direction of the gradient each time. A line-search parameter is incorporated to evaluate the step-length to be advanced in the gradient direction. Convergence in the iterations is obtained when a)

there is negligible difference in the tolerance parameter values between successive iterations, and b) the tolerance parameter value is lower than the selected ε value. The total number of iterations required to obtain convergence in the cost function is dependent on problem at hand and the type of data being evaluated.
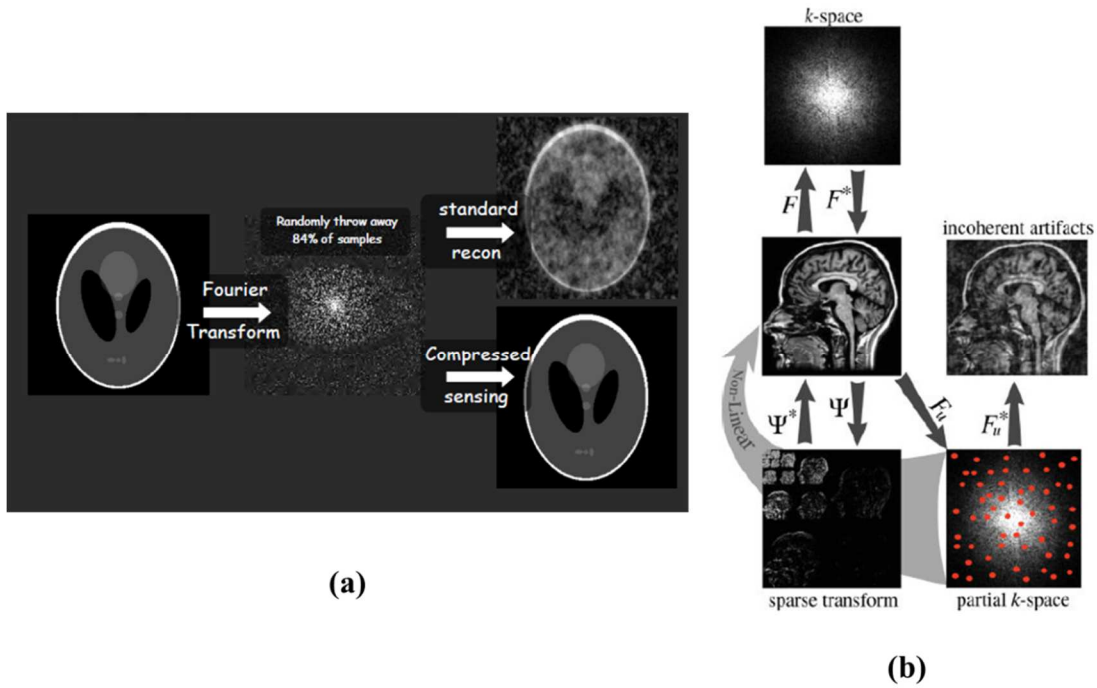
Figure 2.7 (a) An illustration of pseudo-random undersampling in CS. (b) various domains and operators in CS.

The first application of CS to MR imaging was by Lustig *et al* [70]. The application of CS to ^{1}H MRSI was investigated by Geethanath *et al* for various acceleration factors, retrospectively [71]. Sampling masks were generated for various acceleration factors, namely, two, three, four, five, and ten using variable density random undersampling. A two dimensional probability density function was used to select the random samples, ensuring a denser sampling at the center of k-space and sparser sampling of points towards the periphery [71]. The reconstructions at various acceleration

factors preserved the fidelity of the metabolite spectrum when compared with the fully sampled conventional MRSI datasets. The algorithm broke down at an acceleration factor of ten, wherein the metabolite peaks began to show increased signal intensities when compared to the conventional MRSI datasets. The reconstruction, thus, faithfully preserved the prognostic and diagnostic value of the metabolite maps up to an acceleration factor of five; this retrospective study was an important first step that demonstrated the feasibility of the approach (Figure 2.7) [71].

CS has been employed to accelerate multidimensional spectroscopic imaging in recent clinical studies [77-79]. A 4D echo planar imaging sequence based on J-resolved spectroscopy was implemented using CS to achieve a high acceleration *in vivo*, demonstrating the utility of multidimensional MRSI [77-79]. The CS technique has also been applied to ^{13}C 3D MRSI, in the design and testing of a CS based new EPSI sequence [80, 81]. Hyperpolarized ^{13}C data are well suited for CS applications due to the fundamentally sparse spectrum and high SNR resulting from hyperpolarization [80, 81]. The T_1 decay of the hyperpolarized signal restricts the amount of time available for signal acquisition in the time-window when SNR is high, thus, necessitating the use of accelerated imaging techniques for optimal spatial coverage and speed. The sequence proposed by Hu *et al* achieves an acceleration factor of up to 7.53, and minimal artifacts in the reconstruction for 3D MRSI [81]. A time-resolved 3D MRSI technique has been developed by Larson *et al* [82] for monitoring the dynamics of pyruvate conversion to alanine and lactate in a mouse model. This method effectively utilizes the magnetization through the use of multiband excitation pulses in combination with CS for increased acceleration [82].
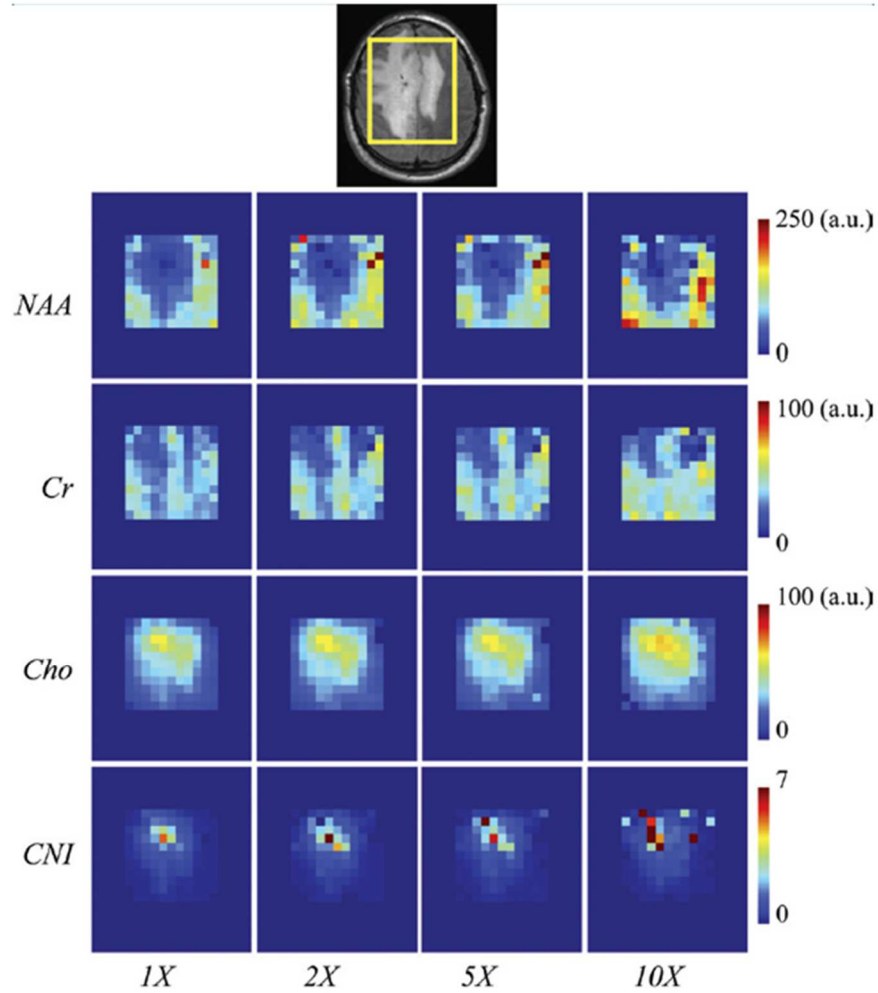
Figure 2.8 The retrospective application of CS-MRSI demonstrated in a brain tumor patient. Representative metabolite maps of NAA, creatine (Cr), choline (Cho), and choline to NAA index (CNI) for various acceleration factors. Reproduced from reference [71].

The CS technique has also been applied to ^{31}P MRSI of the human brain by Askin *et al* [83]. The long scan times associated with ^{31}P MRSI restrict its widespread use in the clinic. Furthermore, ^{31}P MRSI requires larger voxels and increased signal averaging to obtain adequate SNR as the signal from ^{31}P is approximately 15 times less MR sensitive than that from protons. In this study, a higher SNR was observed in the CS reconstructed data, while the peak height ratios of the original and CS datasets were comparable [83].

Recent promising preclinical applications of CS MRSI *in vivo* include [19]F 3D spectroscopy in mice [84] wherein the non-existent background signal in ^{19}F MRSI makes it particularly suited to satisfy the sparsity constraint that is integral to CS. Exogenously administered ^{19}F MRSI has several markers with unique spectral signals that can be well detected in the presence of a negligible background signal. Kampf *et al* demonstrated the retrospective application of CS based ^{19}F MRSI both *in vitro* and *in vivo*, with the CS reconstructions preserving the fidelity of the data up to an acceleration factor of 8 [84]. The first application of high resolution [23]Na spectroscopic imaging in mouse hearts was recently demonstrated by Maguire *et al* [85]. The ^{23}Na MRSI data from *in vivo* mouse hearts were prospectively undersampled by 3X and reconstructed using the CS algorithm previously described in [71], to yield undersampled reconstructions that preserved the fidelity of the data.

2.3.5 Hybrid Fast MRSI & Other Contributions

The two major categories of MRSI acceleration techniques are not exclusive and various novel combinations can be implemented to gain more speed, as has been the case in MRI. Various methods have been broadly classified into the discussed two main categories according to the dominant effect and there are no efforts to suggest exclusivity of these two categories when describing any technique. Various studies have focused on combining acceleration techniques to further reduce scan times and overcome some of the limitations of individual high-speed techniques in MRSI [86-91]. All these hybrid techniques try to achieve the best trade-off between gain in speed and optimal SNR, resolution, and resulting artifacts.

2.4 Implications of Accelerated MRSI & Future Directions

The future holds promise for the development of various hybrid techniques, particularly those involving CS, parallel imaging, and novel k-space trajectories, to achieve further reduction in scan times and better image quality in terms of the SNR, spatial and temporal resolution, and artifact reduction. CS based pulse sequence design has several potentially beneficial implications in the clinical scenario. Larger matrices offer more sparsity to exploit and the increased room for undersampling could lead to even higher acceleration factors. This technique could also be used to cover larger FOVs in the clinical setting. Gradient amplitude constraints would not impose a limitation on the design as the FOVs in clinical applications tend to be at least an order of magnitude higher than those typically used in preclinical studies. CS reconstructions can be used to further accelerate scan times when datasets of higher order dimensions are collected. The inherent sparsity along an increased number of dimensions can be fully exploited by only collecting specific phase encode values along each additional spatial dimension. Furthermore, a key point to be noted is that the benefits of under-sampling along the temporal dimension are not as significant as those along the phase encode dimensions due to the nature of MR signal acquisition. One exception is the EPSI approach, which (even under fully sampled conditions) does not sample the time dimension continuously and hence lends itself to temporal under-sampling quite well [50]. However, more sophisticated reconstruction routines could be developed even for conventional readouts to exploit sparsity along the spectral dimension, with a goal of improving SNR or further reducing the scan time.

All discussed high-speed MRSI techniques have been extensively employed in studies of the brain and to a large extent in the prostate. However, there is limited research in other organs like the breast, abdomen, etc. The application of MRSI to many other organ systems is often limited by low SNR, contamination from peripheral lipid signals (in turn restricting short TE acquisitions), higher field inhomogeneity, and motion artifacts. With increasing acceleration, a drop in SNR is observed when employing fast techniques, except in CS where denoising leads to improved SNR at higher acceleration factors. Other aspects to be considered include eddy current artifacts, the achievable spatial resolution, and the need for fast gradient systems that are often not implementable due to hardware limitations. Non-proton MRSI is also limited by very low MR signal sensitivity, making its clinical translation difficult.

Several processing steps are usually required for the complete analysis of MRSI data, and the processing methods vary for different data types as well [23]. This technique is less appealing to the radiologist due to a lack of standardization in MRSI acquisition protocols, and the non-availability of common processing and analysis tools for a quick and simple representation of metabolite concentration maps. Automation and quality control are of critical importance in accelerated MRSI techniques that frequently experience poor spectral quality due to SNR losses, lipid contamination, hardware limitations, and miscellaneous other artifacts. Ultra-fast CSI acquisition techniques also necessitate the use of more sophisticated reconstruction algorithms and complex spatial-spectral analysis to minimize the reconstruction errors from the sparse acquisitions. Implementation of advanced algorithms and routines on the scanner for 'on the fly' reconstruction and complex spectral analysis is not a trivial task. One must also take into

account the additional time required for reconstruction, post processing, and display of metabolite maps. Furthermore, it is important to note that high-speed MRSI techniques are only acceptable in applications wherein conventional phase-encoded MRSI is itself not SNR limited at the desired spatial resolution. The SNR penalty in conventional MRSI is often large to begin with, particularly when imaging difficult regions, which tends to get further aggravated when employing accelerated CSI techniques.

Another concern in spectroscopic imaging is the effect of the acceleration technique on the PSF and cross-contamination of information between neighboring voxels. For e.g. in turbo MRSI, the reduced echo duration caused a broadening of the spectral PSF, with phase distortions leading to further PSF degradation [36]. Variable density-weighted trajectories tend to suppress the side lobes of the PSF as compared to uniformly-weighted/non-weighted acquisition schemes. Spiral sampling trajectories also tend to have reduced ringing and a narrower central PSF lobe as compared to the elliptical sampling scheme; variable-density spirals can be employed to further reduce the side lobes and ringing [92]. In SENSE spectroscopic imaging, the spatial response function (SRF) tends to slightly vary between voxels and is affected by the sensitivity relations [62]. In wavelet-encoded MRSI, the PSF is a function of the wavelet shape, and in turn of the RF pulse profile [69]. In fast techniques like CS, a coherent broadening of the PSF is avoided due to the incoherent nature of undersampling, resulting in noise-like artifacts [70, 71]. On the other hand, high-speed techniques can help in reducing blurring and streaking artifacts, especially while imaging organ systems that are susceptible to motion. Fast MRSI will also aid in higher volume coverage, incorporation of specialized techniques like spectral editing for mapping metabolites like lactate and gamma-amino-

butyric acid (GABA) that typically require more averaging to obtain optimal SNR. Other techniques like J-resolved spectroscopy and correlation spectroscopy (COSY) could also be incorporated into current clinical protocols to obtain high resolution spectroscopy data [77, 79, 93].

Thus, the acceleration offered by high-speed techniques can either be employed to decrease the scan time, leading to reduced motion sensitivity and patient discomfort, or the time-saving can traded for higher SNR/resolution and/or for imaging a larger volume of interest. The reconstruction and quantification of sparsely-sampled spectroscopic data on the scanner immediately following data acquisition will also help establishing the need for inclusion of fast MRSI techniques into current imaging protocols.

(**Note:** Chapter 2 is based on the paper – "Fast Data Acquisition Techniques in Magnetic Resonance Spectroscopic Imaging", R. Vidya Shankar, J. C. Chang, H. H. Hu, and V. D. Kodibagkar, Submitted to *NMR in Biomedicine*, under review.)

CHAPTER 3

PRE-CLINICAL APPLICATIONS OF CS-MRSI

MRSI has several applications in the preclinical setting for a non-invasive mapping of biochemistry *in vivo*. The objective of this study was to accelerate spectrally-edited MRSI on a preclinical MRI scanner to achieve rapid spectroscopic imaging of lactate levels in solid tumors and evaluate subsequent changes in response to therapy.

3.1 Lactate-selective CS MRSI

3.1.1 Why Image Lactate?

Lactate plays a critical role in the development and metastasis of cancer, and its accumulation is readily seen in solid tumors [30, 94]. Under normoxic conditions, glucose metabolism is a highly energy efficient process, producing 38 adenosine triphosphate (ATP) molecules on the complete oxidation of one glucose molecule, along with water and CO_2 [95]. In differentiating cells, glucose is converted to lactate (via pyruvate, Figures 3.1 and 3.2) when oxygen is limited to produce 2 ATP molecules/glucose molecule. However, even in the presence of ample oxygen, cancer cells tend to preferentially metabolize glucose by aerobic glycolysis, which is a less efficient pathway for ATP production, generating only 4 ATP molecules/glucose molecule as compared to oxidative phosphorylation [30, 94-96]. This phenomenon is known as the Warburg effect [96], wherein glucose is preferentially catabolized to lactate in the presence of adequate oxygen. Thus, the build-up of lactate in solid tumors is suggestive of altered metabolism and possibly indicates the presence of hypoxia.

Lactic acid has also been found to stimulate angiogenesis, promote inflammation, and contribute to the immune escape [30, 94]. The elevated lactate levels seen in biopsy samples have been suggestive of an increased risk of tumor metastasis, recurrence, and radio resistance leading to poor therapeutic outcomes in cancers of the head and neck, breast, and cervix, while cancer response to chemotherapy has indicated a decrease in the steady-state tumor lactate levels [97-102]. A dedicated technique like magnetic resonance spectroscopic imaging (MRSI) can be employed for mapping the spatial distribution of lactate in solid tumors *in vivo*. This could potentially lead to improved cancer targeting and therapy, and the possibility of employing non-invasive lactate imaging as a prognostic marker in the clinic to monitor the dynamic changes in lactate concentration both pre- and post-therapy [103-105].
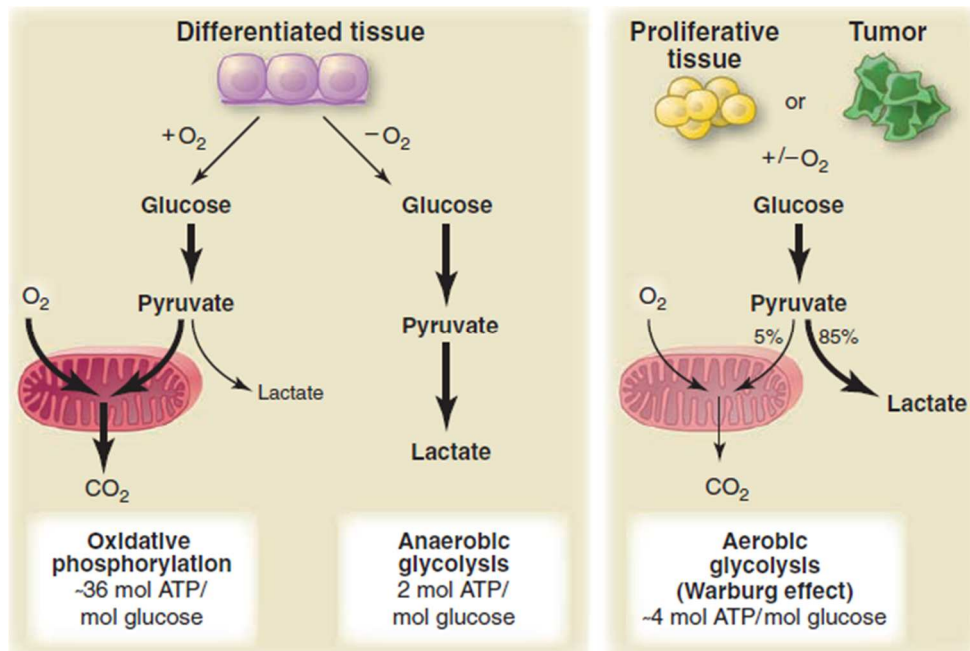
Figure 3.1 An illustration of cellular energy processes, namely, oxidative phosphorylation, anaerobic glycolysis, and aerobic glycolysis (also called the Warburg effect). Reproduced from [96].
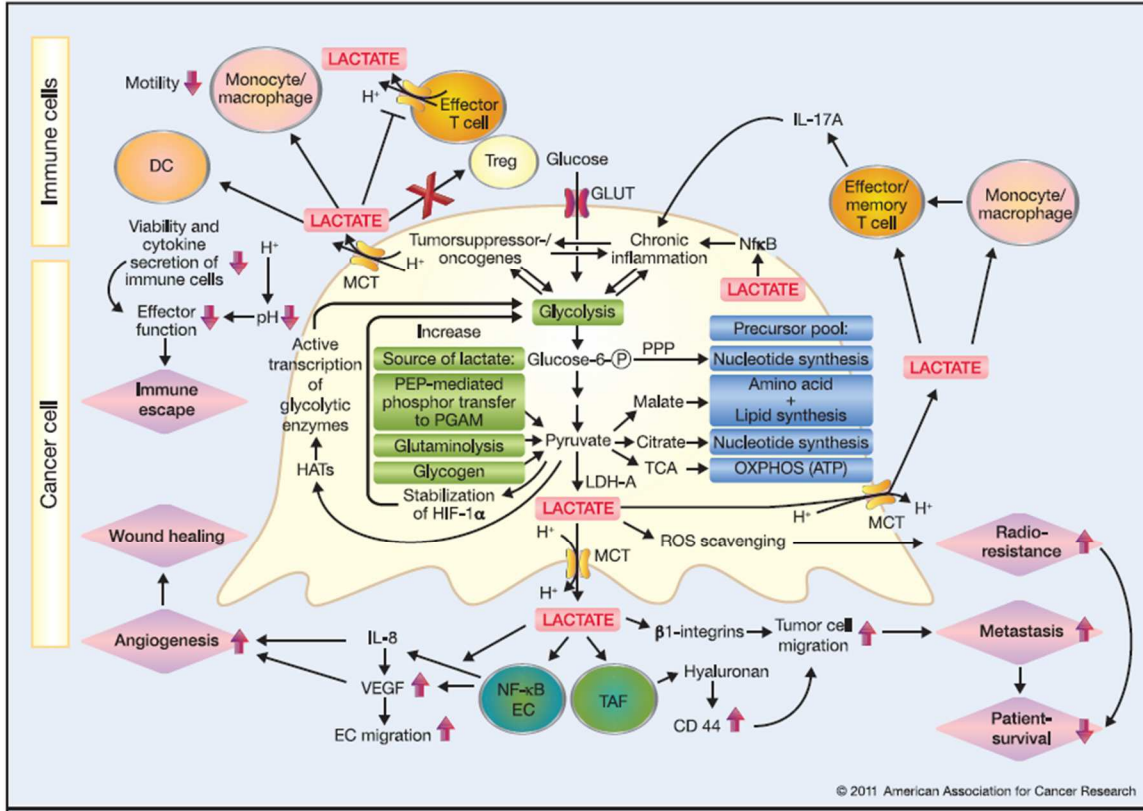
Figure 3.2 The role played by lactate in various cancer pathways and processes. Reproduced from [94].

3.1.2 Lactate Detection in Proton MRSI

As previously discussed in Chapter 1 section 1.3.4, lactate is essentially a J-coupled metabolite, with the methine (-CH) and methyl groups (-CH$_3$) forming an A$_3$X spin system [29]. Even at low magnetic fields, the scalar-coupled spin system of lactate is considered to be weakly coupled [24]. The -CH$_3$ moiety is responsible for the doublet located at 1.31 ppm in the NMR spectrum, while the –CH moiety is responsible for the quartet at 4.1 ppm (Figure 3.3). The doublet is more commonly acquired but accurate detection and quantification are often complicated by the presence of macromolecules and huge overlapping resonances from lipid in the 0.8 – 1.3 ppm range. It is often difficult to detect the quartet at 4.1 ppm *in vivo* due to its proximity to water. To

overcome the above limitations, several spectral editing techniques have been developed for accurate acquisition of the lactate resonance [106-108]. Longer echo times (TE) are usually employed when acquiring the lactate peak to minimize contamination from the lipid resonances.
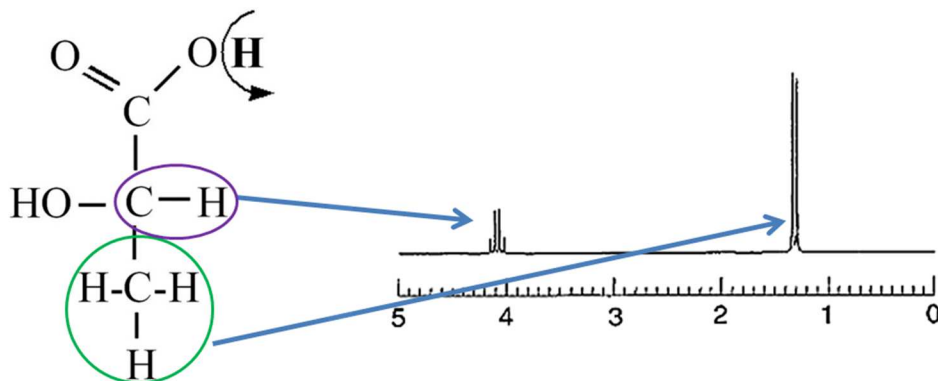
Figure 3.3 An illustration of the lactate molecule and its corresponding NMR spectrum. The CH3 group produces the doublet at 1.31 ppm, while the CH moiety is responsible for the quartet located at 4.1 ppm.

3.1.3 The Sel-MQC Sequence

Spectral editing techniques seek to separate the overlapping resonances and quantify the harder to detect metabolites like lactate, citrate, GABA (γ-Aminobutyric acid), and 2-hydroxyglutarate (2HG) to name a few. Such low concentration metabolites can be selectively recorded with specific acquisition schemes that retain only the metabolite peaks of interest, while eliminating any interfering resonances particularly those from water and fat [109]. Pulse sequence optimization and a strict assessment of the specificity achieved by the editing technique will ensure a more reliable detection of these smaller metabolites [109].

The selective multiple-quantum coherence transfer (Sel-MQC) sequence developed by He *et al* [106] is one such spectral editing sequence that achieves selective

excitation of the lactate doublet, while effectively suppressing the peaks from lipid and water. A 2D MRSI implementation of the Sel-MQC sequence is depicted in Figure 3.4 (adapted from [106]), and involves the three distinct stages elucidated below for lactate excitation, selection, and detection.

(a) Preparation

The first part of the pulse sequence involves converting the lactate resonance into the multiple quantum coherence (MQC) state. A frequency-selective $90°$ RF pulse is applied to excite fat and the CH_3 moiety corresponding to the lactate doublet. Scalar coupling (J), chemical shifts (ω_0), and B_0 field inhomogeneity effects contribute to the evolution of these single quantum coherences (SQCs). Following time $\tau = 1/2J$, where $J = 6.93$ Hz for lactate, a second 90^0 pulse is applied at the -CH peak frequency to convert the lactate magnetization into the MQC (zero and double quantum coherences, ZQ and DQ) mode, while all other resonances remain in the SQC mode.

(b) Gradient Selection & Labeling

A set of coherence selection gradients, namely g_1, g_2, and g_3, are applied in a specific ratio to select either the ZQ $\rightarrow$ DQ (0:-1:2) or DQ $\rightarrow$ ZQ (1:0:2) pathway of lactate. These coherence selection gradients act as a multiple quantum filter allowing only the MQCs from lactate to pass through, while at the same time dephasing all resonances in the SQ mode. The CH_3-selective $180°$ pulse applied in the middle of the gradient labeling period helps to refocus the B_0 inhomogeneity and chemical shift, and eliminate J-modulation effects.

(c) Detecting the lactate doublet

The final stage of the pulse sequence involves acquiring the lactate doublet. A CH-selective 90° 'read' pulse applied at the beginning of the detection period converts the MQCs of lactate back into the SQ mode. This is necessary as the final signal can only be detected and acquired when in the SQ mode. The gradient g_3 applied during the time interval $\tau' = \tau - t_1$ (for the chosen ZQ $\to$ DQ pathway, figure not to scale) refocuses the pathway selected during the prior gradient labeling period.
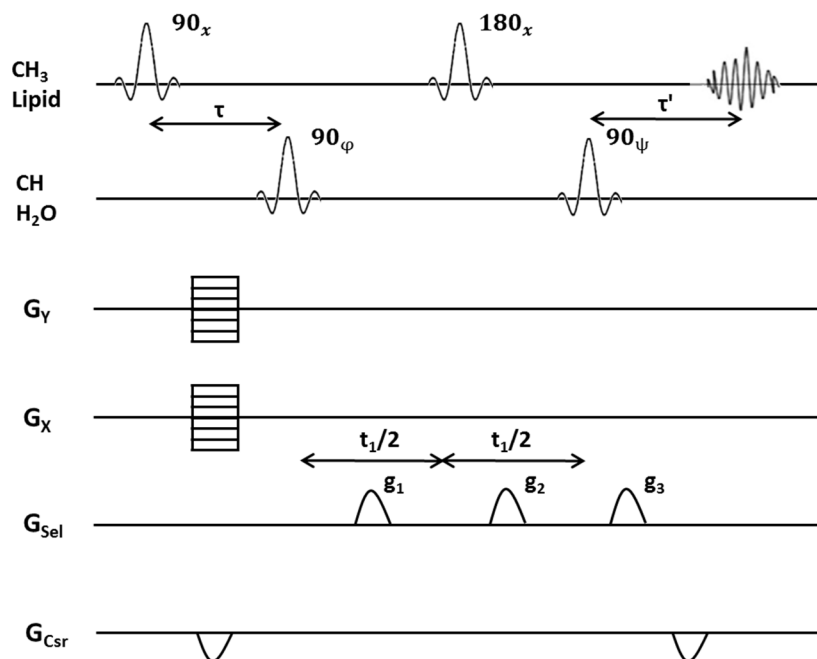
Figure 3.4 A 2D MRSI pulse sequence with lactate-specific editing based on the Sel-MQC technique. Adapted from [106].

Selection of either the ZQ $\to$ DQ or DQ $\to$ ZQ pathway allows a 50% recovery of the lactate signal intensity. Both pathways need to be refocused simultaneously to obtain complete recovery of the lactate signal. All other resonances experience a set of unbalanced gradients and are completely dephased.

49

3.1.4 Key Aspects to Fast Lactate Imaging

The aim of this study was to achieve rapid imaging of the lactate resonance by implementing a 2D MRSI version of the Sel-MQC sequence, with pseudo-random undersampling of the phase encodes G_x and G_y (shown in Figure 3.4) to facilitate CS acquisition and reconstruction. A schematic of the proposed fast lactate imaging method is depicted in Figure 3.5.
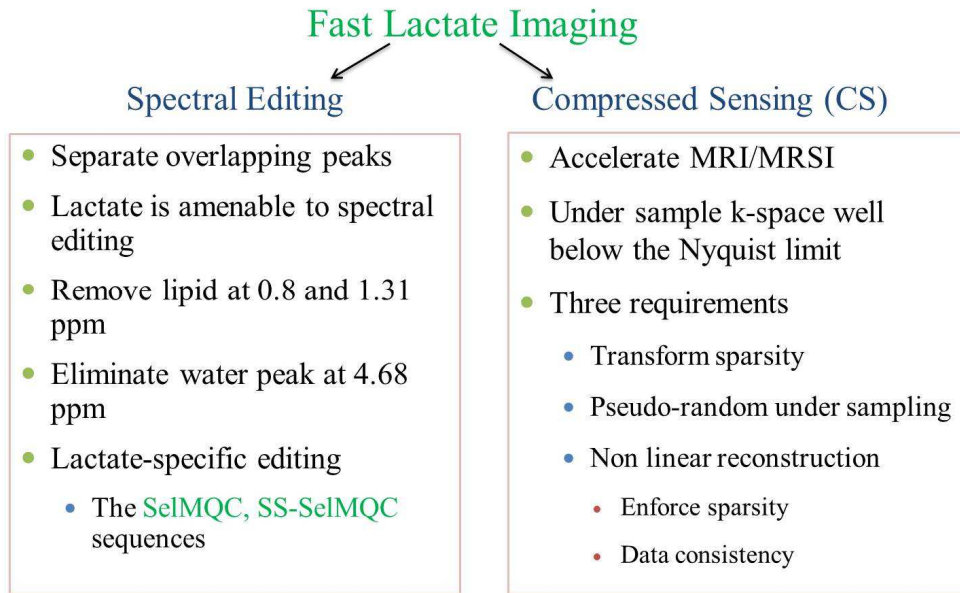
Figure 3.5 An illustration of the two key aspects in fast lactate imaging, namely lactate-selective spectral editing (SelMQC [106], SS-SelMQC [107]) and CS acquisition and reconstruction [70, 110].

The objective of this study was to incorporate spectral editing components for the selective excitation of the lactate resonance along with prospective undersampling of the k-space to facilitate rapid CS accelerated MRSI of lactate *in vivo*. The nuisance signals are filtered out by spectral editing leading to a reliable detection of the lactate peak. Combined with CS acquisitions, the developed sequence, referred to henceforth as the lactate-CS-MRSI sequence, with enable the high-speed detection of lactate with finer

precision. The implementation of the proton lac-CS-MRSI sequence and its applications both *in vitro* and *in vivo* will be elucidated in the following sections.

3.1.5 Materials & Methods

MRSI Pulse Sequence for Rapid Lactate Mapping

The lactate-CS-MRSI pulse sequence, depicted in Figure 3.4, was developed in the Bruker ParaVision 5.1 environment. Two key modifications were made to a conventional MRSI pulse sequence: (1) Spectral editing components based on the SelMQC technique [106] were added to enable selection of the ZQ → DQ pathway of lactate. (2) Pseudo-random undersampling patterns that were generated 'on the fly' on the scanner (based on the acceleration factor input by the user) were employed to undersample the phase encodes G_x and G_y depicted in Figure 3.4 to facilitate prospective CS acquisitions.

MRSI Data Acquisition

All experiments were conducted on a Bruker BioSpec® 7 Tesla (7T) preclinical magnetic resonance imaging (MRI) scanner. The developed lactate-CS-MRSI sequence was initially tested and optimized on phantoms containing deionized water/oil/lactate (5 mM). MR acquisition parameters were as follows: 16 x 16 x 4096 matrix, 40 x 40 mm^2 FOV, TE/TR = 144/1500 ms, 2 mm slice thickness, number of averages = 1, spectral width = 4006.41 Hz, dwell time = 249.6 μs. *In vivo* studies involved cohorts of nude mice subcutaneously implanted with H1975 (non-small cell lung cancer, nsclc) tumors in the right thigh. All animal studies were approved by the Institutional Animal Care and Use

Committee. A cohort of n = 6 nu/nu tumor mice was employed for testing and optimizing the lactate-CS-MRSI sequence *in vivo*. Tumors were allowed to grow to 1 cm^3 prior to conducting MRSI experiments. Animals were passively restrained throughout the experiment and were anesthetized via isoflurane gas inhalation (1.5 %). *In vivo* experiments were conducted using a surface receive coil combined with a 72 cm volume transmit coil. The subcutaneous thigh tumor was carefully placed under the surface coil and the animals were positioned on a warm heating pad connected to a circulating water bath set to operate at 37 ^{o}C, to keep them warm during the experiment. The fully sampled reference MRSI acquisition (1X), along with datasets corresponding to various acceleration factors, namely 2X-5X and 10X, were acquired for each experiment. MR scan parameters: 16 x 16 x 2048 matrix, 27.2 x 27.2 x 3 mm^3 FOV, TE/TR = 144/1500 ms, number of averages = 8, spectral width = 4006.41 Hz, dwell time = 249.6 μs.

CS-MRSI Reconstruction

A custom non-linear iterative reconstruction based on the conjugate gradient algorithm was implemented in Matlab (The Mathworks Inc., MA) to reconstruct all the lactate-CS-MRSI datasets. The CS-MRSI reconstruction was formulated as a convex optimization problem, which involved minimizing the following cost function [71]:

$$\varepsilon(m) = \|F_u m - y\|_2 + \lambda_{L1}\|Wm\|_1 + \lambda_{TV}TV(m) \tag{3.1}$$

where, y is the measured k-space data, m is the desired MRSI data, F_u, W, and TV are the Fourier transform, wavelet transform, and total variation operators, respectively, $\|.\|_1$ and $\|.\|_2$ are the l_1 and l_2 norm operators, respectively, and, λ_{LI} and λ_{TV} are the corresponding regularization parameters for the L$_1$ norm and TV operator, respectively.

The k_x - t matrix was encoded along each of the two dimensions using the Daubechies wavelet transform at all points in k_y. The regularization terms λ_{TV} and λ_{LI} were experimentally determined to be 0.005 and 0.001, respectively. Eight iterations were found to be optimal to obtain convergence of the cost function.

Post processing, Error Metric and Statistical Analysis

All reconstructed lactate CS-MRSI datasets were quantitatively compared with the 1X fully sampled reference dataset by evaluating metrics like the SNR, lactate peak amplitude, and the total acquisition time. In each case, the error in reconstruction, as defined by the root mean square error (RMSE) metric was calculated as:

$$RMSE = \sqrt{\frac{1}{N}\sum_{i=1}^{N}(y_i - y_i')^2} \tag{3.2}$$

Where, N is the total number of points in the MRSI dataset, y is the reconstructed data from the fully-sampled (1X) k-space, and y' is the data reconstructed from undersampled k-space. The RMSE defined here can be considered to be equivalent to the normalized RMSE as the data range was normalized from 0 to 1. The jMRUI [111] software package was employed to apply the following minimal post-processing operations to all the reconstructed MRSI datasets: (a) apodization to eliminate any truncation artifacts, (b) automatic/manual zero and first order phase correction, and (c) Generation of lactate maps using AMARES [111].

A voxel-wise 2-tailed paired t-test was applied to the lactate maps generated from each reconstructed dataset with the fully sampled reference dataset using the GraphPad

Prism (San Diego, CA, USA) scientific software. A p-value < 0.05 was considered statistically significant and indicative of an incorrect reconstruction.

3.1.6 Results

Figure 3.6 shows results from the phantom experiments. The lactate-CS-MRSI sequence was able to eliminate the water and fat resonances, while enabling selection of lactate from the innermost tube of the phantom. Undersampled MRSI datasets corresponding to acceleration factors 1X – 10X were prospectively acquired and reconstructed using the procedures outlined previously.
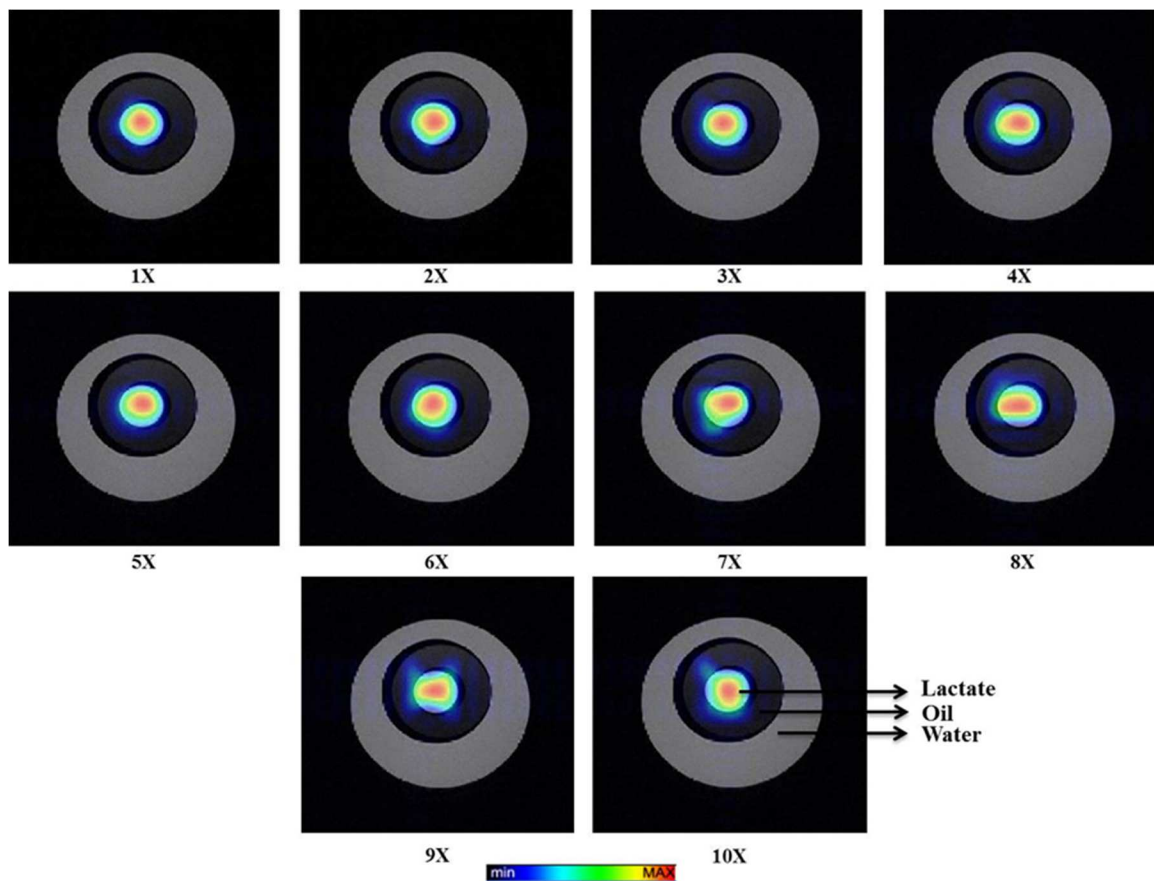
Figure 3.6 The water/oil/lactate (5 mM) phantom. An illustration of reconstructed MRSI datasets corresponding to different undersampling factors (from left to right): 1, 0.5, 0.33, 0.25, 0.2, 0.17, 0.14, 0.12, 0.11, and 0.1, respectively.

54

Total acquisition time – 6 min 30 s (1X), 3 min 18 s (2X), 2 min 7 s (3X), 1 min 36 s (4X), 1 min 17 s (5X), 1 min 6 s (6X), 54 s (7X), 47 s (8X), 42 (9X), and 38 s (10X). As can be seen from the figure, the CS-MRSI reconstructions of the lactate peak maintain good fidelity even up to 10X, with no statistical significance seen between the fully sampled 1X reference and undersampled reconstructions (i.e. $p > 0.05$).

The developed sequence was subsequently tested *in vivo* in a cohort of nu/nu mice (n = 6) subcutaneously implanted with H1975 (non-small cell lung cancer, nsclc) tumors in the right thigh. The results from the *in vivo* experiments are depicted in Figures 3.7 - 3.9. In Figure 3.7, all reconstructions 1X – 5X show the same distribution of lactate and no statistically significant differences were observed expect between 1X and 4X ($p < 0.05$). Figure 3.9 shows additional results from the *in vivo* cohort (same acquisition parameters), with 2X – 5X lactate reconstructions maintaining high accuracy with the 1X reference.

The RMSEs from the phantom experiment are shown in Figure 3.8 (a). The RMSE remains below 5% for accelerations up to 6X, with increasing deviations seen with increasing acceleration. However, even between 7X – 10X, the RMSE was found to be under 8%, with high accuracy in the reconstruction of the lactate peak. Figure 3.8 (b) depicts the mean nRMSE ± standard deviation for the *in vivo* cohort of H1975 mice. As seen in the figure, reconstruction errors are between 2% - 6% for reconstructions 2X – 5X. The low standard deviation values, particularly at 3X and 4X indicate consistent reconstruction errors in the entire cohort of n = 6 animals.
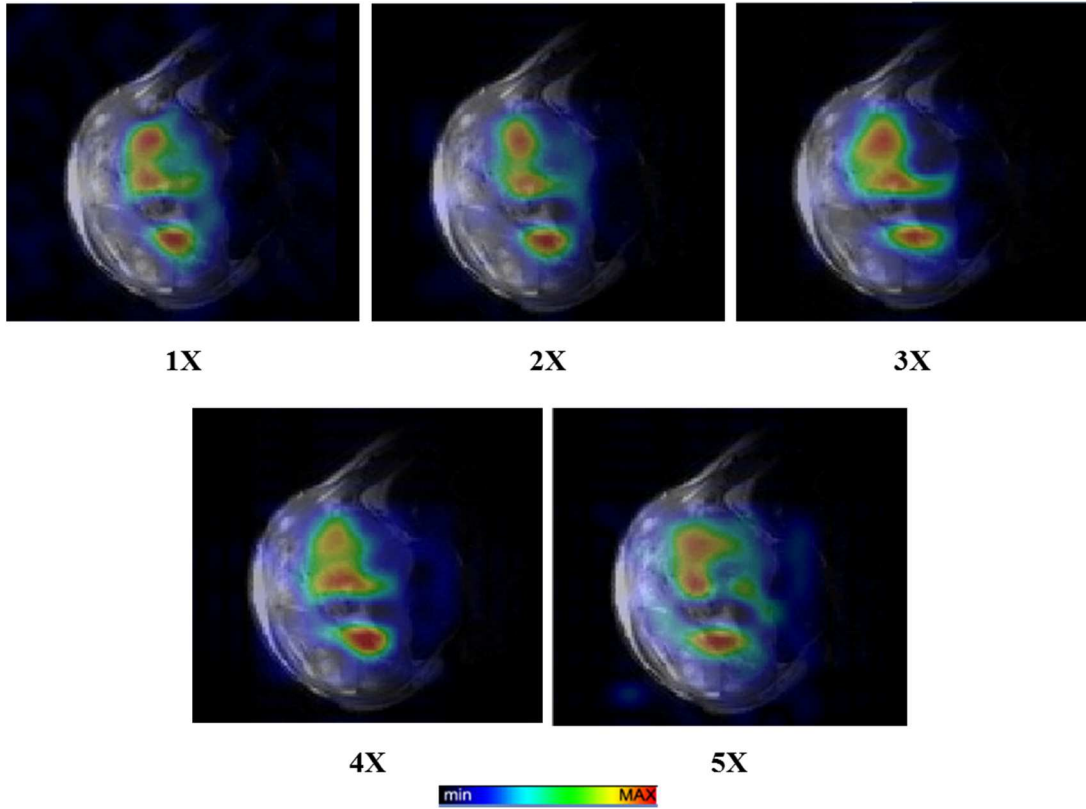
Figure 3.7 Reconstructed MRSI datasets showing the distribution of lactate in a H1975 tumor implanted subcutaneously on a mouse thigh. Total acquisition time – 51 min 12 s (1X), 25 min 36s (2X), and 10 min 24 s (5X). The p-value for the 1X vs 2X case is 0.26, while that for the 1X vs 5X case is 0.49, indicating no statistically significant differences (p>0.05) between the undersampled and fully-sampled reference reconstructions.

(a)

(b)
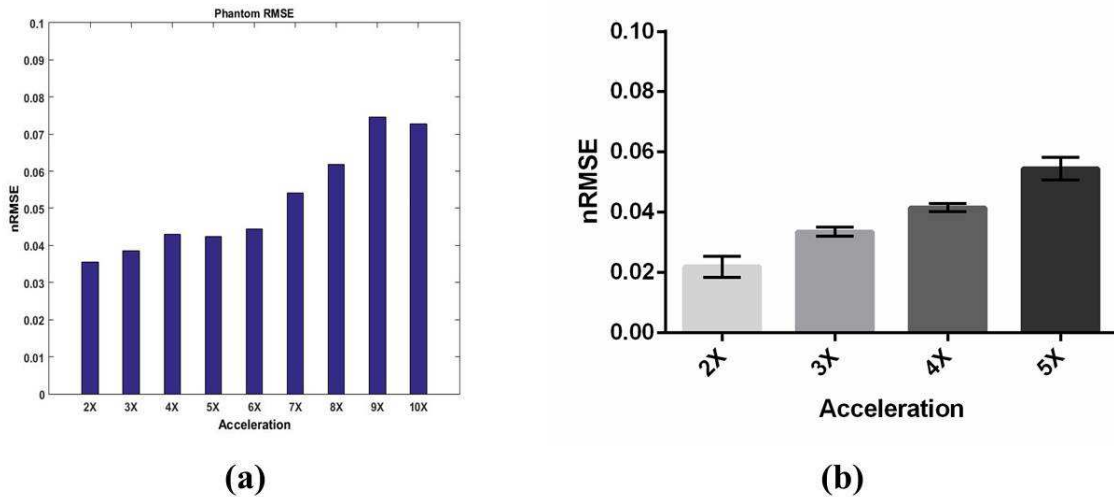
Figure 3.8 RMSEs from the in vitro and in vivo experiments. (a) The normalized RMSEs from the phantom experiment for acceleration factors 2X – 10X. (b) The mean nRMSEs ± standard deviation for the H1975 cohort.
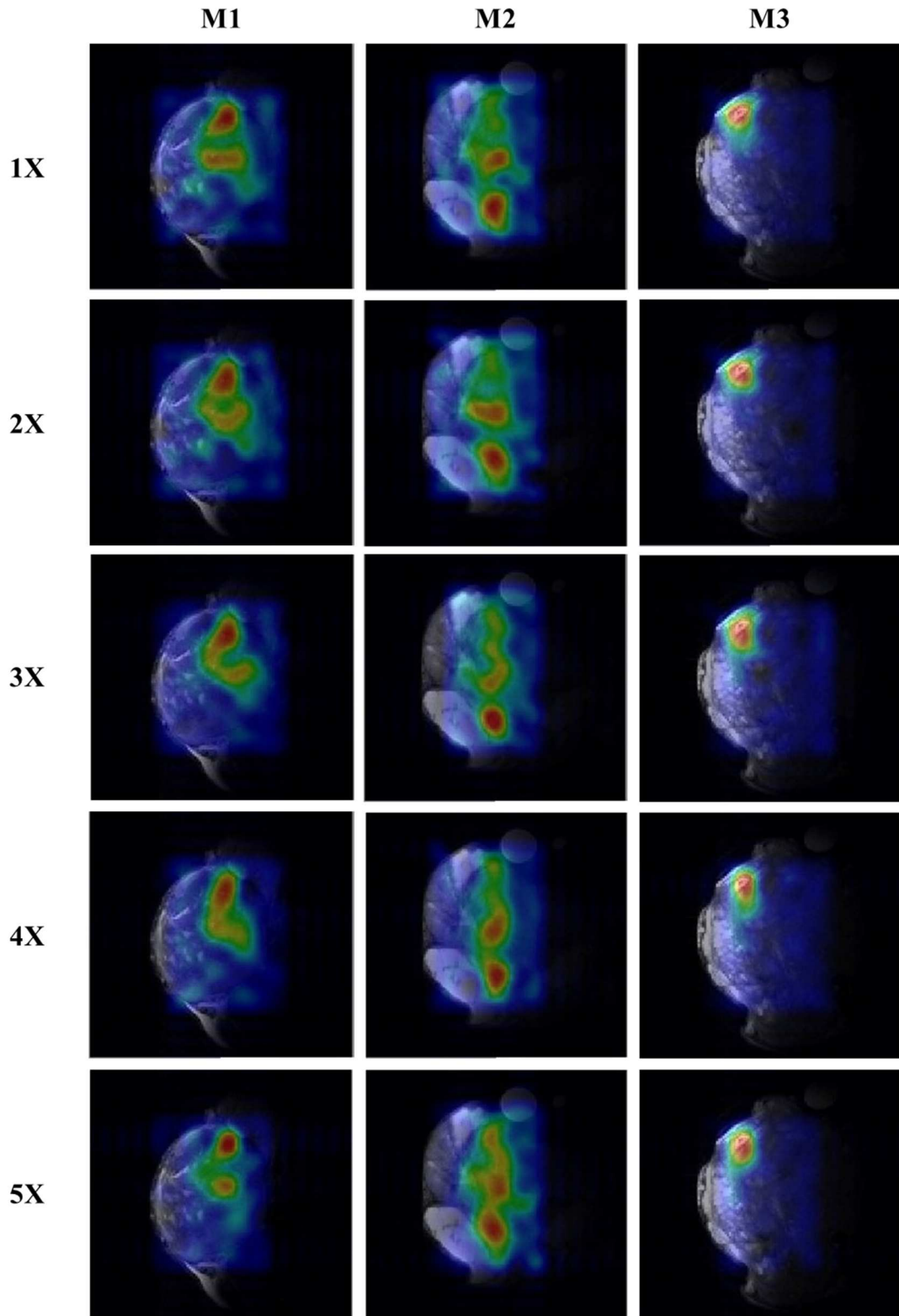
Figure 3.9 Lactate-CS-MRSI datasets from the in vivo cohort. High fidelity can be seen between the 1X and 2X – 5X reconstructions of the lactate peak ($p > 0.05$).

3.2 Assessment of Lactate Changes using Combretastatin A4 Phosphate

3.2.1 CA4P

The lactate-CS-MRSI sequence was also used to assess the dynamic changes in cancer metabolism in response to therapy using the prodrug combretastatin A4 phosphate (CA4P) [112-114]. CA4P is essentially a tubulin-binding agent that rapidly disrupts and shuts down the tumor vasculature upon administration. The vascular endothelium of the tumor is an important target in cancer therapeutics as the continued growth and survival of solid tumors is heavily dependent on the vasculature, which sustains malignant growth by supplying oxygen and nourishment [114]. Thus, disrupting the vascular functionality of cancer cells is a key approach to a quick and catastrophic destruction of the tumor, by inducing nutrient deprivation and hypoxia [113, 114]. CA4P belongs to the class of compounds isolated from the South African tree *Combretum caffrum* [113], and is responsible for causing fast and prolonged interruption of blood flow leading to extensive necrosis in the tumor cells within 24 hours of administration (Figure 3.10).

Various qualitative and quantitative techniques have been employed to capture the rapid changes in solid tumors induced by CA4P treatment [115-123]. Modalities like positron emission tomography (PET) measure changes in tumor perfusion and blood volume using ^{15}O-labeled water ($H_2^{15}O$) and carbon monoxide ($C^{15}O$) [117]. The increased glucose uptake by solid tumors as compared to normal tissues can be exploited for tumor diagnostics, anti-cancer therapy, and in the detection of metastasis using FDG-PET. Other imaging modalities include *in vivo* near infrared spectroscopy (NIR) combined with diffusion weighted (DW) MRI to monitor changes in vascular perfusion, tumor oxygenation (pO_2) and necrosis in response to CA4P treatment [121], NIR

combined with laser Doppler flowmetry to assess variations in blood flow and perfusion [116], fluorescence and bioluminescence imaging (BLI) to measure light emission kinetics [123], and dynamic contrast enhanced (DCE) computed tomography (CT) for a quantitative evaluation of the spatial heterogeneity in tumor vascularity as a marker of angiogenesis over the entire tumor volume [119]. Various MRI techniques have also been implemented to capture tumor dynamics upon CA4P administration, such as DCE MRI to study vascular permeability and perfusion [118], dynamic bioluminescence imaging (BLI) combined with MRI to examine changes in tumor growth and pO_2 [120], and MRS [124, 125] to map key metabolite concentrations (for e.g. lactate, choline, and citrate).
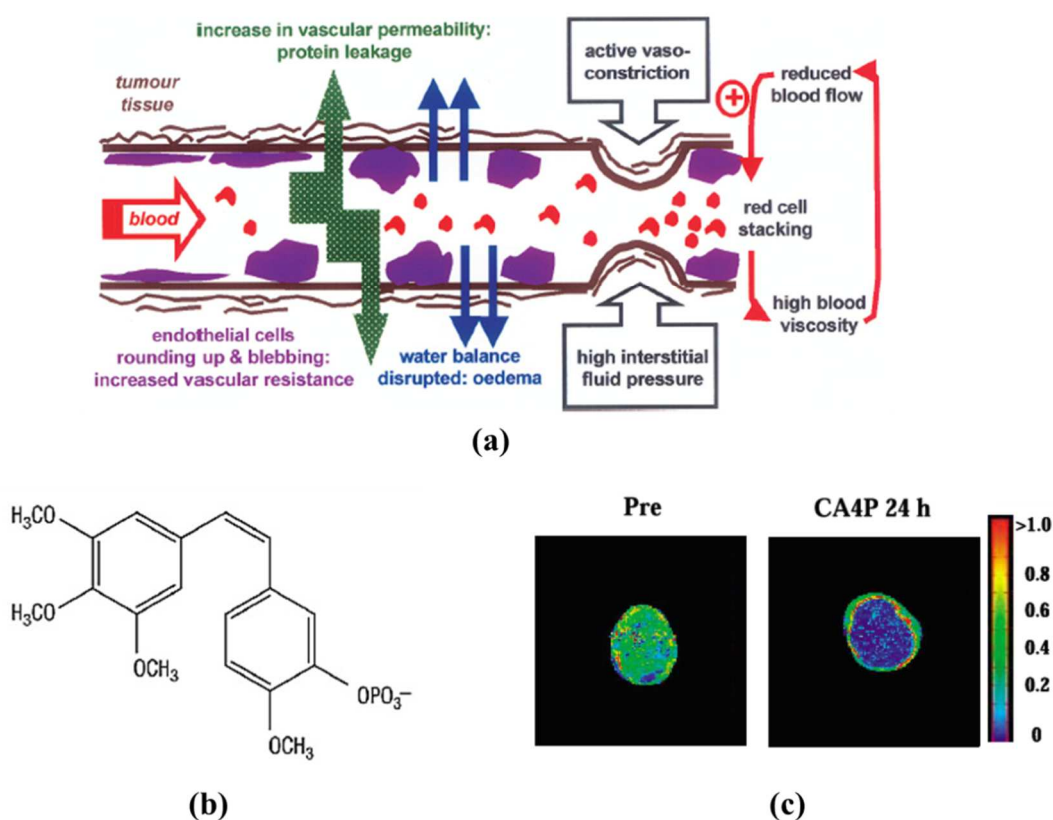
Figure 3.10 The mechanism of action of a vascular disrupting agent such as CA4P depicted in (a) and the CA4P molecule in (b). Results from DCE MRI both pre- and 24 hours post CA4P injection illustrated in (c), indicating a significant decrease in tumor perfusion. Reproduced from [126] and [118].

3.2.2 Methods

MRSI Experiments

Additional *in vivo* experiments were conducted to assess the effects of CA4P in altering the lactate metabolism of H1975 tumors. The lactate-CS-MRSI sequence was used to assess pre- and post CA4P treatment lactate levels for various acceleration factors. A cohort of n = 5 nu/nu tumor mice was treated with the CA4P prodrug (83 mg/kg body weight) and spectroscopic data was acquired using the lactate-CS-MRSI sequence both pre- and post-therapy. The general imaging sequence that was adopted while imaging each mouse is as follows: Baseline lactate-CS-MRSI scan (1X and 2X, 5X) – Inject CA4P – lactate-CS-MRSI scan (5X) – wait 24 hours – lactate-CS-MRSI scan (1X and 2X, 5X)**.** A second cohort of n = 5 nu/nu tumor mice was injected with dextrose and served as the control cohort. The same general imaging sequence described above was also adopted for the control cohort, and the lactate-CS-MRSI sequence was employed to acquire dynamic MRSI data both pre- and post-injection of dextrose.

3.2.3 Results

The results from the CA4P experiments are depicted in Figures 3.11 – 3.13. In each of the illustrated figures, the top panel shows the baseline lactate maps (1X, 2X, and 5X) from day zero i.e. prior to the injection of CA4P, while the bottom panel shows the corresponding lactate maps (1X, 2X, and 5X) from the same tumor cross-section 24 hours post the injection of the prodrug. All MRSI datasets were acquired with the following scan parameters: 16 x 16 x 2048 matrix, TE/TR = 144/1500 ms, 3 mm slice, N_{avg} = 4, FOV 3 x 3 cm^2, 1X scan time = 25 min 36 s. In four of the five animals of the

CA4P cohort, a decrease in total lactate levels was quantitatively measured 24 hours after the injection of CA4P, as can be observed from the lactate maps and the total integrated intensity of the lactate peak collated in Table 3.1. An increase in lactate was measured in one animal from the cohort 24 hours post administration as seen in Figure 3.13 (mouse 5 in Table 3.1).

A second cohort of nu/nu mice (n = 5) subcutaneously implanted with H1975 tumors in the right thigh served as the control cohort and were injected with dextrose. Figure 3.14 shows the results from the control cohort acquired with the same scan parameters listed earlier. The top panel shows the baseline lactate maps (1X, 2X, and 5X) from day zero i.e. pre dextrose injection, while the bottom panel shows the corresponding lactate distribution (1X, 2X, and 5X) measured from the same tumor cross-section 24 hours after the administration of dextrose. As expected, no significant changes were seen the total lactate distribution 24 hours post dextrose injection in the control cohort. The lactate maps from both the CA4P and control cohorts also indicate that the prospectively acquired accelerated reconstructions 2X and 5X maintain high fidelity with the 1X fully sampled reference MRSI dataset in each animal, as can be observed in Figures 3.11 – 3.14. Table 3.1 summarizes the lactate integrated intensities and pre/post ratios for accelerations 1X and 5X from both the CA4P and control cohorts.

The mean nRMSEs ± standard deviations from the CA4P and control cohort both pre and post injection in each case are depicted for accelerations 2X and 5X in Figure 3.15 (a) and (b), respectively. In both cohorts, the reconstruction error remains below 3% for the 2X, while the error does not exceed 5% in case of the 5X reconstructions.
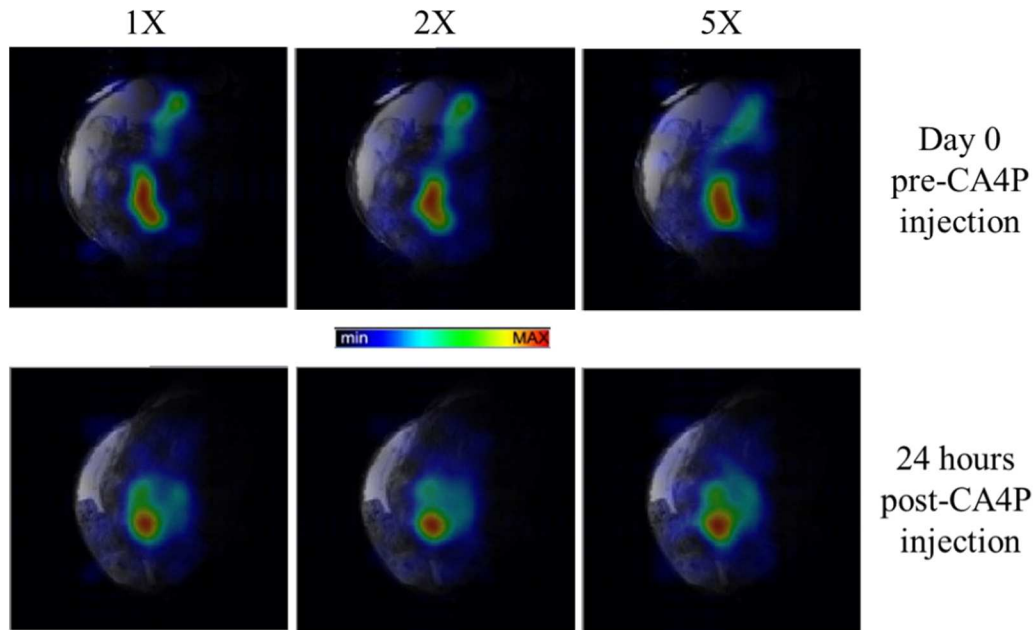
Figure 3.11 Lactate distribution as mapped by MRSI in a H1975 tumor (CA4P M1, Table 3.1) in response to CA4P treatment. Top panel: lactate maps before CA4P injection, lower panel: lactate distribution in the same tumor cross-section 24 hours post CA4P injection. 1X pre/post = 295/206 a.u. and 5X pre/post = 311/201 a.u., mean integrated intensity (scale bar 0 – 4 a.u.).
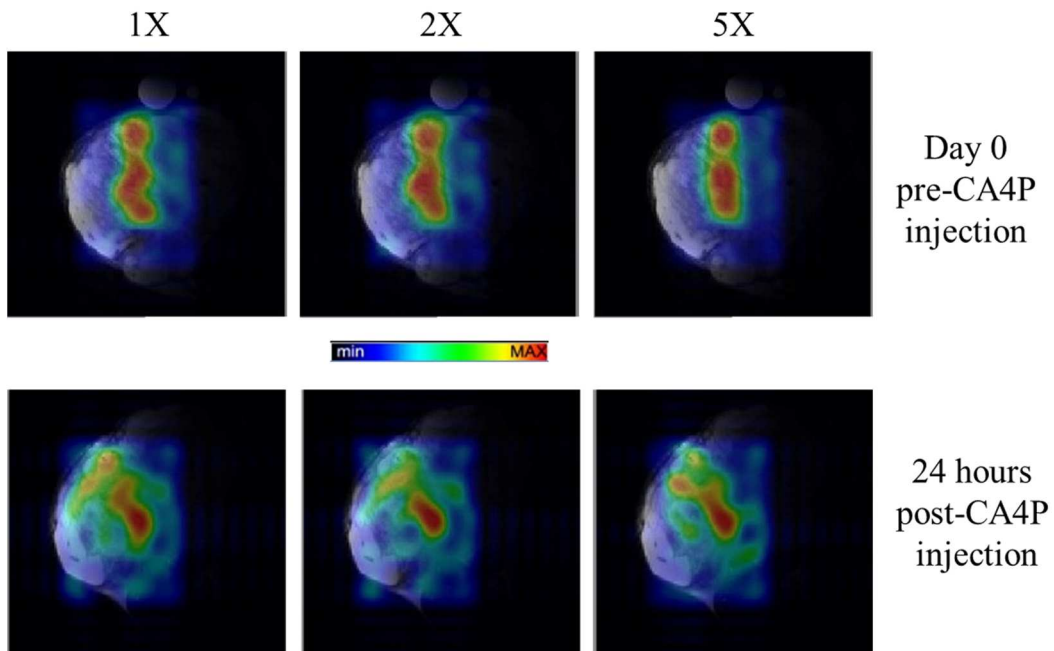
Figure 3.12 Lactate distribution in a second H1975 tumor (CA4P M3, Table 3.1) pre and post injection of CA4P. 1X pre/post = 473/446 a.u. and 5X pre/post = 466/427 a.u., mean integrated intensity.
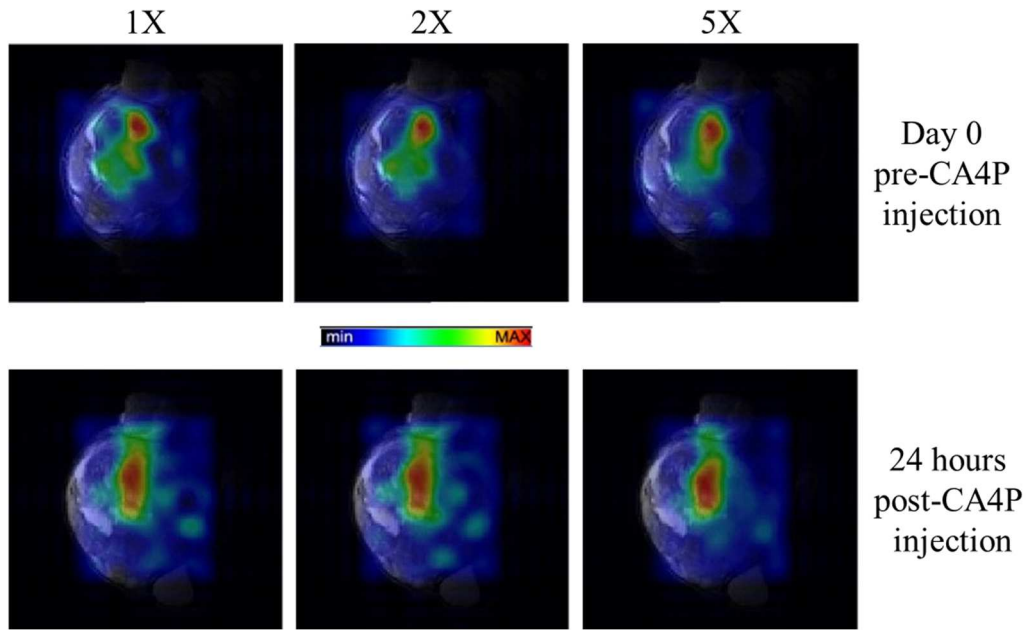
Figure 3.13 Lactate distribution in a third H1975 tumor (CA4P M5, Table 3.1) pre and post injection of CA4P. 1X pre/post = 428/476 a.u. and 5X pre/post = 413/465 a.u., mean integrated intensity.
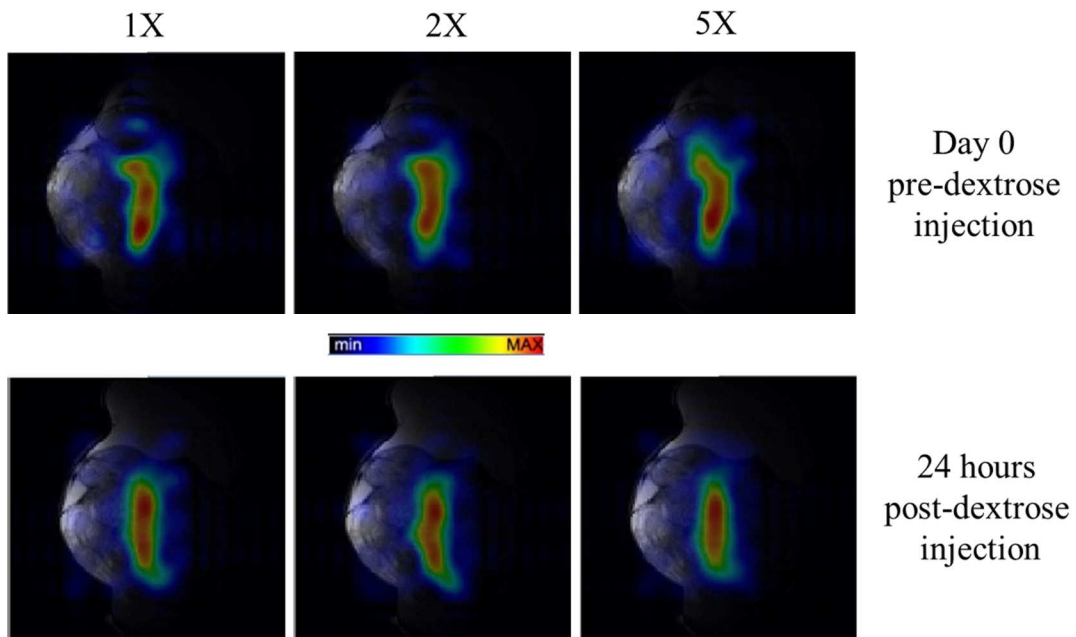
Figure 3.14 Lactate distribution as mapped by MRSI in a H1975 tumor in response to injection of dextrose. Top panel: lactate maps before dextrose injection. Lower panel: lactate maps 24 hours post dextrose injection. 1X pre/post = 278/263 a.u. and 5X pre/post =269265 a.u. mean integrated intensity.

Table 3.1 Lactate integrated intensities (arbitrary units) and ratios for the CA4P and control cohorts (Ratio = Pre/Post).

Cohort		1X			5X		
		Pre	Post	Ratio	Pre	Post	Ratio
CA4P	M1	295	206	0.7	311	201	0.65
	M2	507	461	0.9	529	448	0.85
	M3	473	446	0.94	466	427	0.92
	M4	513	450	0.88	504	462	0.92
	M5	428	476	1.11	413	465	1.13
Control	M1	475	481	1.01	454	469	1.03
	M2	278	263	0.95	293	261	0.89
	M3	239	218	0.91	225	221	0.98
	M4	379	386	1.02	390	394	1.01
	M5	327	339	1.04	311	322	1.04
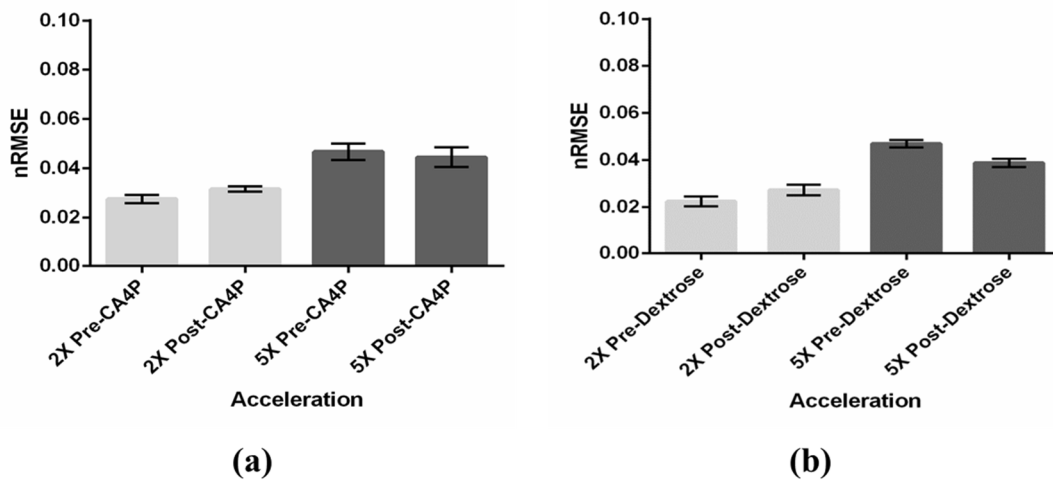
Figure 3.15 The normalized RMSEs corresponding to accelerations 2X and 5X, both pre and post injection of the probe, for the (a) CA4P and (b) control cohorts.

The low standard deviation values also indicate very less variation in the nRMSE across a particular cohort as seen in Figure 3.15 and the trend seen is as expected. Additional statistical analysis was performed on the datasets from both the CA4P and control cohort, as depicted in Figure 3.16. In the first instance, only four mice from the CA4P cohort that showed a decrease in the total lactate integrated intensity post 24 hours injection were included in the analysis, excluding the mouse (Figure 3.13) that showed the opposite trend. As seen from Figure 3.16 (a), a statistically significant ($p < 0.05$) difference is seen in the lactate levels pre and 24 hours post CA4P injection, in both the 1X and 5X reconstructions.

On the other hand, no statistical significance is seen ($p > 0.05$) between the 1X and 5X reconstructions, both pre and post injection, indicating high fidelity between the reference and accelerated datasets. When all five mice were included in the analysis, no statistical significance ($p > 0.05$) in the paired t-test was observed between the measured tumor lactate levels, pre and 24 hours post administration of CA4P as illustrated in Figure 3.16 (b). However, the reconstruction accuracy between the 1X and 5X was still preserved with $p > 0.05$.

All five mice were included for analysis in the control cohort. As seen in Figure 3.16 (c), no statistically significant differences ($p > 0.05$) were found in the tumor lactate levels prior to and 24 hours after the injection of dextrose, as expected. Similarly, the 1X and 5X reconstructions were found to be statistically similar ($p > 0.05$), indicating high fidelity and negligible loss of information between the reference and accelerated reconstructions.
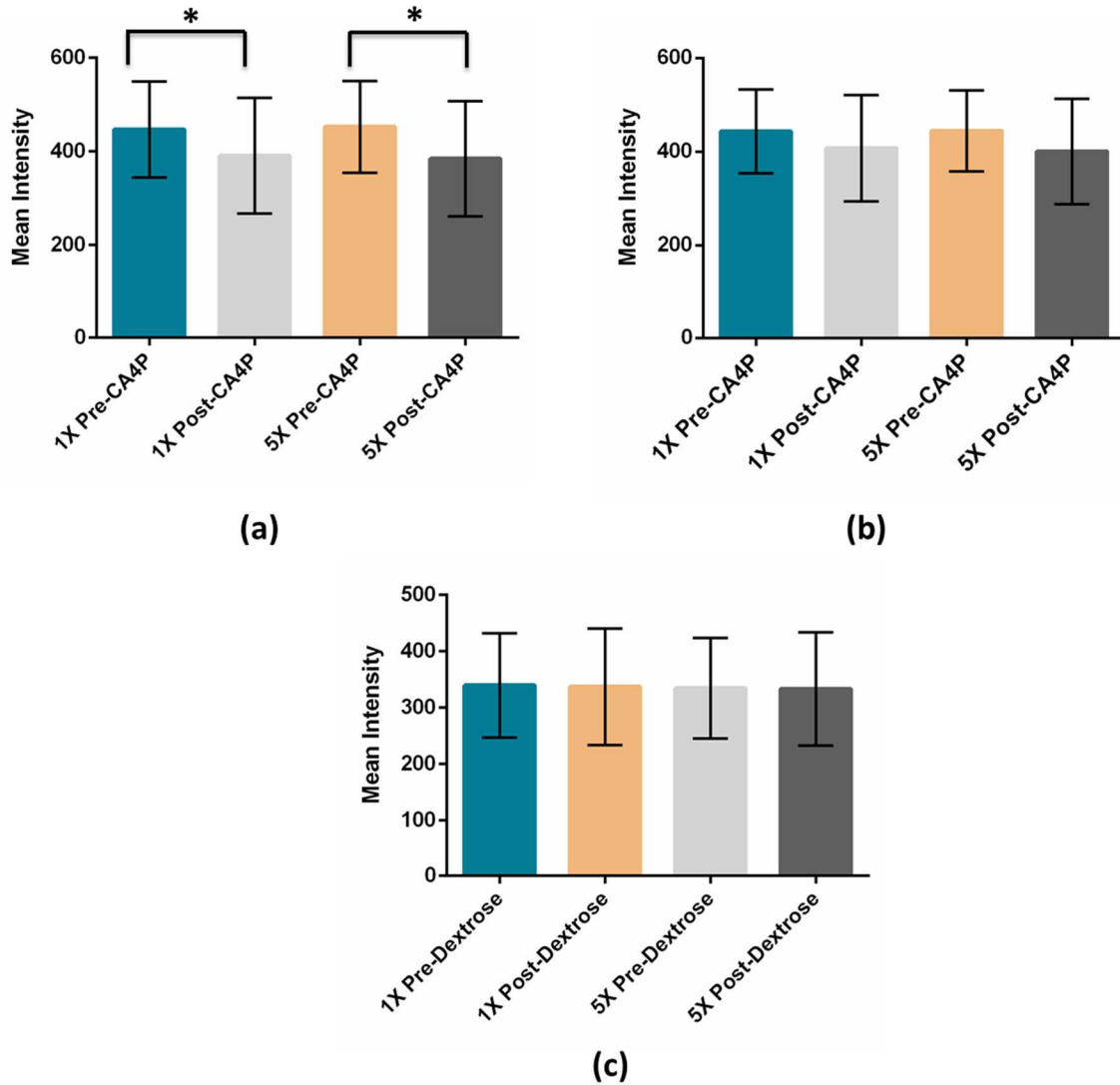
Figure 3.16: Statistical analysis on the CA4P and control cohorts (* indicates $p < 0.05$). (a) The CA4P cohort considering $n = 4$. Statistical significance found in measured lactate levels measured prior to and 24 hours post CA4P injection. (b) The CA4P cohort considering $n = 5$. No statistical significance found between pre and post tumor lactate integrated intensities. (c) The control cohort considering $n = 5$. No statistical significance found in tumor lactate pre and post dextrose injection. $P > 0.05$ between all 1X and 5X datasets.

3.3 Discussion & Conclusions

A CS accelerated lactate-selective MRSI pulse sequence was implemented in the

Bruker 7 T ParaVision 5.1 environment to facilitate fast MRSI acquisitions of lactate in

the preclinical setting. The developed sequence achieved the prospective pseudo-random undersampling of the k-space 'on the fly' to facilitate CS acquisitions and reconstruction. The lactate-selective CS-MRSI sequence achieved high-speed mapping of the lactate peak both *in vitro* and *in vivo* in solid tumors and could potentially save 80% of the acquisition time.

As previously discussed, lactate is a key player in cancer. The increased glucose uptake by cancer cells as compared to normal tissues can be exploited for tumor diagnostics, anti-cancer therapy, and in the detection of metastasis using 2-[^{18}F]Fluoro-2-deoxyglucose positron emission tomography (FDG-PET) [127]. Both hexokinase activity and glucose transporter expression tend to regulate the update of FDG in cells [127, 128]. FDG-PET thus enables a non-invasive visualization of the Warburg effect, which is a fundamental property of neoplasia [128], and has been widely utilized in oncology as a staging/restaging tool and biomarker of cancer progression and prognosis. However, this technique does have its pitfalls and is not able to capture glucose activity in all types of cancers, such as those of the prostate, pancreas, and liver [127]. Other concerns like the presence of a strong background signal, inability of the probe to sufficiently perfuse the tumor, and efflux of FDG from certain types of cancer cells may hinder the imaging process [127].

The ability to directly measure the lactate distribution in solid tumors can prove to be significantly beneficial as this metabolite is a key marker of altered metabolism, possible malignancy, and tumor hypoxia. As previously discussed, tumor metastasis and recurrence have been linked to elevated lactate concentrations, while variations during radiotherapy and treatment can provide insights into the efficacy of a particular

therapeutic strategy. While various MRI sequences are capable of measuring tumor characteristics such as the perfusion, apparent diffusion coefficient (ADC), and pO_2, MRSI is the only technique that can map the spatial heterogeneity of lactate in cancer. The developed ^{1}H lactate-CS-MRSI sequence offers the possibility of employing <u>fast non-invasive lactate imaging as a powerful prognostic marker</u> in the clinic.

Hyperpolarized ^{13}C MRSI is currently the only other competing technique for [1-^{13}C] lactate measurements [129-131]. Hyperpolarization offers a 10,000 – 100,000 fold increase in the signal intensity [132] and is useful for capturing the pathways of endogenous biomolecules [129, 130] upon intravenous injection of the hyperpolarized solution that is generated external to the subject. Various acceleration strategies have been applied to ^{13}C MRSI [15] (including CS, as reviewed in detail in Chapter 2 of the thesis) as the rapid enhancement decay, determined by the T_1 of the agent injected (~30 – 60 s for the agents considered to date [15]), necessitates a rapid acquisition of the data following dissolution. This also places a restriction on the type of compounds that can be hyperpolarized as the rate of signal relaxation must be slow enough to enable *in vivo* administration and subsequent imaging of metabolism. Other regulatory aspects like the integrity of the agent also need to be taken into consideration [15]. The other main challenge is the clinical translation of ^{13}C MRI/MRSI due to the need for additional hardware, specialized equipment for a sterile preparation of the agent, rapid administration of the agent to the patient, and routine quality control checks [133]. Human trials have been few [133] and the above mentioned challenges still need to be addressed for safe routine clinical scans. Under these circumstances, the developed ^{1}H

lactate-CS-MRSI sequence could potentially be beneficial for a regular assessment of lactate changes in the clinic, particularly to assess and personalize therapeutic outcomes.

The later section of this chapter demonstrated the application of the lactate-CS-MRSI sequence in evaluating changes in lactate levels in response to therapy using CA4P. The sequence was used to monitor baseline lactate levels and subsequent changes 24 hours post the injection of the prodrug. The CS reconstructions maintained high fidelity with the 1X reference even at 80% undersampling. Four of the five tumor mice in the cohort showed a decrease in the total integrated intensity of lactate within the tumor volume when measured 24 hours after CA4P injection, while one mouse from the cohort showed a tumor lactate increase 24 hours post CA4P administration. <u>This study demonstrated, for the first time, a reduction in lactate levels of H1975 tumors 24 hours following a vascular targeting agent, CA4P.</u> To the best of my knowledge, ^{1}H MRSI measurement of lactate changes upon CA4P administration has not been documented in the literature to date.

The initial hypothesis for this study was that an increase in tumor lactate levels would be observed upon treatment using CA4P. This is based on the fact that CA4P-induced vascular shutdown would lead to more hypoxia or acidosis, causing higher glycolysis rates to produce more lactate. A poorly perfused tumor vasculature may also not be able to clear the accumulated lactate efficiently. However, previous studies have demonstrated an improvement in the tumor pO_2 and vascular perfusion 24 hours post CA4P administration, suggesting that there is recovery in the vasculature particularly in the rim of the tumor [118, 121, 125]. This would potentially result in improved blood flow and lead to either an increase in lactate clearance or decreased production of lactate,

or possibly both. This might explain why a decrease in tumor lactate levels was measured 24 hours post injection of CA4P. Previous studies have also observed that there is heterogeneity in the restoration of perfusion within the tumor, with lower lactate levels detected in the better perfused regions [125]. The study by Bohndiek *et al* demonstrated a 34% decrease in the rate constant corresponding to ^{13}C hyperpolarized labeled flux between [1-^{13}C] pyruvate and lactate [125] 6 hours after CA4P injection, and continued to be at that lower level even after 24 hours. However, no significant change in lactate concentrations in tumor extracts was detected 24 hours later in this study [125]. Other VDAs like ZD6126 have also been employed to probe tumor dynamics [134] using a MQC spectral editing sequence wherein no significant change in lactate was found in response to the prodrug. Another aspect to take into consideration would be the type of tumor being investigated as response to targeting agents and therapeutics may be varied among different types of solid tumors.

In conclusion, fast lactate MRSI was implemented in the preclinical setting with a reduction in the acquisition time by up to 80% *in vivo*. This study also offered a first insight into H1975 tumor lactate dynamics in response to treatment using CA4P, wherein a decrease in tumor lactate levels was measured 24 hours after administration of the prodrug. Future studies could further investigate the CA4P-induced dynamics of tumor lactate metabolism in different types of cancers *in vivo* using MRSI.

(**Note:** Certain sections of Chapter 3 are based on the paper – "Compressed Sensing Accelerated MR Spectroscopic Imaging of Lactate", R. Vidya Shankar, S. Agarwal, and V. D. Kodibagkar, in preparation for submission to *Magnetic Resonance in Medicine* for review.)

CHAPTER 4

2D CS-MRSI OF THE PEDIATRIC BRAIN

The advantages offered by MRSI in the non-invasive, quantitative mapping of important biomarkers have been documented in Chapters 1, 2, and 3 of this dissertation. The objective of this study was to retrospectively evaluate the feasibility of scan time reduction using compressed sensing (CS) based MRSI in pediatric patients undergoing routine brain exams.

4.1 Background

Various MRI sequences are routinely employed in pediatric neuroimaging studies for longitudinal investigations of brain development and function in children. Spectroscopic imaging techniques like single voxel spectroscopy (SVS) and MRSI/CSI can be employed to assess the concentrations of various metabolites in the pediatric brain. For e.g. rapid neurochemical changes in brain structure and content have been observed at various stages of brain development [135, 136], with an increase in NAA, creatine, and glutamate accompanied with a decrease in the concentrations of choline and myo-inositol (mI) [137]. Vital biochemical information can be extracted in numerous pathological conditions and diseases such as in neuro oncology and brain tumors [138-143], neurofibromatosis [144], tuberous sclerosis [145], epilepsy and other related seizures [146], neurodegenerative, neuropsychiatric, and mitochondrial disorders [135, 137, 143], and in the evaluation of hypoxia/ischemia and stroke in the pediatric brain [147].

The basic principles of SVS and MRSI along with their respective merits/demerits have previously been discussed in Chapters 1 and 2 and will not be

elaborated here. The long scan times encountered in MRSI are not desirable when imaging pediatric patients as children are more likely to move or not cooperate during the examination window. This could also have added implications like increasing the sedation time for patients under anesthesia, such as in infants and in the elderly. Thus, it is crucial to devise and implement fast imaging techniques for the benefit of the pediatric patient population.

However, very few studies have sought to investigate and validate the feasibility of fast imaging techniques in pediatric patients in both MRI and MRSI [148-153]. The fast MRSI study by Kim *et al* using dual band RF pulses and a spiral k-space readout focused on the rapid extraction of metabolic profiles from the corticospinal tract in the pediatric brain [148], while the study in children by Vasanawala *et al* investigated the application of fast CS-MRI combined with parallel imaging in various anatomies like the abdomen, cardiac, and knee [149]. The clinical performance of rapid acquisition using compressed sensing (CS) and parallel imaging in contrast enhanced abdominal pediatric MRI has been assessed by Zhang *et al* and Cheng *et al* [152, 153]. A fast pediatric cardiac study by Hsiao *et al* focused on the application of parallel imaging and CS for the evaluation of ventricular volume and blood flow in volumetric phase contrast MRI [150]. In all the above mentioned studies, a significant reduction in the acquisition time was achieved with preservation of anatomic detail, and spatial and spectroscopic image quality.

The objective of this study was to test the application of CS accelerated MRSI in pediatric patients undergoing routine MRI scans for various brain-related concerns. The theory and principles underlying CS have been discussed in previous chapters and will

not be elaborated here. The retrospective application of CS-MRSI is evaluated in both healthy brain tissue and in a few tumor cases for accelerations up to five-fold, with a quantitative evaluation of the accuracy and fidelity of the reconstructed spectra in comparison with the fully-sampled 1X reference MRSI datasets.

4.2 Materials and Methods

This study was approved by the local institutional review board and was compliant with the Health Insurance Portability and Accountability Act (HIPAA). Informed consent was obtained for acquiring the MRSI data, wherein a stock spectroscopic imaging pulse sequence provided by the MRI manufacturer was employed. The retrospective evaluation of 2D ^{1}H CS accelerated MRSI was performed on 20 pediatric brain cases, which included 11 male and 9 female patients in the age range 3 days to 16 years. Tables B.1 and B.2 (Appendix B) summarize the demographic details and various MRI/MRSI parameters related to the patient group under consideration.

4.2.1 MRSI Data Acquisition and Undersampling

All MRSI data was acquired on a Philips 3 T Ingenia MRI scanner using a standard point resolved spectroscopy (PRESS) based MRSI pulse sequence. A 13-channel head coil array was employed for all experiments. Initial studies involved testing the CS-MRSI reconstruction algorithm on phantom (metabolite solution -12 mM NAA, 10 mM creatine, 3 mM choline) and volunteer MRSI datasets. In the patient studies, general anesthesia was administered to the patients for their routine brain MRI exam. Fully sampled MRSI data was collected on patients in the age range 3 days - 16 years

with the following acquisition parameters: TE/TR = 46/1500 ms, 16x16x2048 grid, 10 mm slice thickness, 1 average, total acquisition time for the fully sampled 1X reference dataset = 9 min. The variable density sampling mask for different acceleration factors, illustrated in Figure 4.1, was generated as previously described in [70, 71]. The k-space was pseudo-randomly undersampled along the phase encode directions to generate datasets that represented 2X (50%), 3X (33%), 4X (25%), and 5X (20%) acceleration.

4.2.2 CS-MRSI Reconstruction

A custom non-linear iterative reconstruction based on the conjugate gradient algorithm was implemented in Matlab (Mathworks Inc., MA) to reconstruct all the retrospectively undersampled MRSI datasets. The CS-MRSI reconstruction was formulated as a convex optimization problem, which involved minimizing the cost function [71], previously detailed in Chapter 3.

4.2.3 Post Processing and Error Metric

All reconstructed CS-MRSI datasets were subjected to a quantitative comparison with the fully sampled 1X reference dataset using the metrics discussed in Chapter 3. In each case, the root mean square error (RMSE) metric was used to compute the reconstruction error for each individual metabolite (NAA, creatine, choline, and lactate), as previously employed in Chapter 3. The RMSE can be interpreted as being equivalent to the normalized RMSE (nRMSE) since the range of each dataset was normalized to vary from 0 to 1. Standard post-processing steps were applied to all the reconstructed MRSI datasets using the jMRUI [111] software package. Detailed analysis was

performed on the voxels located in the region interior to the brain for all the twenty MRSI datasets under consideration. A total of 957 voxels were analyzed across all the pediatric brain MRSI datasets.

4.2.4 Statistical Analysis

A voxel-wise 2-tailed paired t-test was performed on the metabolite intensity and ratio maps (NAA/Cr, NAA/Cho, and Cho/Cr) from each reconstructed dataset with the corresponding 1X reference dataset using the GraphPad Prism (San Diego, CA, USA) scientific software. A p-value < 0.05 was considered to be statistically significant and indicative of an inaccurate reconstruction. Voxels with a denominator value of zero (lack of deterministic fit) in the 1X or accelerated reconstructions were set to zero for the ratio calculations. In addition, the fidelity of the reconstructions was assessed by determining the magnitude of correlation between the 1X fully sampled reference and the accelerated reconstructions using the Origin® 8.1 software package. Correlation graphs were generated for individual mean metabolite intensities collated from all twenty datasets and evaluated against the 1X fully sampled reference as a function of acceleration. The accelerated reconstructions were considered quantitatively equivalent to the 1X reference if the magnitude of coherence was close to one, using a 95% confidence interval.

4.3   Results

The retrospective evaluation of CS-MRSI was initially conducted on phantom and human volunteer MRSI datasets from the 3 T Philips Ingenia MRI scanner. Variable density undersampling masks for acceleration factors 2X − 5X that were simulated in

Matlab^{TM} are depicted in Figure 4.1. Figures 4.2 and 4.3 depict the results from the phantom experiments, wherein mean metabolite intensities are accurately reconstructed up to five-fold acceleration, with high spectral fidelity and negligible information loss. Figure 4.3 shows the nRMSEs for each individual metabolite and for the full spectrum. The normalized metabolite RMSEs remain below 3% up to 5X for each individual metabolite, while the nRMSE for the entire spectrum is slightly above 1% at five-fold acceleration.
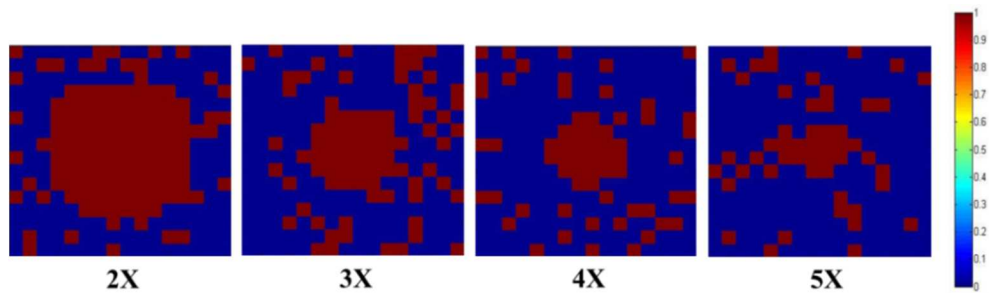
Figure 4.1 Variable density under-sampling masks simulated in MatlabTM for various acceleration factors – 16x 16 matrix (total 256 samples 1X).
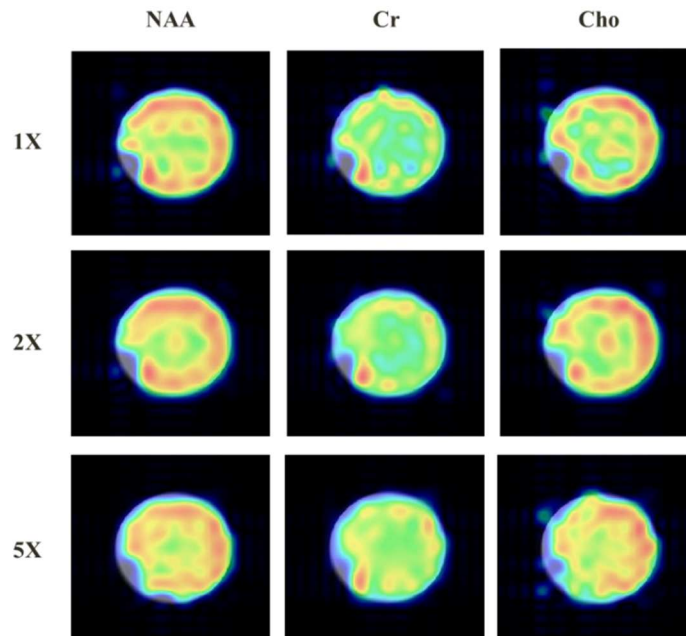
Figure 4.2 Metabolite maps of NAA (12 mM), creatine (10 mM), and choline (3mM) at acceleration factors 1X, 2X, and 5X (16x16x2048 grid, TR/TE = 2000/46 ms, 20 mm slice thickness, 1 average).
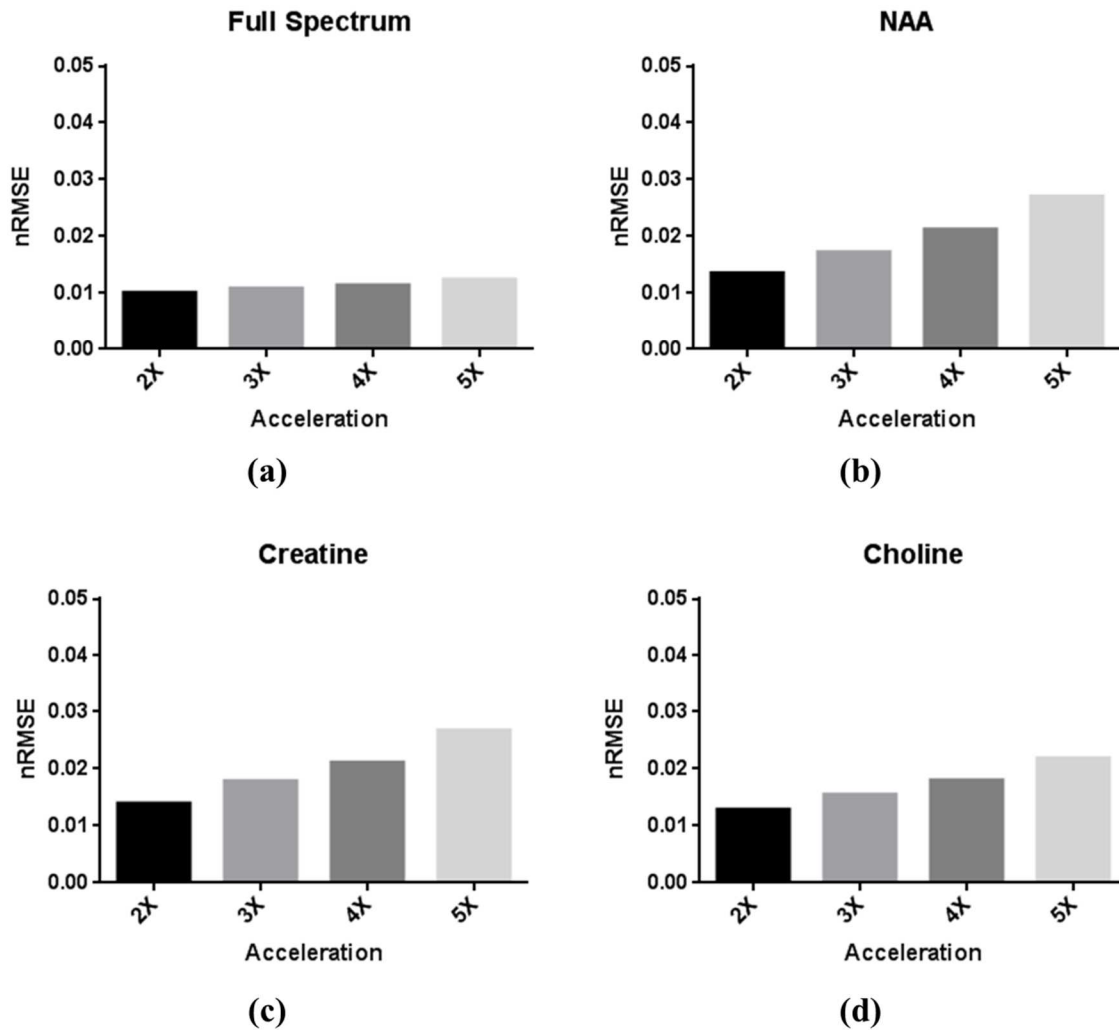
Figure 4.3 The nRMSEs for the phantom dataset at acceleration factors 2X – 5X. (a) the full spectrum, (b) NAA, (c) Creatine, and (d) Choline.

A retrospective evaluation of CS-MRSI was also conducted in 3 normal human volunteers, with results depicted in Figures 4.4 and 4.5. This study was approved by the local institutional review board and informed consent was obtained for acquiring the MRSI data. Figure 4.4 depicts select voxels from a volunteer brain MRSI dataset, with spectral fidelity maintained up to 5X.
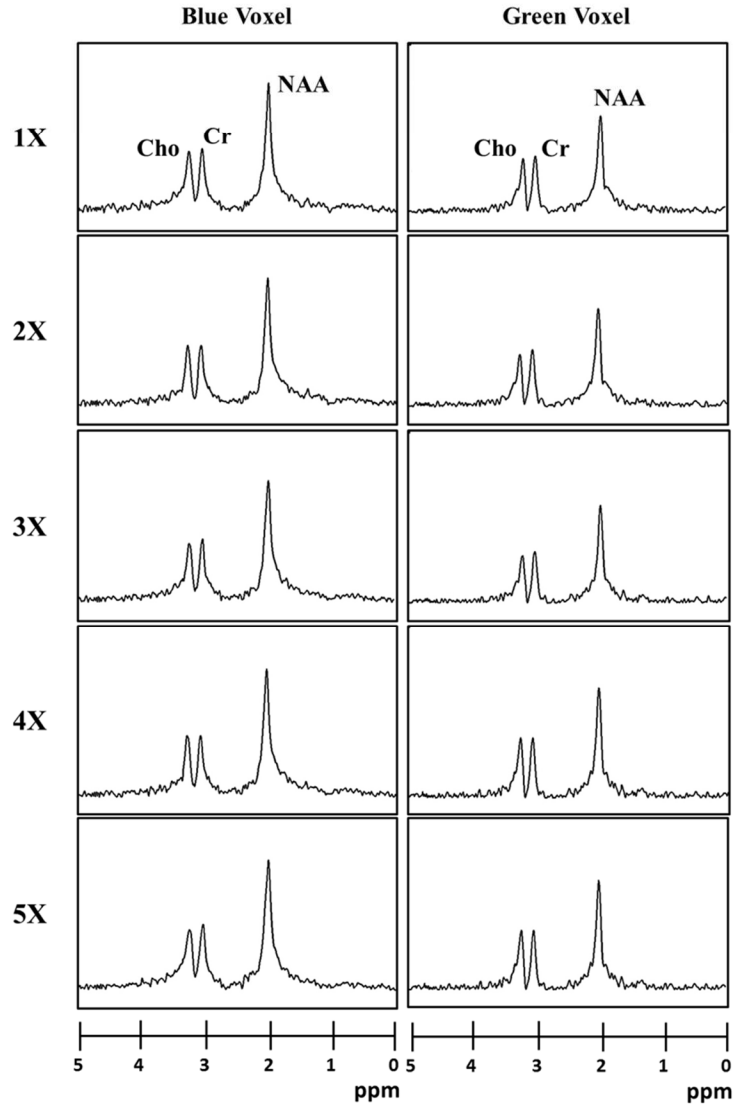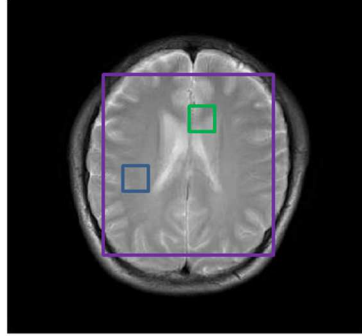
Figure 4.4 Spectra from select voxels of a volunteer MRSI dataset**.** MRSI scan parameters: 16x16x2048 matrix, TR/TE = 1500/46 ms, 1 average, 1 cm slice thickness, FOV 24 x 24 cm2, total scan time for the 1X = 9 min. The y-axis limits are from -0.1 to 1 for all illustrated spectra.
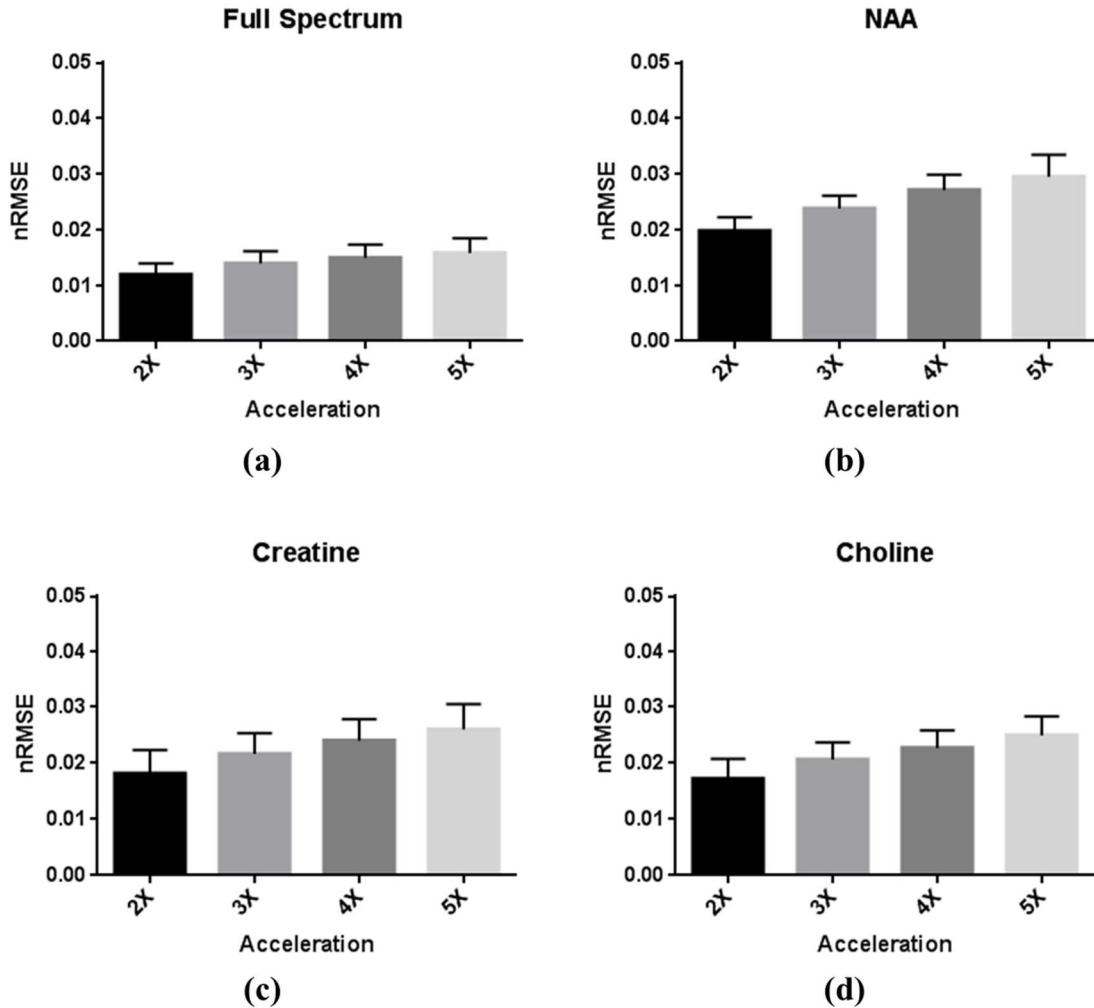
Figure 4.5 Mean nRMSEs ± standard deviations for the 3 volunteer MRSI datasets for (a) the full spectrum, (b) NAA, (c) creatine, and (d) choline.

Figure 4.5 shows the mean normalized RMSEs for the 3 volunteers at 2X-5X accelerations. The nRMSE at 5X for the full spectrum is (1.6 ± 0.26) %, while that for the individual metabolites is (2.96 ± 0.39) % for NAA, (2.6 ± 0.45) % for creatine, and (2.49 ± 0.34) % for choline. The reconstruction error remains below 3.5% up to 5X when considering individual metabolites, with a low and consistent standard deviation across the 3 volunteers for accelerations 2X – 5X. Mean metabolite ratios NAA/Cr, Cho/NAA, and Cho/Cr ± standard deviations have been collated in Table 4.1 for the three volunteers.

Table 4.1 Mean metabolite ratios ± standard deviations for the 3 volunteer MRSI datasets for 1X – 5X acceleration factors. (NAA: N-acetylaspartate, Cr: creatine, Cho: choline, M: male, F: female, SD: standard deviation)

Volunteer		NAA/Cr (mean ± SD)	Cho/NAA (mean ± SD)	Cho/Cr (mean ± SD)
1 (M)	1X	2.58 ± 1.04	0.43 ± 0.14	0.98 ± 0.17
	2X	2.61 ± 1.11	0.43 ± 0. 16	0.98 ± 0.16
	3X	2.62 ± 1.07	0.43 ± 0.14	0.99 ± 0.15
	4X	2.73 ± 1.08	0.47 ± 0.15	0.99 ± 0.15
	5X	2.79 ± 1.07	0.49 ± 0.14	1.1 ± 0.15
2 (M)	1X	2.46 ± 1.1	0.46 ± 0.16	1 ± 0.22
	2X	2.49 ± 1.16	0.46 ± 0.17	1 ± 0.23
	3X	2.44 ± 1.15	0.47 ± 0.16	1 ± 0.19
	4X	2.5 ± 1.23	0.47 ± 0.17	1.03 ± 0.2
	5X	2.52 ± 1.26	0.48 ± 0.16	1.2 ± 0.19
3 (F)	1X	2.44 ± 0.77	0.39 ± 0.09	0.91 ± 0.16
	2X	2.44 ± 0.84	0.4 ± 0.1	0.99 ± 0.14
	3X	2.5 ± 0.79	0.45 ± 0.09	1.02 ± 0.16
	4X	2.4 ± 0.69	0.48 ± 1.05	1.15 ± 0.14
	5X	2.31 ± 0.69	058 ± 0.09	1.17 ± 0.15

The retrospective evaluation of CS-MRSI was subsequently performed on pediatric MRSI datasets. Demographics of the pediatric patients scanned, the reason for MRI, and metabolite ratios from MRSI have been collated in Tables B.1 and B.2

(Appendix B). The patient population consisted of 11 male and 9 female patients that included healthy, tumor (also post-surgery) and non-tumor cases, and a few with brain development concerns. The corresponding metabolite ratios from MRSI for all accelerations 1X – 5X have also been documented, with expected variations seen in normal and tumor voxels. Table B.1 lists all parameters from the non-tumor cases, while Table B.2 has parameters corresponding to the patients with brain tumors.

Figures 4.6 and 4.7 depict the MRSI reconstruction results for various acceleration factors from a nine year old female patient scanned for seizures (case 6 in Table B.1). Figure 4.6 shows the PRESS volume of interest (VOI) selected for MRSI overlaid on the T_1 anatomical scout from MRI, with the corresponding spectroscopic imaging grids for acceleration factors 2X - 5X. The CS-MRSI reconstructions displayed spatial distributions that were very similar to that of the 1X reference dataset, with no spurious signals outside the selected VOI. An expanded view of the 1X and 5X spectroscopic grids is depicted in Figure 4.7.

Within the VOI, select voxels were examined to assess the reconstruction quality of individual spectra. Figure 4.8 highlights the spectra from two voxels (blue and green) in the VOI and one (red) located exterior to but close to the periphery of the brain. The CS reconstructions preserve the line shape of the each individual metabolite, with good agreement observed in the peak amplitudes for various accelerations up to 5X. Gradual smoothing of the spectra can be seen with increasing acceleration, which can be attributed to the denoising effects of the wavelet and total variation terms in the CS reconstruction. The difference spectra computed at each acceleration factor also indicate a high fidelity in the CS reconstructions with respect to the 1X fully sampled reference.

The corresponding metabolite maps (obtained after spectral fitting of the peak amplitudes in jMRUI) of NAA, creatine, and choline have been illustrated in Figure 4.9 for the 1X-5X MRSI datasets. Similar spatial distributions can be observed with increasing acceleration for each metabolite.
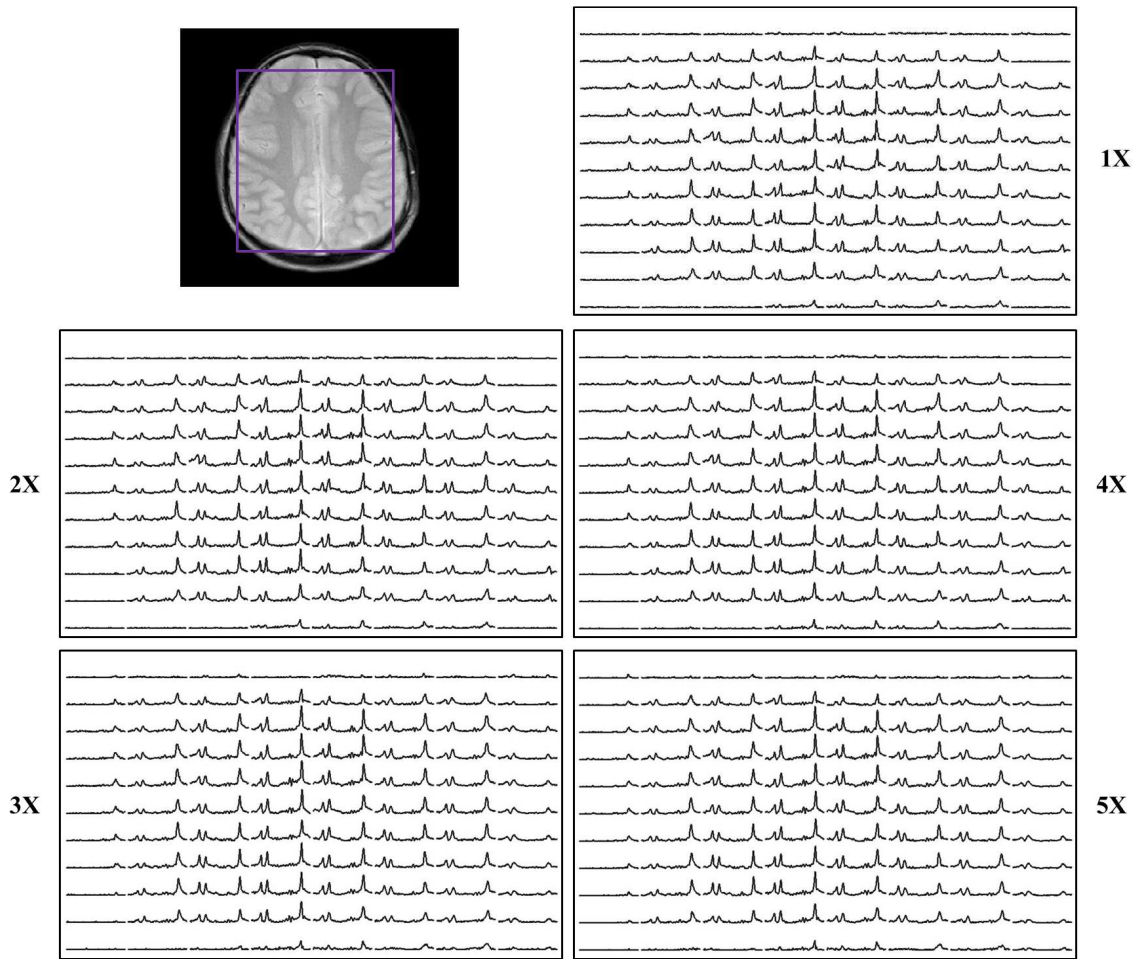
Figure 4.6 MRSI data from a nine year old female patient scanned for seizures and diagnosed with a 2x2 cm2 arachnoid cyst in the anterior right temporal lobe. The figure depicts the anatomical scout MRI with the PRESS VOI, along with the spectroscopic imaging grids corresponding to the VOI for acceleration factors 2X – 5X.

Figure 4.10 displays the metabolite maps of NAA, creatine, choline, and lactate for a pediatric patient diagnosed with a brain tumor. Figure 4.10 depicts the fully sampled and accelerated metabolite maps for a MRSI dataset collected from a 10 year old

male diagnosed with two intra-axial masses of metastatic Ewing's sarcoma, one each in the right temporal and right parietal lobes (case 1 listed in Table B.2). In this case, the spatial distribution of all metabolic profiles is accurately preserved for acceleration factors up to 5X, including the voxels covering the tumors. Distinct variations can be observed between the metabolite distributions in the normal and cancerous tissue regions, as expected. The presence of lactate, an important marker of anaerobic glycolysis in solid tumors, is readily seen in the lesion. Both the spatial spread and spectral line profile of the lactate peak maintains high fidelity with the 1X for CS reconstructions 2X – 5X.
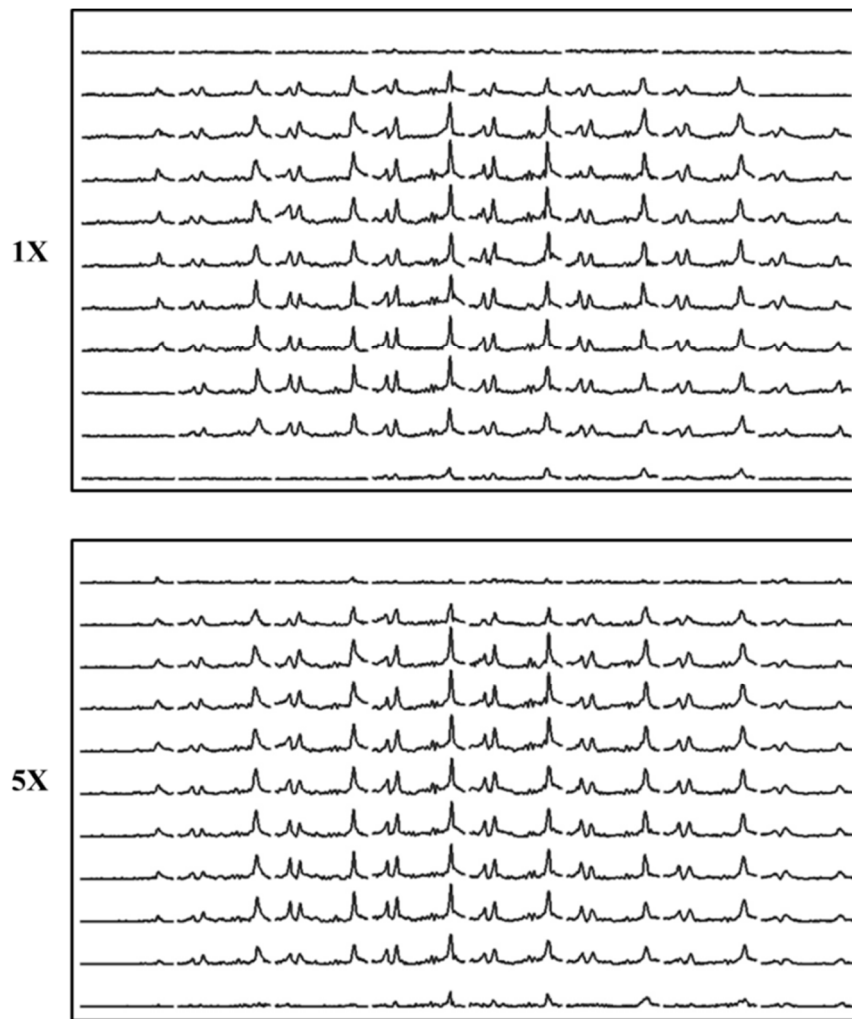
Figure 4.7 An expanded view of the 1X and 5X MRSI grids from Figure 4.6.
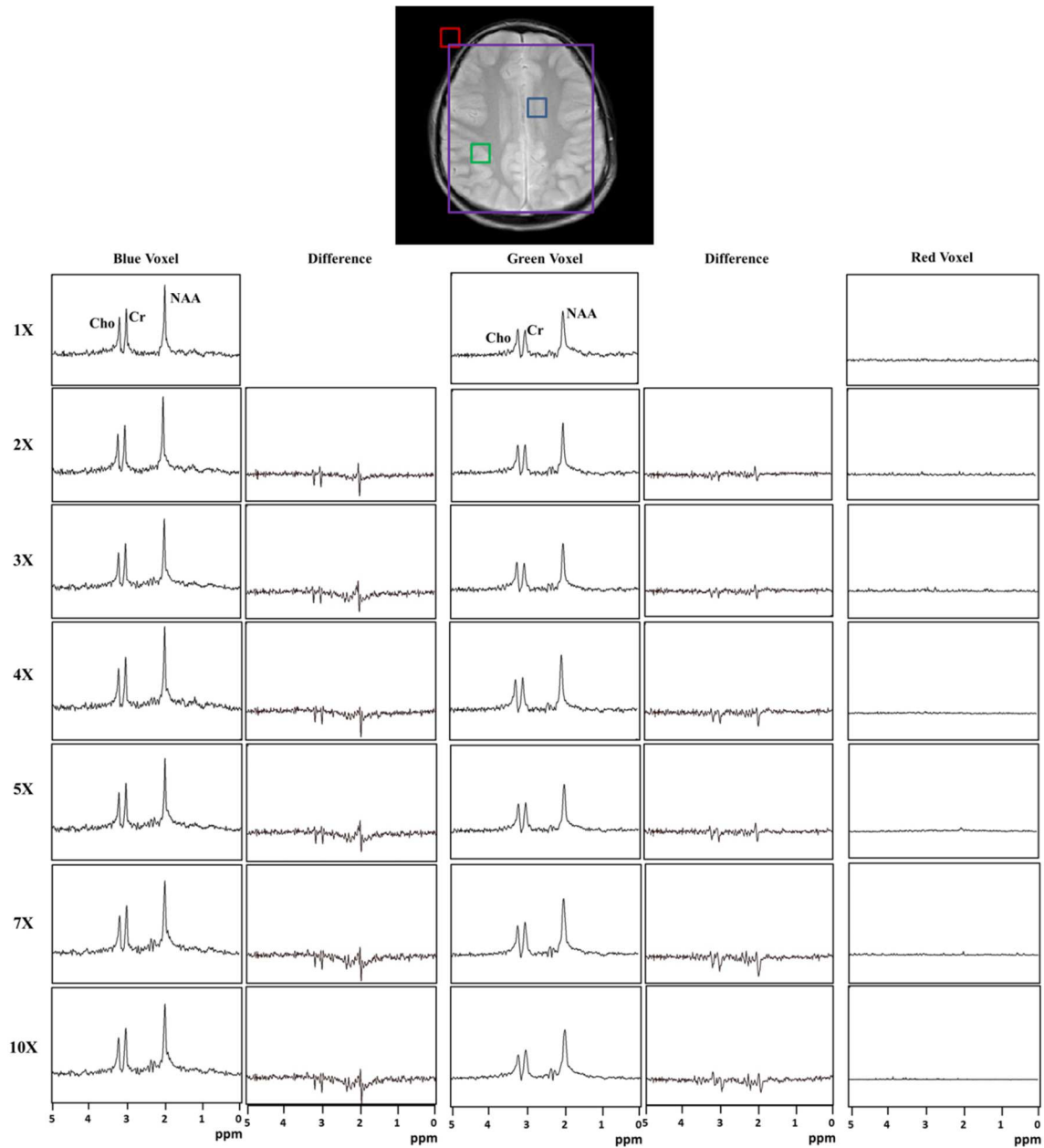
Figure 4.8 Select voxels in blue, green, and red from the representative MRSI dataset in Figure 4.6 for acceleration factors 2X – 5X, 7X, and 10X. The major metabolite peaks NAA, creatine, and choline seen in normal brain voxels are depicted, along with a select voxel located outside but close to the periphery of the brain. The y-axis limits are from - 0.3 to 1 for all illustrated spectra. The CS-MRSI reconstructions display high accuracy even at an acceleration of five.

Figures 4.11 and 4.12 show a few select reconstructed voxels from two tumor

MRSI datasets. The MRSI dataset illustrated in Figure 4.12 is from a 1.5 year old male

patient with a large contrast enhancing lesion in the right posterior lateral basal ganglia/thalamus, as detected by MRI (case 2 from Table B.2). Figure 4.11 shows spectra corresponding to the dataset in Figure 4.10 for the original and CS-accelerated MRSI data. The reconstruction quality was evaluated for one voxel each selected from the normal and tumor regions. The distinct spectral profiles of the metabolites that help distinguish between normal and cancerous tissue have been accurately maintained for the CS-MRSI datasets 2X-5X, as compared to the 1X reference. The same trend is observed in the second brain tumor spectra depicted in Figure 4.12, with faithful CS reconstructions even at higher undersampling factors (up to 5X), and evident differences in the metabolite peak amplitudes in the illustrated normal and tumor tissue voxels.
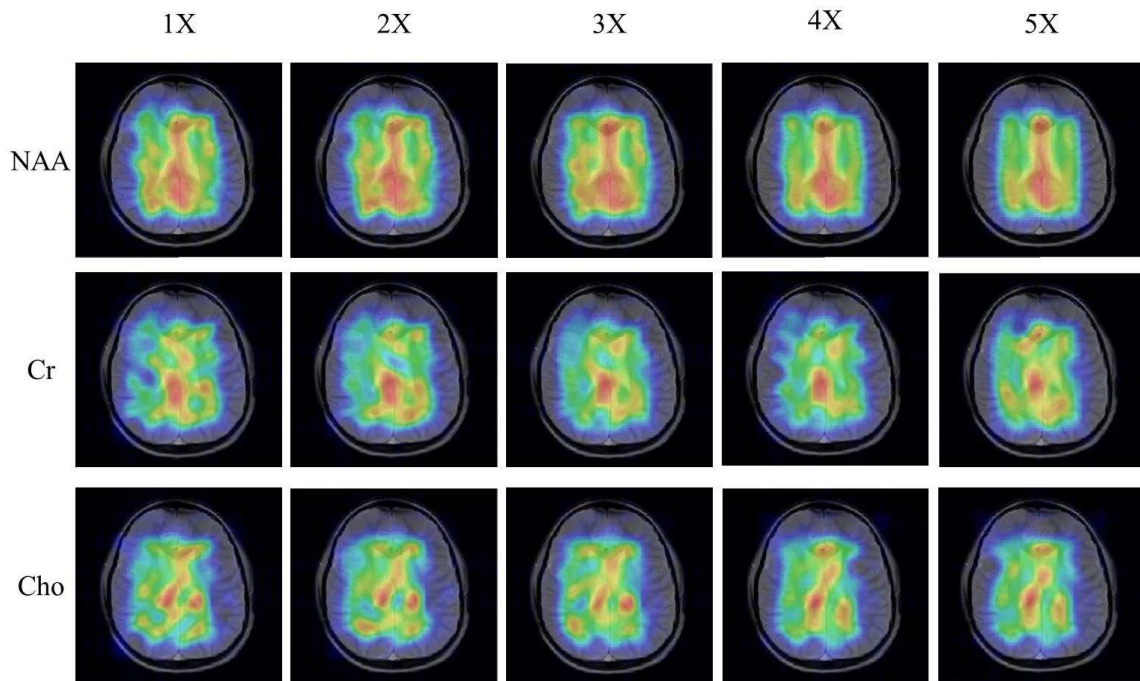
Figure 4.9 Metabolite maps showing the distribution of NAA, creatine, and choline for acceleration factors 1X - 5X in a nine year old female patient scanned for seizures. The mean metabolite ratios for the 1X are given by NAA/Cr = 2.4 ± 1.17, Cho/Cr = 1.0 ± 0.25, and Cho/NAA = 0.47 ± 0.18. The mean metabolite ratios for the 5X are given by NAA/Cr = 2.83 ± 2.26, Cho/Cr = 0.92 ± 0.2, and Cho/NAA = 0.43 ± 0.19.

The RMSE metric was employed to quantify the error in reconstruction (2X - 5X, 7X, 10X) for all 20 pediatric CS-MRSI datasets and is depicted in Figure 4.13. Figures 4.13 (a) - (d) show the individual metabolite RMSEs for NAA, lactate, creatine, and choline respectively. Figure 4.13 (e) shows the RMSE for the entire spectrum. In each dataset, the error increases with increasing acceleration as expected, but does not exceed 3% at 5X for the full spectrum in any of the reconstructed datasets. The RMSEs for the individual metabolites remained below 5% even at an acceleration of 5X, as illustrated in Figure 4.13 (a) – (d).
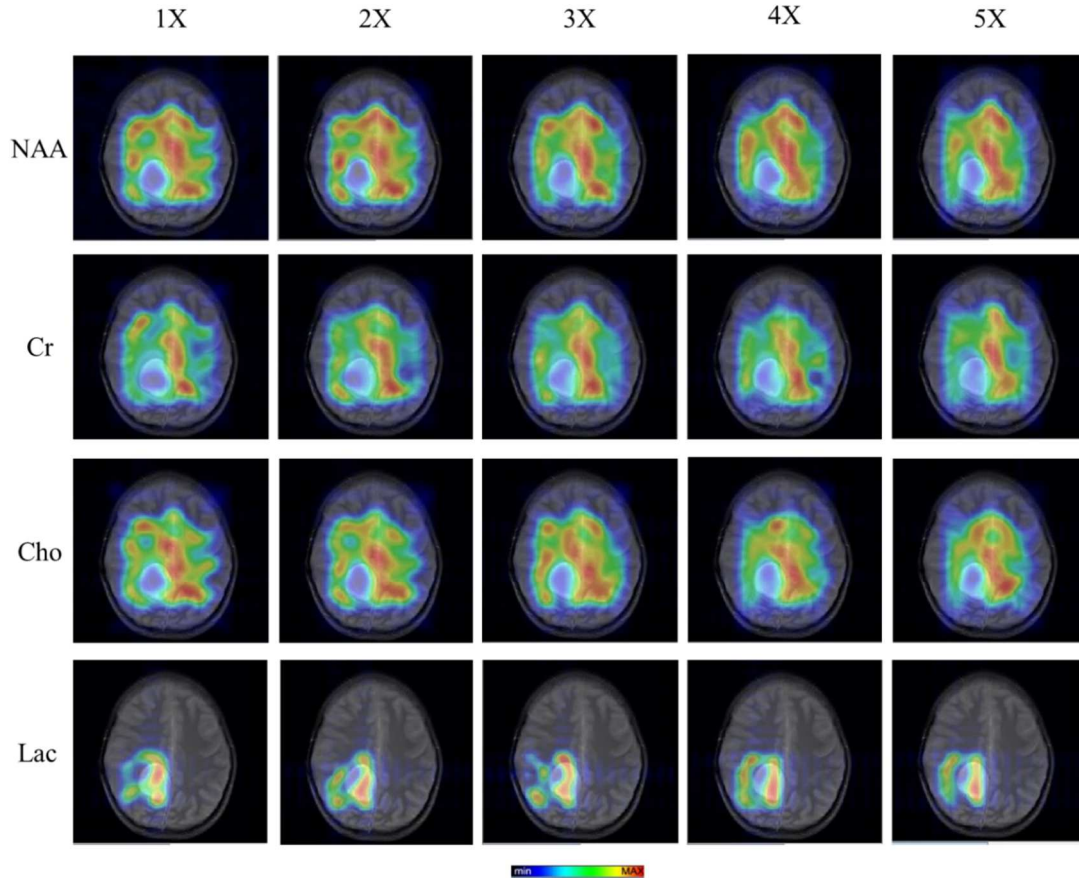
Figure 4.10 Representative metabolite maps of NAA, creatine, choline, and lactate for acceleration factors 1X – 5X. MRSI data was collected from an 11 year old male patient diagnosed with two intra-axial masses of metastatic Ewing's sarcoma, one in the right temporal lobe, and the other in the right parietal lobe. High lactate distribution was found in the tumor region with very low concentrations of the other major brain metabolites.
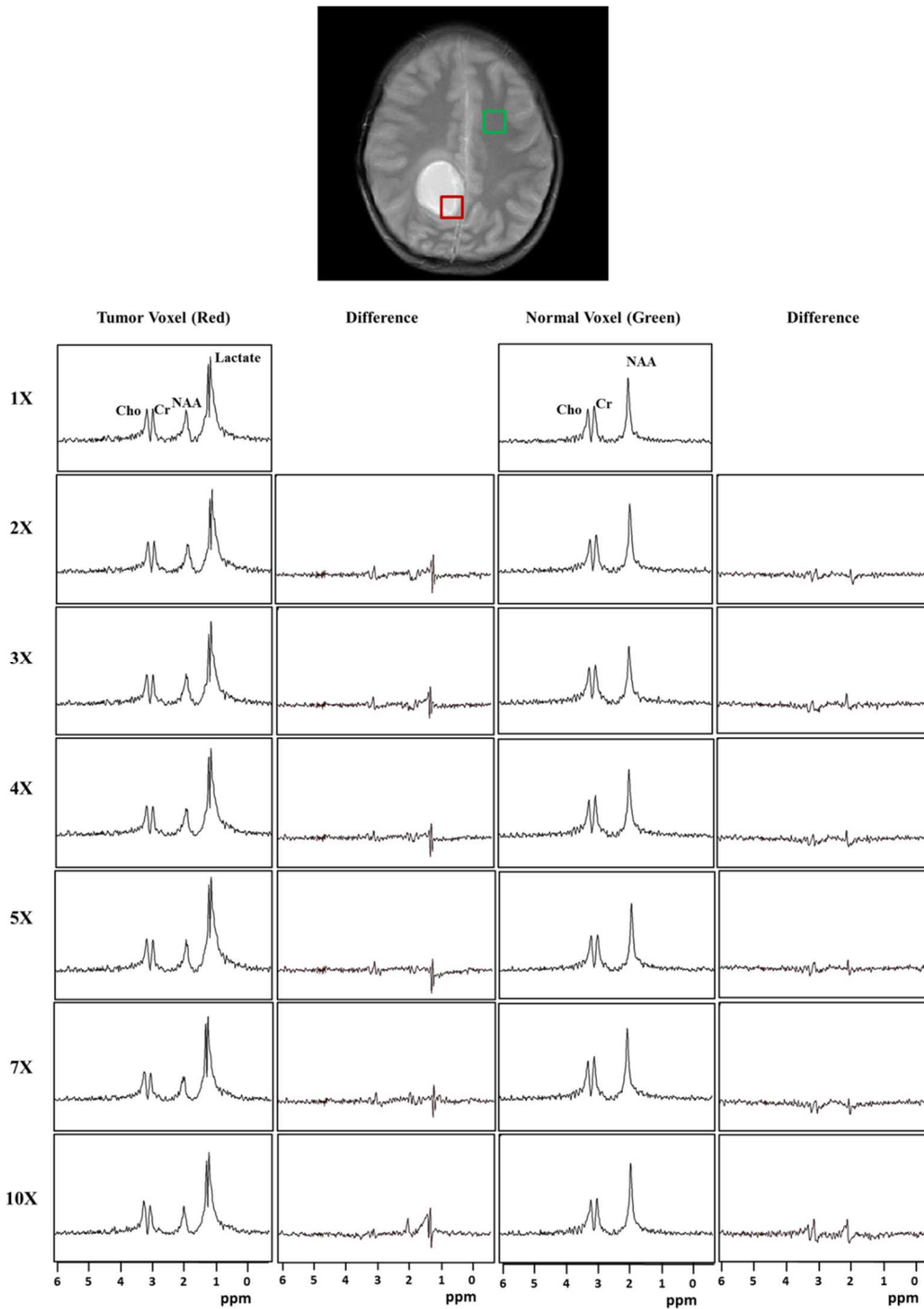
Figure 4.11 Spectra from select voxels of the pediatric brain tumor MRSI dataset previously depicted in Figure 4.10. A huge lactate peak is seen in the tumor voxel indicated in red. The normal and tumor voxels also show variations in the peak amplitudes of choline and NAA. The y-axis limits are from -0.3 to 1 for all illustrated spectra. All accelerations 2X – 5X show good fidelity with the 1X reference.
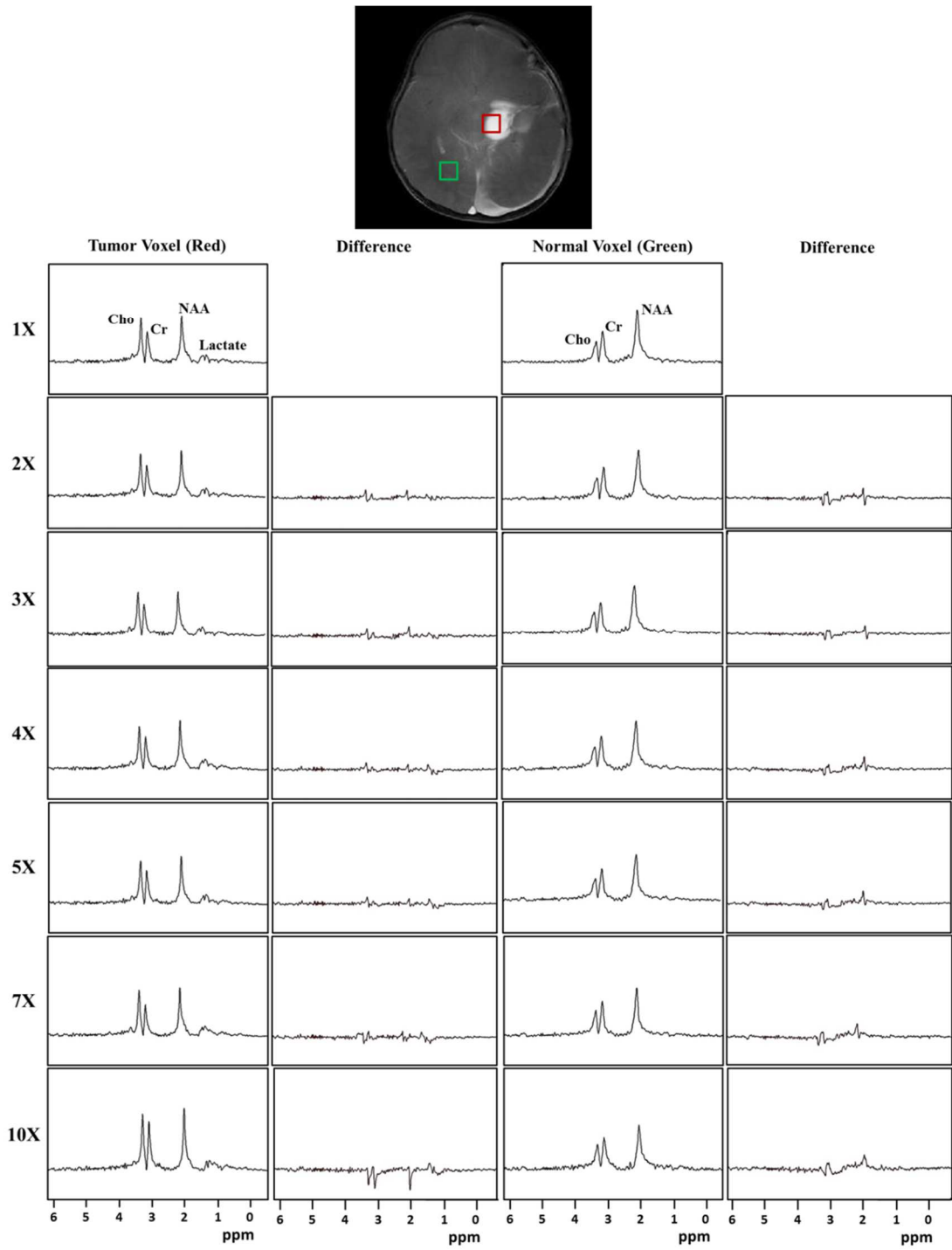
Figure 4.12 Spectra from select voxels of a second pediatric brain tumor MRSI dataset. Lactate is seen in the tumor voxel indicated in red. The normal and tumor voxels also show variations in the peak amplitude of choline, with higher concentration seen in the tumor as expected. The y-axis limits are from -0.3 to 1 for all illustrated spectra. All accelerations 2X – 5X show good fidelity with the 1X reference.
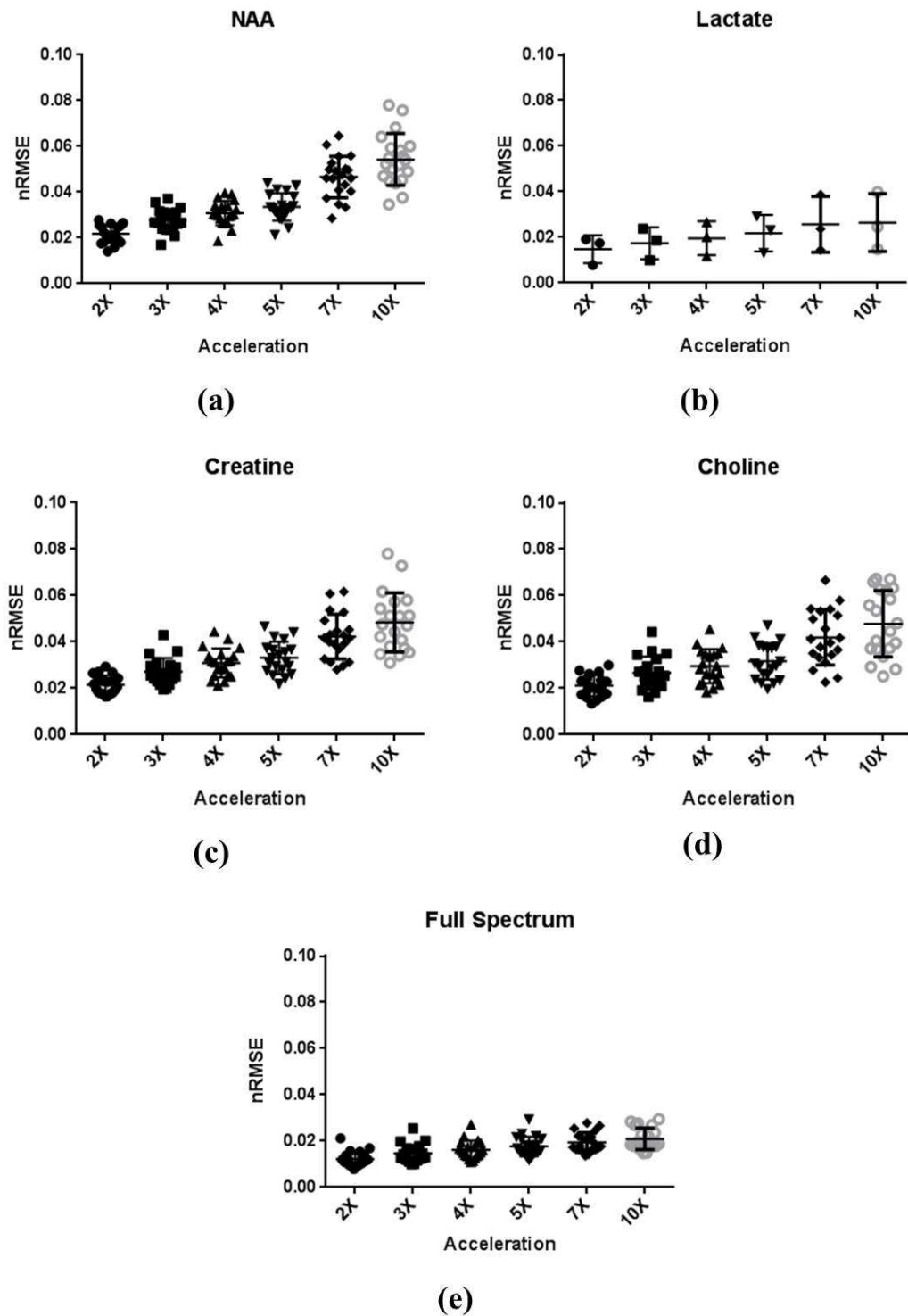
Figure 4.13 Normalized RMSEs of all 20 pediatric MRSI datasets that were evaluated using CS undersampling and reconstruction for up to 90% reduction in the scan time. Individual metabolite RMSEs are depicted in (a)–(d), full spectrum in (e). The RMSE increases with higher acceleration and stays below 5% when computed for the individual metabolites, and overall below 3% (when considering the complete spectrum) up to 5X.

89
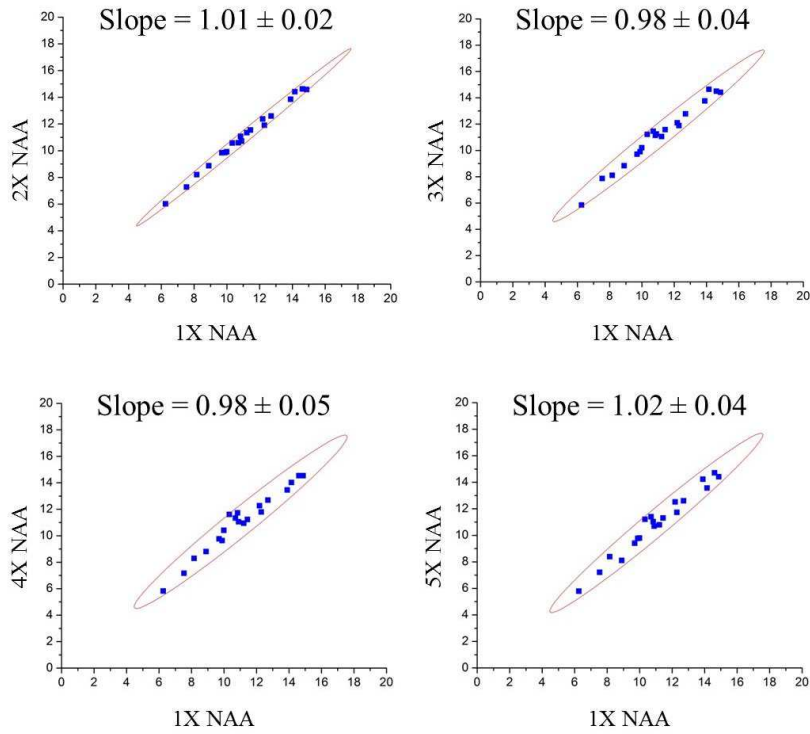
Figure 4.14 Correlation plots (1X vs 2X − 5X) of mean NAA intensities from the 20 pediatric brain MRSI datasets.
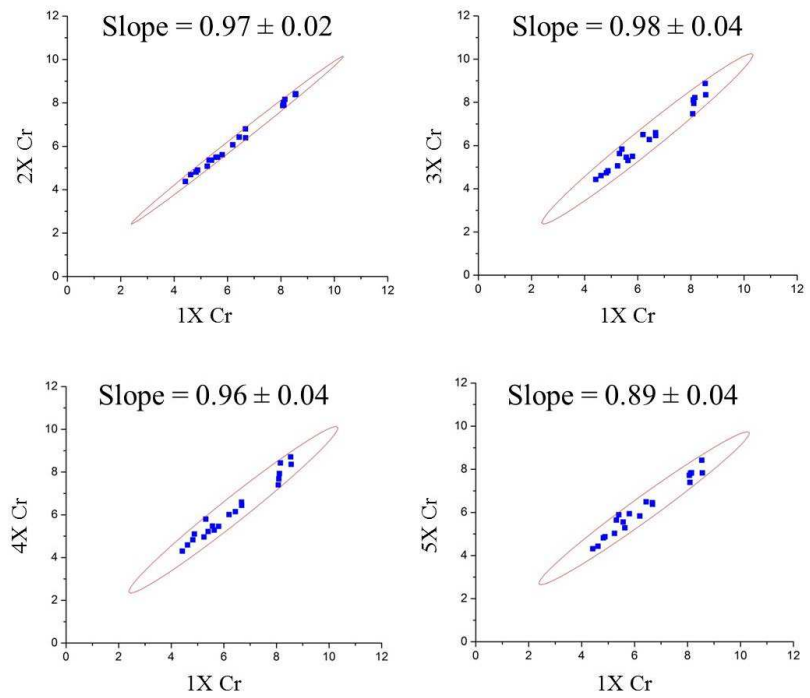
Figure 4.15 Correlation plots (1X vs 2X − 5X) of mean creatine intensities from the 20 pediatric brain MRSI datasets.
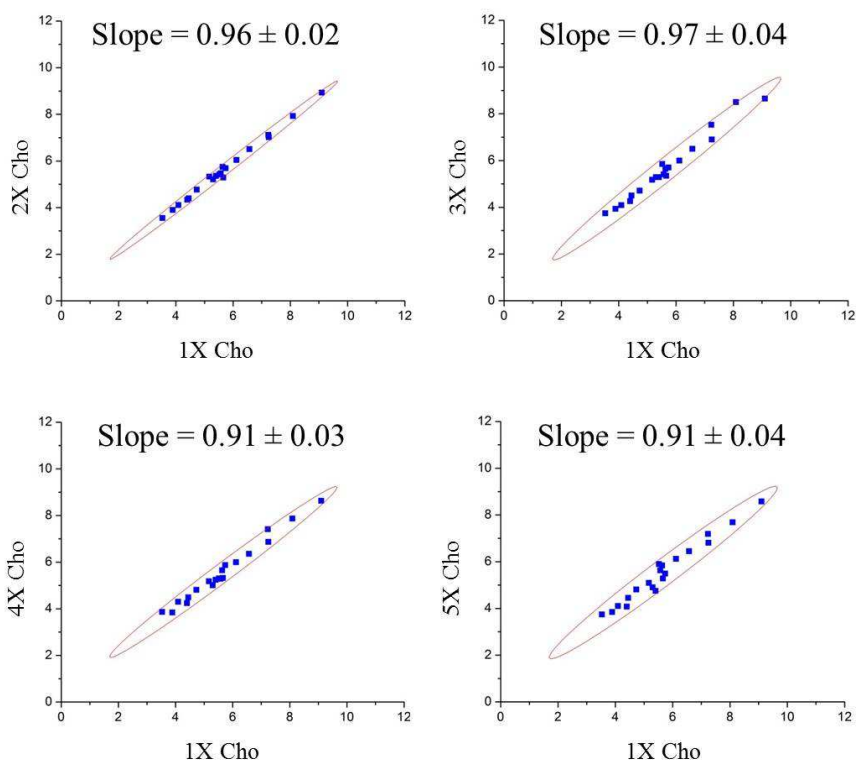
Figure 4.16 Correlation plots (1X vs 2X − 5X) of mean choline intensities from the 20 pediatric brain MRSI datasets.

Correlation graphs for the metabolites NAA, creatine, and choline are depicted in Figures 4.14, 4.15, and 4.16 respectively. Mean metabolite intensities were computed for each of the 20 pediatric MRSI datasets and plotted against the corresponding 1X reference metabolite intensities as a function of acceleration (2X – 5X). As seen from the plots, a very high magnitude of correlation (with the slope close to one in each case) exists between the 1X and 2X-5X reconstructions, for each individual metabolite within a 95% confidence interval. Although deviations from the gold standard increase with increasing acceleration, no metabolite data point lies outside the confidence interval represented by the ellipse, with very few instances in which the points are located close to or at the boundary of the ellipse. This indicates that even individual metabolite intensities

in the CS-MRSI reconstructions maintained high fidelity with the 1X fully sampled reference, for acceleration factors 2X – 5X, with insignificant loss of information.

Tables B.1 and B.2 show the means ± standard deviations of three different metabolite ratios for acceleration factors of 1X – 5X for the each individual pediatric MRSI dataset. The 20 datasets that were analyzed were divided into two main categories, namely, tumor cases (6, includes resected tumors) and non-tumor (14) datasets. Only voxels from the interior of the brain (corresponding to the selected VOI during imaging) were chosen and analyzed in both the above mentioned categories. In both groups, the mean metabolite ratios for accelerations 2X – 5X are comparable and have a strong correlation with the 1X values, with no statistically significant differences seen ($p > 0.05$). The lack of any significant differences/variations indicates that the accelerated reconstructions of these critical biomarkers in both tumor and non-tumor datasets is faithfully preserved and comparable to the 1X even at an acceleration factor of five.

4.4   Discussion & Conclusions

In this study, the *in vivo* application of compressed sensing to pediatric MRSI demonstrates that a quantitatively accurate reconstruction can be achieved by sampling only 20% of the k-space, thus, significantly reducing the scan time in spectroscopic imaging. This will facilitate the integration of MRSI in clinical protocols, leading to a more comprehensive evaluation of metabolite maps that contain vital prognostic and diagnostic information. The inclusion of MRSI scans can prove critical in children as one can monitor the spatial changes in these important biomarkers, particularly in the developing and diseased brain. It could also help identify specific markers in common

childhood cancers of the brain and central nervous system that have an incidence of 5.3 per 100,000 in the 0 – 19 years age group [154].

The CS accelerated reconstructions maintained high spectral accuracy for up to 80% under sampling for each of the 20 pediatric brain MRSI datasets that were analyzed, with overall reconstruction errors that were lower than 3% (and individual metabolite errors that were less than 5%). This clearly demonstrates the feasibility and repeatability of our approach to produce consistently faithful results in a varied group of clinical MRSI datasets. The previous study from our group focused on the evaluation of the in house developed reconstruction algorithm in adult patients, including both normal and tumor cases [71]. In the current study, we wanted to further validate the reproducibility of our approach in pediatric patients as only a handful of studies have investigated the possibility of fast imaging in pediatric MRI and MRSI datasets [148-153], as previously discussed. This study, thus, presents a more detailed analysis of the application of CS-MRSI in the pediatric brain.

Apart from the qualitative inspection of the metabolite maps and spectra, the CS-MRSI reconstructions for various accelerations and the reference 1X dataset are statistically comparable, as indicated by the p-values generated from a series of voxel-wise paired t-tests. Derived parameters, like metabolite ratios, are also accurately reconstructed up to an acceleration factor of five. A p-value threshold of 0.05 was considered optimal as in this study we were testing for non-significant differences and assessing spectral and spatial fidelity in the reconstruction. A $p\text{-value} < 0.05$ was considered to indicate a statistically significant difference between the reference and accelerated dataset, and thus, suggestive of a failed reconstruction.

93

The reconstructions at 7X and 10X were found to be statistically different from the 1X for most metabolite ratios, indicating increased deviation and higher reconstruction errors. Our ongoing work focuses on identifying the optimal acceleration factor between 5X and 10X that would result in a statistically comparable reconstruction for all considered datasets. Another area that requires further investigation is the selection of an optimal undersampling mask that produces the least errors and is tailored to the CS-MRSI reconstruction at hand, particularly at higher accelerations (> 4X). A bad undersampling mask, as previously discussed by Lustig *et al* [70] and in more recent studies [155, 156], might result in a poor reconstruction.

Furthermore, certain user-dependent factors like inconsistent post processing and spectral fitting of the MRSI datasets can also contribute to differences between the original and undersampled datasets. Increased deviations (in either direction) in the metabolite peak amplitudes have been observed with higher under sampling. Various contributing factors to the reconstruction error include the VOI that was selected, size of the MRSI grid, SNR of the original k-space data acquired, along with a sub-optimal choice of regularization parameters for the reconstruction algorithm. The errors can be particularly significant when there is a huge SNR penalty to begin with in MRSI (for e.g. when imaging difficult regions), causing the CS reconstruction to break down.

The metabolic changes measured by MRS(I) can aid in the characterization of numerous neurological disorders. It is critical to estimate the sensitivity and specificity of changes in metabolite concentrations associated with each disease prior to the application of any acceleration technique. For e.g. MRS(I) has been found to be highly sensitive and specific to identifying metabolic changes in Alzheimer's disease and mild cognitive

impairment, wherein NAA, choline, and myo-inositol (mI)/creatine ratios are assessed [157-159]. In a clinical study by Moats *et al* [158], a receiver operating characteristic (ROC) of mI/Cr and NAA/Cr ratios was employed to make a diagnosis. A decrease in NAA concentration has direct correlation with the severity of neuropathological findings [159] along with an increase in mI levels, establishing the NAA/mI index as a sensitive marker of abnormalities in cognitive function. In epileptic seizures, MRS(I) has been found to be highly sensitive to a decrease in NAA levels in the epileptogenic focus, even when no abnormality was detected in the accompanying MR scans in a majority of patients [160]. Cerebral lactate has also been detected in patients with seizures as compared to the control group [160, 161].

MRS(I) can identify marked NAA reduction and lactate increase in stoke/cerebral ischemia, while inconsistent changes have been measured in the peaks from choline and creatine [162]. MRS(I) has also proven beneficial in differentiating brain tumors from non-neoplastic lesions (72% sensitivity, 92% specificity [163]), and evaluating low grade vs high grade gliomas (93% sensitivity, 60% specificity [164]). Various pediatric specific neurological abnormalities like inherited metabolic disorders, hypoxia ischemia, and traumatic brain injury (TBI) can be assessed with ^{1}H spectroscopy [165]. In all the discussed neurological conditions, MRS(I) shows high sensitivity and specificity to the detection of major metabolites like NAA, creatine, and choline. Other metabolites such glutamate, glutamine, GABA, alanine, and lactate are in a majority of cases not reliably detected owing to their low concentration and considerable spectral overlap with stronger resonances in the MRS spectrum. In such instances, specialized pulse sequences that permit selective excitation of these hard to detect metabolites [106, 107, 166-171] can be

combined with acceleration techniques to increase the sensitivity and specificity of MRSI. For e.g. the lactate specific CS-MRSI sequence that was discussed in Chapter 3 could prove very useful in the enhanced detection of lactate metabolism in solid tumors. Specialized editing sequences have also been developed for the improved detection of metabolites such as γ-Aminobutyric acid (GABA) [169, 171], 2-hydroxyglutarate (2HG) [166, 167], glutamine and glutamate [170], and glycine [168]. These sequences can be combined with fast acquisition strategies like CS for a precise, high-speed detection of these smaller biomarkers.

The retrospective application of CS under sampling to MRSI was the main limitation of this study. However, we believe our work is an important step in the validation of CS-MRSI reconstructions in pediatric brain datasets, with future studies focusing on the prospective implementation. Another limitation of the study was that we did not test CS in conjunction with 3D MRSI datasets, which cannot be acquired in patients due to the prohibitive scan time. For e.g. considering one signal average and a TR of 1 s, a 16x16x16 spectroscopic grid would require the acquisition of 4096 signals, leading to a total scan time of approximately 1 hour and 8 mins, which is prohibitive where patients are under general anesthesia.

In conclusion, it has been demonstrated that 2D MRSI can be accelerated by 80% using compressed sensing in the pediatric clinical setting, with minimal loss in spectral fidelity and accuracy in metabolite quantification. This methodological advancement has the potential to increase the utility of MRSI in routine clinical evaluation of brain morphology and function, as well as in other organs.

(**<u>Note:</u>** Chapter 4 is based on the paper – R. Vidya Shankar, H. H. Hu, J. C. Chang, and V. D. Kodibagkar, "2D MR Spectroscopic Imaging of the Pediatric Brain Using Compressed Sensing", in preparation for submission to *Radiology*.)

CHAPTER 5

CLINICAL IMPLEMENTATION OF CS-MRSI & OPTIMIZATION OF CS

UNDERSAMPLING

5.1 Prospective CS-MRSI

The objective of this study was to implement CS acquisitions prospectively on a GE Discovery 3 T clinical MRI scanner and assess the fidelity of the CS-MRSI reconstructions. Pseudo-random undersampling masks [70] designed to skip phase encodes, corresponding to acceleration factors 2X, 3X, 4X, and 5X were incorporated into the GE 'presscsi' pulse sequence via the EPIC programming environment. The CS-MRSI sequence was tested on the 'braino' metabolite phantom (12.5 mM NAA, 10 mM creatine, 3 mM choline) by prospectively acquiring the 1X – 5X MRSI datasets, with the following acquisition parameters: 16x16x2048 grid, TE/TR = 144/2000 ms, 1 average, 10 mm slice thickness, total acquisition time 8 min 40 s (1X), 4 min 20 s (2X), 2 min 54 s (3X), 2 min 20 s (4X), and 1 min 44 s (5X). All CS-MRSI datasets were reconstructed and post processed using the procedures outlined previously in Chapters 3 and 4 to generate the final metabolite maps at each acceleration factor.

Figure 5.1 shows the acquired k-space maps of the 1X reference and 2X – 5X CS-MRSI datasets as an illustration of the prospective undersampling on the scanner. The metabolite maps of NAA, creatine, and choline for each acceleration factor are illustrated in Figure 5.2. As seen from the figure, the integrated metabolite intensities maintain high fidelity with the 1X reference, with negligible loss of information. No statistically significant differences were seen between the 1X reference and CS-MRSI reconstructions

for up to 80% undersampling. A decrease in the peak amplitudes was observed with increasing acceleration; this can be attributed to a sub-optimal choice of parameters in the iterative reconstruction algorithm along with slight differences in the prospectively acquired signal intensities at each acceleration factor as compared to the 1X reference. The normalized RMSEs at all acceleration factors are depicted in Figure 5.3(a), wherein the reconstruction error remains below 3.5 % for up to an acceleration of 5X.
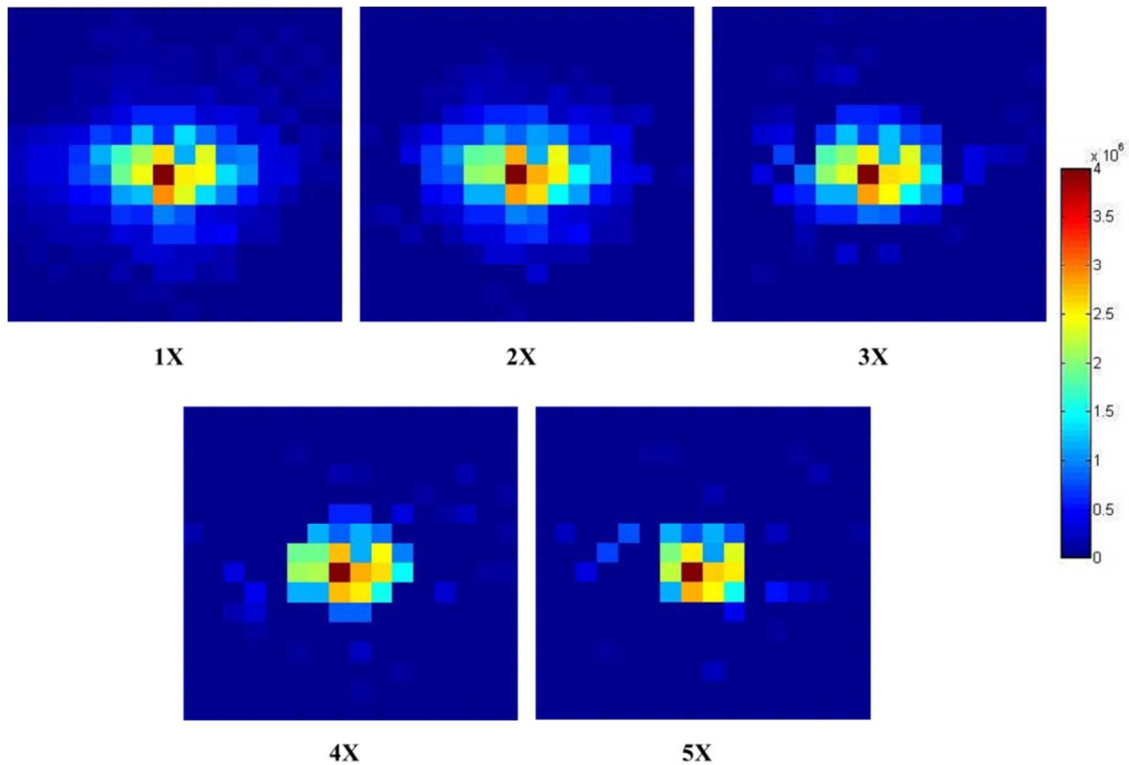
Figure 5.1 K-space map (kx, ky, kt=0) from a prospectively under-sampled 2D PRESS-MRSI dataset (3T, TR/TE= 1200/35 ms, 16X16X1028) acquired on a metabolite phantom.

Figure 5.3 (b) lists statistical comparisons between the 1X and accelerated datasets. As seen from the table, the p-values indicate a strong correlation between accelerations 1X – 4X. The p-values for the 1X vs 5X case are weaker, but not statistically different ($p > 0.05$) from the ground truth.
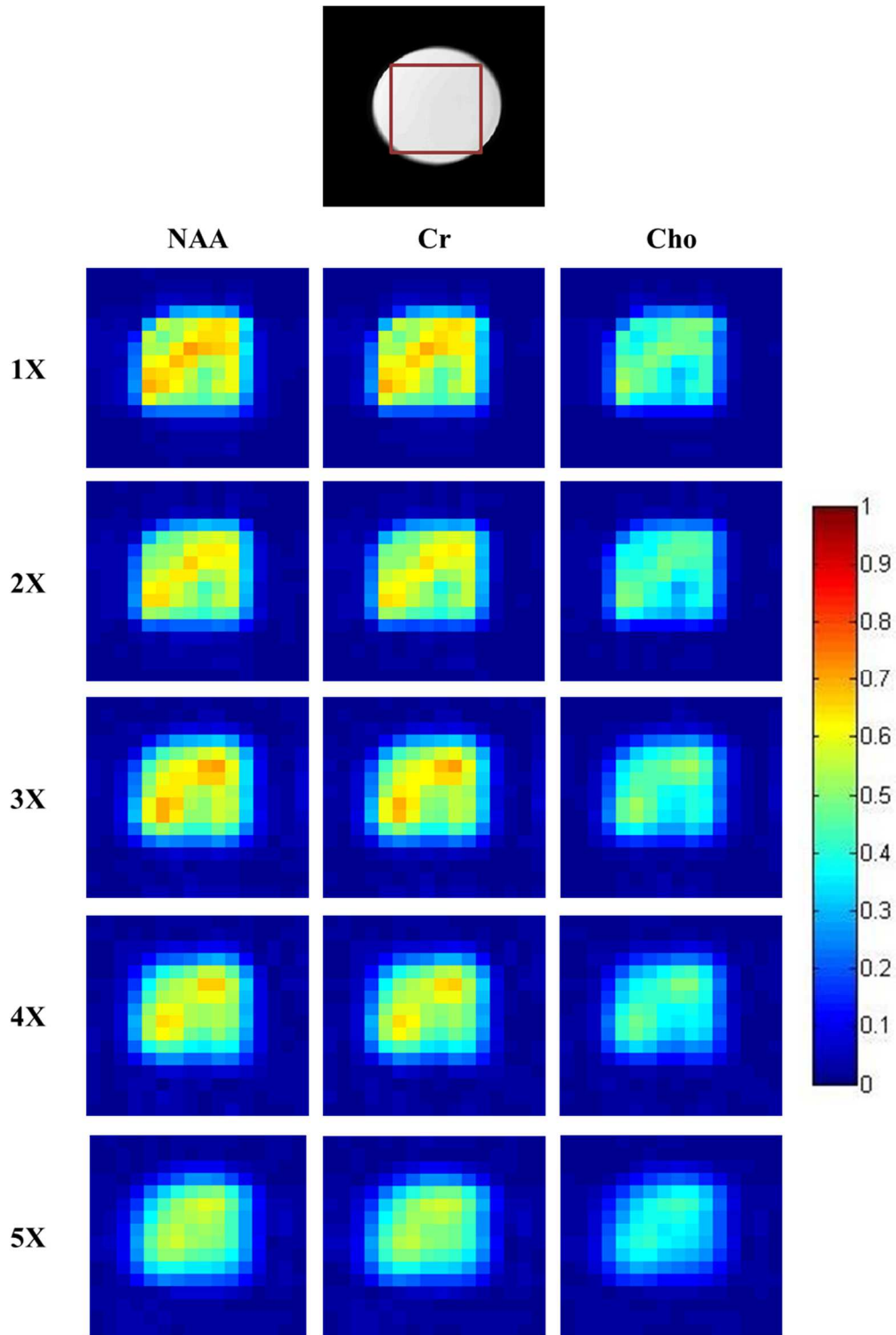
Figure 5.2 GE 'braino' metabolite phantom - 16x16x2048 matrix, TE = 144 ms, TR = 2000ms, 1 average, 10 mm slice thickness, total acquisition time 8 min 40 s (1X). Metabolite maps of NAA (12.5 mM), creatine (10 mM), and choline (3 mM) for various acceleration factors (2X-5X).

nRMSE

Acceleration	p-value		
	NAA	Cr	Cho
1X vs 2X	0.69	0.56	0.62
1X vs 3X	0.46	0.43	0.3
1X vs 4X	0.19	0.19	0.11
1X vs 5X	0.10	0.07	0.06

(a)   **(b)**
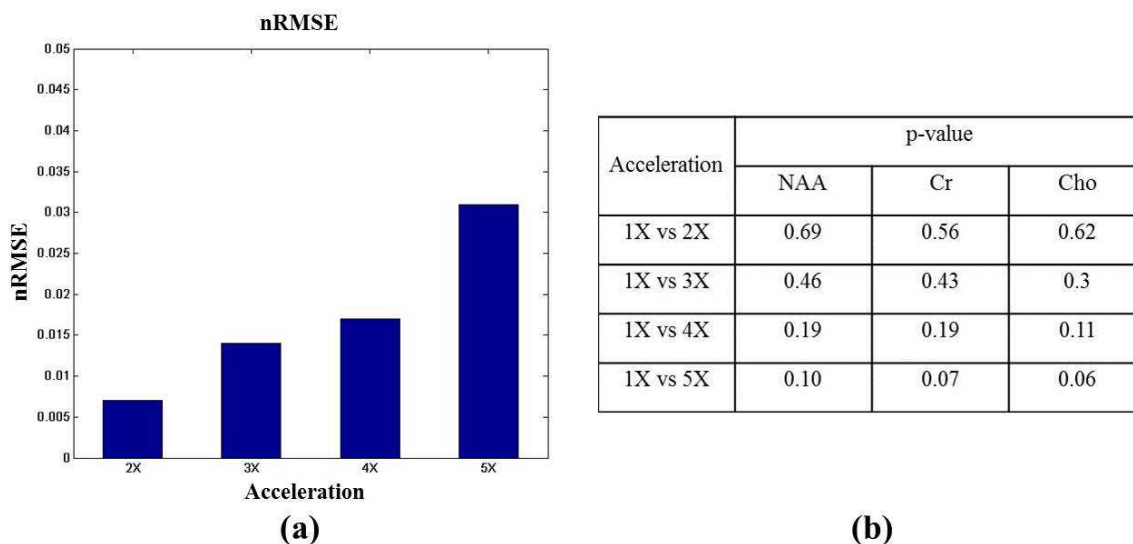
Figure 5.3 (a) The normalized RMSEs from the 'braino' phantom for acceleration factors 2X – 5X. (b) Statistical comparisons with the 1X reference dataset.

5.2   Optimal Mask for CS-MRSI

Random undersampling, or pseudo-random undersampling when considering MRI/MRSI, is a key CS requirement, as previously discussed in Chapter 2. A random selection of sampling locations ensures incoherent aliasing artifacts, which can subsequently be removed by signal denoising procedures [70]. A pseudo-random mask undersamples the peripheral regions of k-space more as compared to the center. This is preferred as most of the signal energy is in the low frequency components that are located at the k-space origin. However, the choice of an optimal sampling mask (along with the type of sparsifying transform) is critical for obtaining an accurate reconstruction. Not all pseudo-random sampling patterns achieve a sufficient degree of incoherence required in CS for accurate signal recovery. The key requirement to determining an optimal mask is

101

to examine the point spread function (PSF), which is a useful tool to measure incoherence, as discussed by Lustig *et al* [70]. Pixels do not display any interference when sampling under the Nyquist criterion i.e. the non-diagonal terms of the PSF are essentially zero $PSF(i,j)_{i \neq j} = 0$. Interference between pixels is caused when the Nyquist limit is violated, with the emergence of non-zero off-diagonal terms. The degree of incoherence can be measured by calculating the maximum value of the side lobe-peak ratio (SPR) when undersampling below the Nyquist limit [70]. The sampling pattern at a particular acceleration with the least peak interference can be considered a good candidate for an optimal mask.

Various methods have been suggested to identify the optimal mask for a particular application in MRI [57, 155, 156, 172, 173]. In the study by Knoll *et al*, a fully sampled template image was employed to formulate the probability density function (PDF) to be equal to the normalized k-space power spectrum [155]. This ensured that the locations with highest energy in k-space were more likely to be sampled. Approaches by Liu *et al* and Ravishankar *et al* sought to determine the best mask based on errors in k-space following a CS reconstruction [172, 173]. Either an existing sampling pattern was modified [173], or one was built from scratch [173] by determining the k-space coefficients with the highest reconstruction errors and subsequently sampling that location [156]. All the above described approaches have been used to determine an optimal mask for CS-MRI. However, there is no literature on finding a mask suited to CS accelerated proton MRSI. The following sub-section of this chapter seeks to identify an optimal sampling mask at a certain acceleration factor using both *in vitro* and *in vivo* ^{1}H MRSI data.

5.3.1 Methods and Sampling Pattern Design

Phantom (metabolite solution – 12 mM NAA, 10 mM creatine, 3 mM choline) MRSI data was acquired on a Philips 3 T Ingenia scanner with the following scan parameters – TR/TE = 1500/48 ms, 16x16x2048 matrix, 1 average, 10 mm slice. Acquisition parameters for the corresponding T_1 anatomical scout were – TR/TE = 83/7 ms, 128 x128 matrix, 5 mm slice, 1 average. Four different types of masks were evaluated at accelerations 2X – 5X in this study, namely, the low resolution, variable density (VD), iterative design, and *a priori* sampling strategies. The number of k-space sampling locations for a 16x16x2048 grid at each acceleration factor are as follows: 128 (2X), 84 (3X), 64 (4X), 51 (5X), 38 (7X), and 26 (10X). In the low resolution mask, all samples at each acceleration factor were placed at the center of k-space. The pseudo-random undersampling strategy described by Lustig *et al* [70] that was adopted in Chapters 3 and 4 of this dissertation was employed to generate the VD mask.

In the iterative design approach, the k-space locations with the highest reconstruction errors were identified and sampled, as proposed by Liu *et al* [172]. An initial mask 'M' containing a certain percentage of samples at the k-space center (derived from the probability density function (pdf) employed in the pseudo-random undersampling design) was used to retrospectively undersample and reconstruct the test MRSI dataset. Subsequently, the k-space location with the highest error was identified and that location in the mask 'M' was then sampled. This procedure, which is similar to a brute-force implementation, was repeated till the mask 'M' had enough samples to justify the chosen undersampling rate. The *a priori* mask was derived from the k-space of the anatomical reference scout acquired using the same field of view (FOV) as the MRSI

dataset. The scout k-space was cropped to match the corresponding MRSI spatial grid size (16x16). Intensity thresholding was applied to select the highest energy locations of k-space to form the mask at a certain acceleration factor.

5.3.2 Simulation Results

Figures 5.4 – 5.6 depict the simulation results for the phantom MRSI data. At 2X, all four undersampling patterns resulted in quantitatively comparable results, with no statistically significant differences between the 1X fully sampled reference and the CS-MRSI reconstructions corresponding to each type of mask. At 3X, increasing deviations from the ground truth were found in the low resolution CS-MRSI reconstructions.
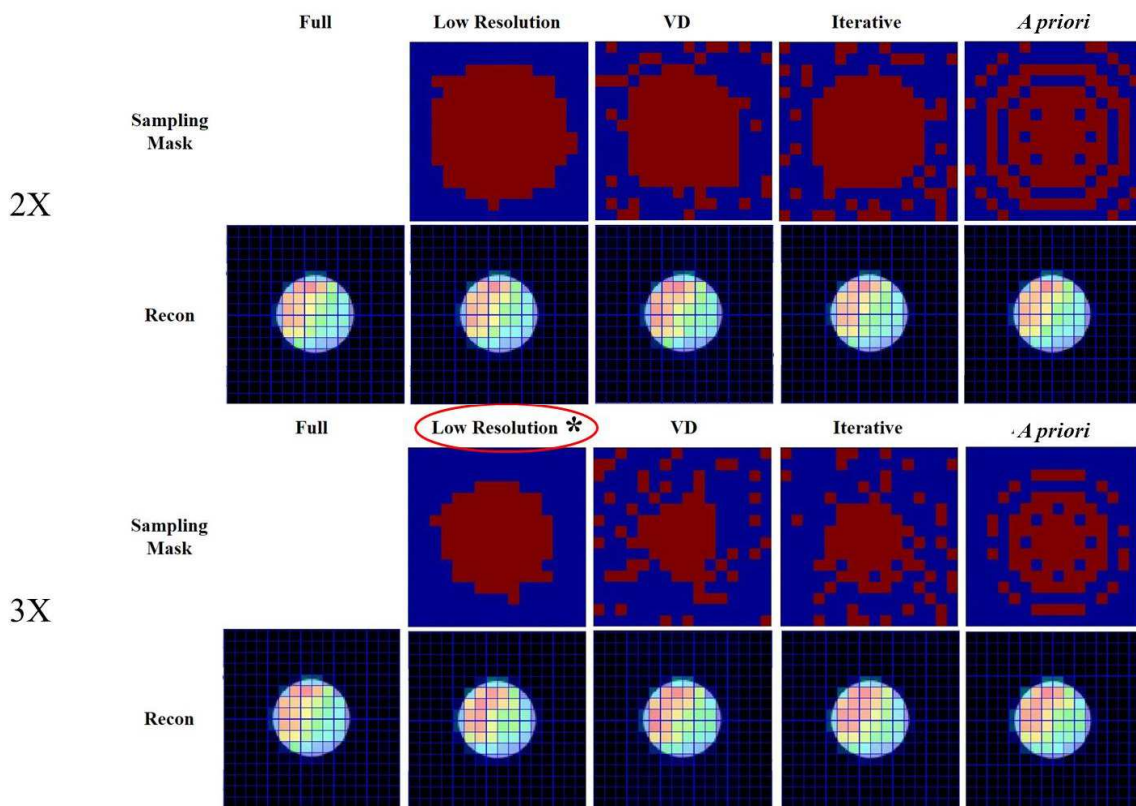
Figure 5.4 Reconstruction (mean integrated intensity) results at 2X and 3X using the 4 types of masks (* indicates p < 0.05).

At the 4X and 5X acceleration factors shown in Figure 5.5, the low resolution CS-MRSI reconstructions continued to show increasing deviations from the 1X reference. The iterative design reconstruction broke down at 4X, whereas both the VD and *a priori* masks maintained statistical similarity ($p > 0.05$) with the 1X up to five-fold acceleration. The reconstruction results at 7X and 10X are illustrated in Figure 5.6, wherein the reconstructions from all four masks fail.
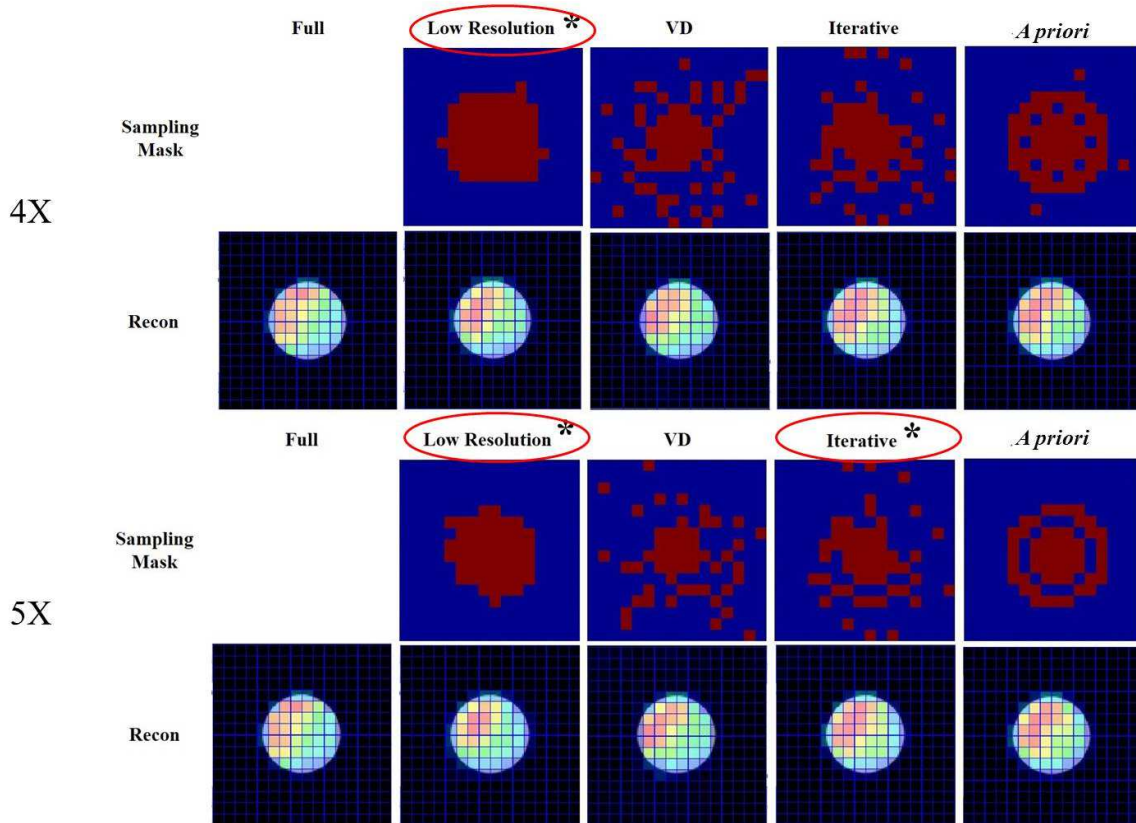
Figure 5.5 Reconstruction (mean integrated intensity) results at 4X and 5X using the 4 types of masks (* indicates $p < 0.05$).

The normalized RMSEs (nRMSE) from all the reconstructed CS-MRSI datasets corresponding to each of the four types of masks at 2X – 5X, 7X, and 10X acceleration factors have been depicted in Figures 5.7 and 5.8. Figure 5.7 shows the nRMSE that was

computed considering the entire MRSI dataset, while in the Figure 5.8 only the voxels containing the phantom were considered when computing the nRMSE. The nRMSEs from the phantom dataset are comparable for the low resolution, VD, iterative design and *a priori* undersampling, with no significant differences in the reconstruction error between the four sampling designs. These results suggest that the nRMSE might not be the best metric to employ when evaluating different undersampling patterns and CS-MRSI reconstruction accuracy.
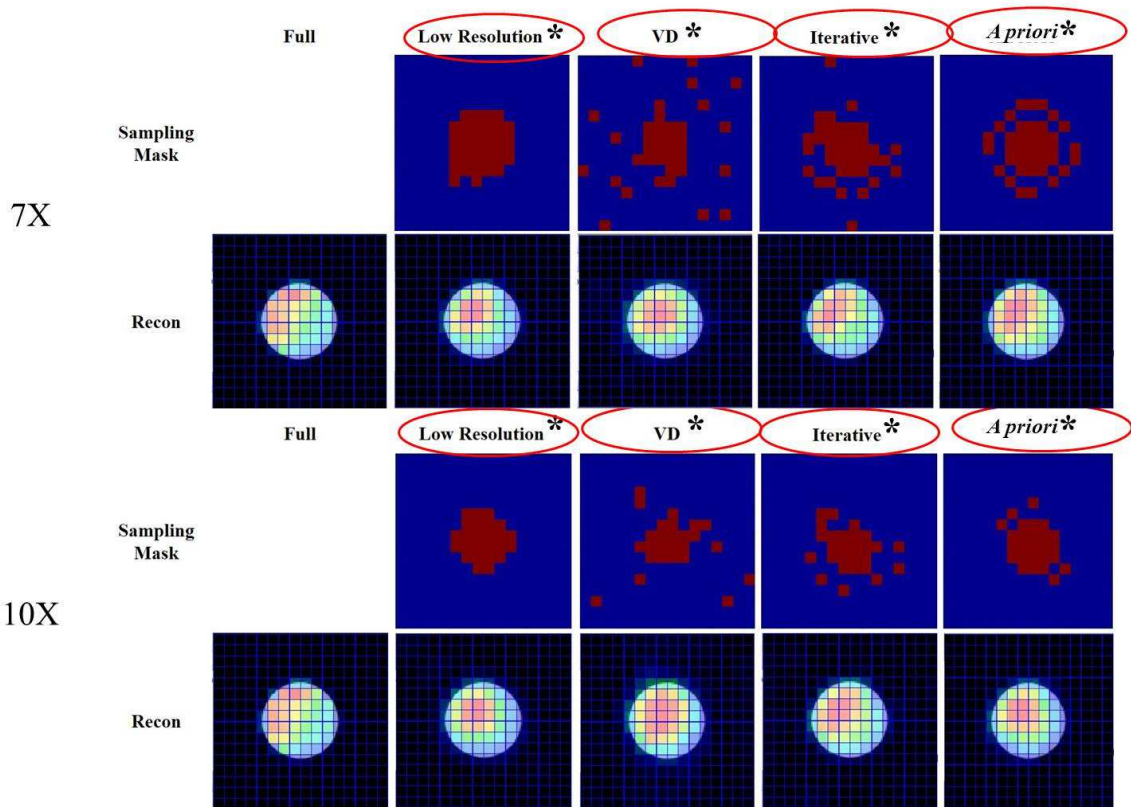
Figure 5.6 Reconstruction (mean integrated intensity) results at 7X and 10X using the 4 types of masks (* indicates $p < 0.05$). All reconstructions fail at 7X and 10X.

Table 5.1 lists the mean metabolite ratios ± standard deviations for the CS reconstructions obtained using the four sampling masks for the phantom MRSI dataset.

106
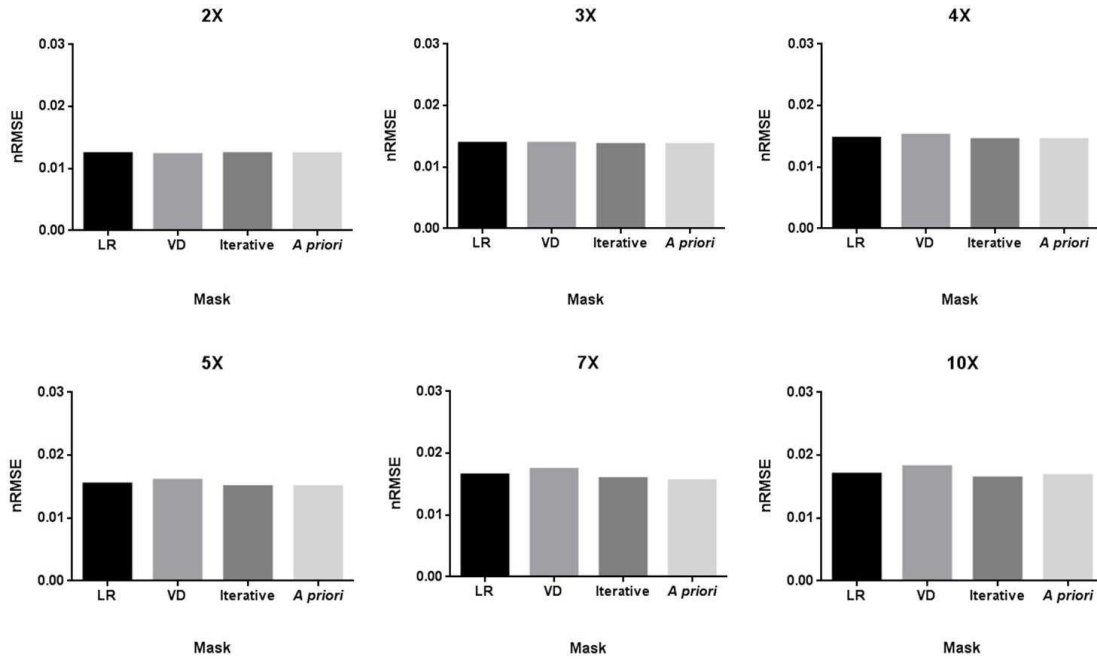
Figure 5.7 The normalized root mean square errors (nRMSEs) for accelerations 2X - 5X, 7X, and 10X corresponding to each type of mask. The nRMSE was computed for the entire MRSI dataset. (LR- low resolution, VD – variable density)
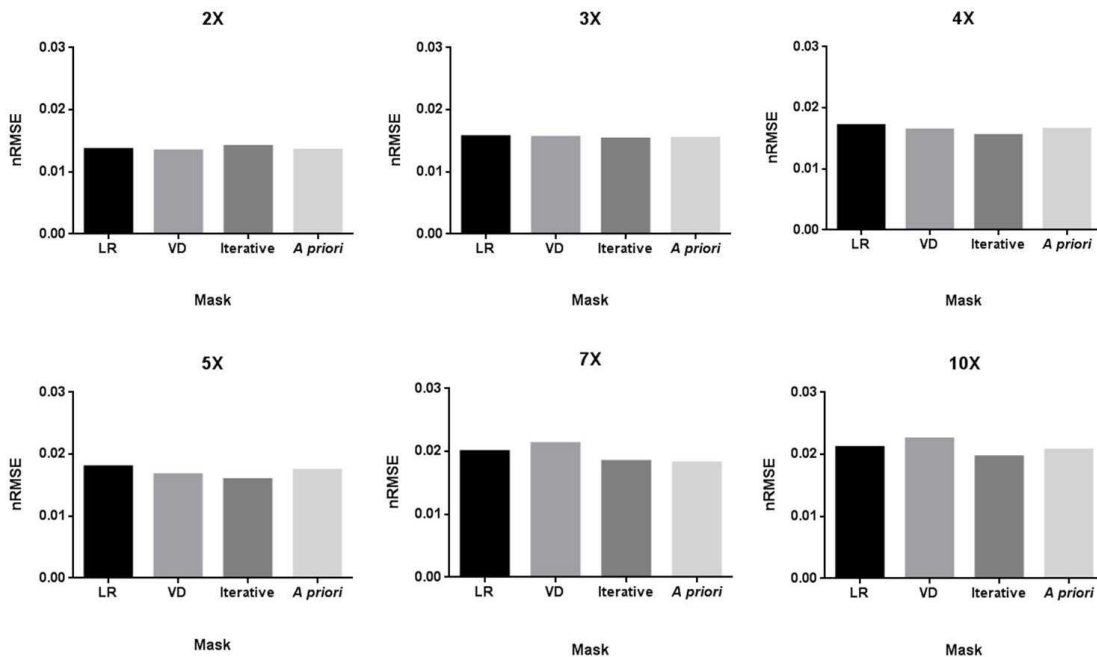
Figure 5.8 The nRMSEs for accelerations 2X - 5X, 7X, and 10X corresponding to each type of mask. Only the voxels containing the phantom were considered when computing the nRMSE. (LR- low resolution, VD – variable density)

107

Table 5.1 Mean metabolite ratios ± standard deviations for the phantom MRSI dataset corresponding to low resolution, VD, iterative design, and *a priori* undersampling at 1X – 5X, 7X, and 10X accelerations (*p < 0.05 as compared to the 1X).

(LR – Low Resolution, VD – Variable Density, NAA – N-acetylaspartate, Cr – creatine, Cho – choline)

Phantom Dataset		LR	VD	Iterative	*A priori*
NAA/Cr (Mean ± SD)	1X	2.48 ± 0.56	2.48 ± 0.56	2.48 ± 0.56	2.48 ± 0.56
	2X	2.37 ± 0.67	2.36 ± 0.70	2.38 ± 0.64	2.43 ± 0.94
	3X	2.21 ± 0.36 (*)	2.36 ± 0.71	2.37 ± 0.73	2.38 ± 0.90
	4X	2.17 ± 0.32 (*)	2.31 ± 0.37	2.42 ± 0.75	2.31 ± 0.40
	5X	2.26 ± 0.37 (*)	2.40 ± 1.05	2.29 ± 0.33 (*)	2.42 ± 0.86
	7X	2.29 ± 0.30 (*)	2.27 ± 0.29 (*)	2.22 ± 0.25 (*)	2.25 ± 0.28 (*)
	10X	2.30 ± 0.38 (*)	2.26 ± 0.26 (*)	2.23 ± 0.26 (*)	2.29 ± 0.57 (*)
Cho/NAA (Mean ± SD)	1X	0.66 ± 0.11	0.66 ± 0.11	0.66 ± 0.11	0.66 ± 0.11
	2X	0.68 ± 0.14	0.68 ± 0.13	0.67 ± 0.12	0.69 ± 0.13
	3X	0.68 ± 0.12	0.64 ± 0.14	0.65 ± 0.12	0.67 ± 0.14
	4X	0.68 ± 0.11	0.68 ± 0.11	0.68 ± 0.12	0.66 ± 0.16
	5X	0.68 ± 0.10	0.70 ± 0.07	0.65 ± 0.12	0.66 ± 0.13
	7X	0.7 ± 0.09	0.62 ± 0.10	0.65 ± 0.10	0.67 ± 0.12
	10X	0.73 ± 0.07 (*)	0.65 ± 0.12	0.66 ± 0.09	0.72 ± 0.11 (*)
Cho/Cr (Mean ± SD)	1X	1.62 ± 0.42	1.62 ± 0.42	1.62 ± 0.42	1.62 ± 0.42
	2X	1.56 ± 0.29	1.53 ± 0.24	1.54 ± 0.23	1.61 ± 0.39
	3X	1.47 ± 0.20	1.48 ± 0.21	1.50 ± 0.24	1.53 ± 0.35
	4X	1.46 ± 0.22 (*)	1.56 ± 0.23	1.57 ± 0.32	1.48 ± 0.30
	5X	1.53 ± 0.20	1.53 ± 0.16	1.46 ± 0.26 (*)	1.50 ± 0.21
	7X	1.43 ± 0.18 (*)	1.46 ± 0.16 (*)	1.41 ± 0.23 (*)	1.49 ± 0.19 (*)
	10X	1.60 ± 0.43	1.46 ± 0.28 (*)	1.42 ± 0.22 (*)	1.58 ± 0.40
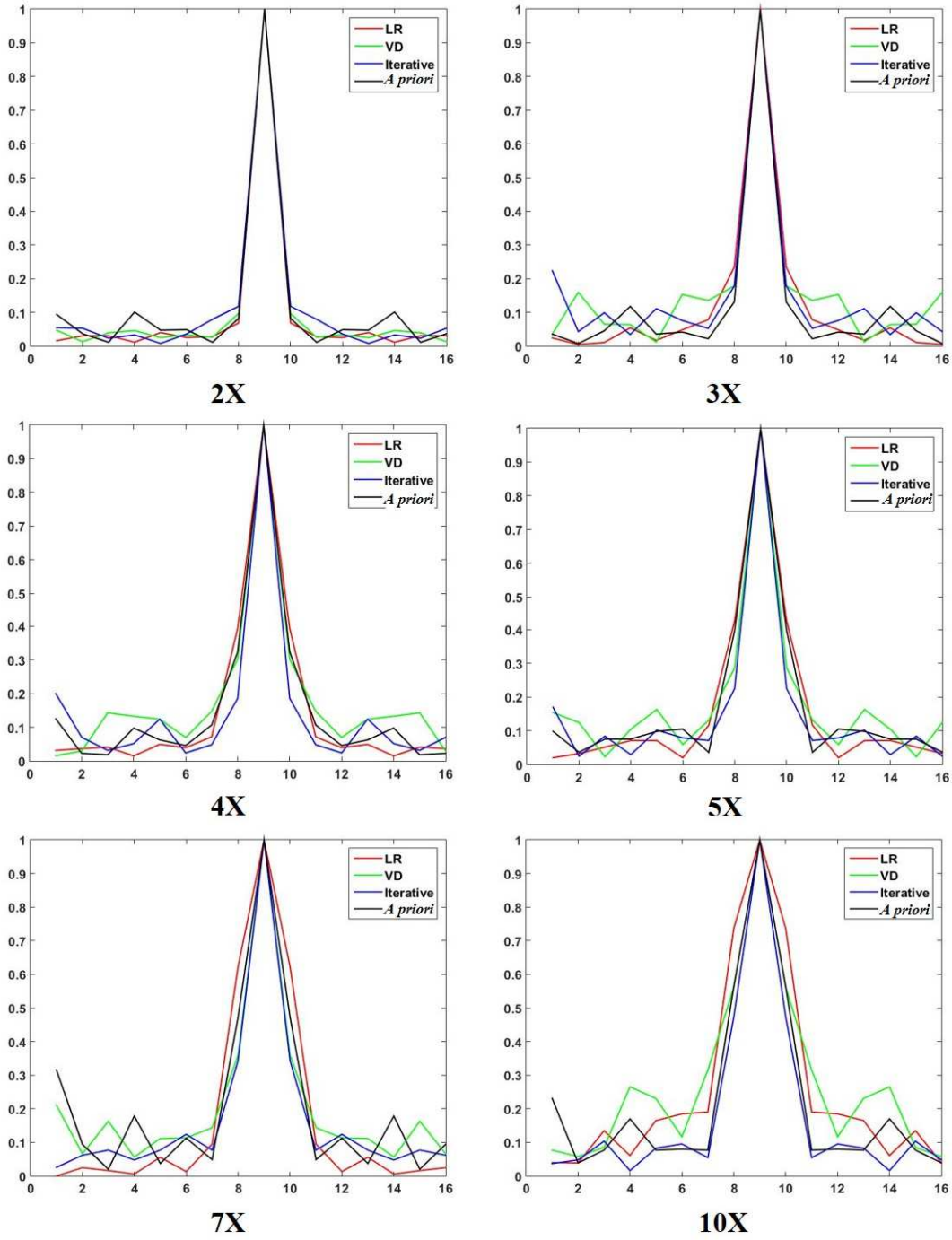
Figure 5.9 The PSFs of the four types of masks at each acceleration factor. (LR – Low Resolution, VD – variable density)

As seen from Table 5.1, at 2X acceleration there are no statistically significant differences between the metabolite ratios from each sampling scheme and the 1X fully sampled reference. Significant differences in the metabolite ratios are seen between the 1X and (3X – 5X, 7X, 10X) datasets reconstructed using the low resolution sampling mask. Both *a priori* and VD undersampling show no statistical significance (p > 0.05) up to 5X, while the iterative design reconstructions show fidelity up to 4X when compared with the 1X reference. All reconstructions from the four sampling schemes fail at 7X and 10X.

5.3.3 Discussion & Conclusions

A preliminary study was conducted to assess the effect of different undersampling masks on the CS-MRSI reconstruction quality. Four sampling schemes, namely low resolution, VD, iterative design, and *a priori* were retrospectively evaluated on a phantom MRSI dataset. The *a priori* and VD undersampling masks can be considered equivalent to the 'Key-thresh' and 'CS-points' masks previously employed by our group for fast acquisitions in dynamic contrast enhanced (DCE) MRI [174], with reconstructions maintaining high statistical fidelity up to 5X acceleration. All retrospectively generated CS-MRSI datasets were reconstructed using the algorithm described in [71], which was previously employed in Chapters 3, 4, and 5 of this dissertation. Reconstruction parameters were kept the same across the board to ensure that any resulting differences can be attributed to the type of mask being employed. Simulation results indicate that both the *a priori* and VD undersampling masks maintain high fidelity with the 1X reference up to 5X acceleration. The low resolution reconstructions showed statistically significant differences from the 1X with increased

undersampling. The breakdown in reconstruction even at a relatively lower acceleration such as 3X can be attributed to the placement of all samples at the k-space center, which does not satisfy the random undersampling criterion necessary in CS.

The iterative sampling method was quantitatively comparable to the *a priori* and VD undersampling schemes even at higher accelerations. In this experiment, no distinction was made between the low and high frequency locations of k-space when selecting the points with maximum error, contrary to that employed previously by Liu *et al* [172]. This approach was chosen to ensure a brute-force evaluation of the k-space error locations since the computational complexity of evaluating a low resolution 16 x 16 spatial grid in MRSI is comparatively low as compared to the matrix sizes employed in MRI. In the test datasets, the iterative design approach showed a tendency towards sampling the center more densely as compared to the peripheral regions of k-space (as can be seen from the masks in Figures 5.4 – 5.6), indicating that a sampling of lower frequencies reduces the reconstruction error more than the higher frequencies. A similar result has been found in a recent study conducted by Zijlstra *et al* [156]. Future work could involve partitioning the k-space into high and low frequency regions while checking for the maximum error, in order to ensure an optimal ratio of low/high frequency sampled locations. The iterative design method is tailored to each specific dataset, is retrospective in application, and can be computationally expensive, particularly when using larger grid sizes. More extensive simulations are required to determine whether the same mask can be employed for a particular anatomy for e.g. in brain MRSI.

VD undersampling suggested by Lustig *et al* has shown high reconstruction fidelity in the datasets evaluated in various published CS-MRSI studies [71, 72, 85] as

well as those included in this thesis. While the VD method satisfies the CS requirement of pseudo-random undersampling, not all masks might be good candidates to achieve an accurate reconstruction. Furthermore, for low resolution MRSI datasets, only assessing the PSF (and degree of incoherence) of a sampling pattern may not be the only major criterion in determining an optimal mask. An observation along these lines has previously been made while investigating undersampling patterns in MRI [57, 156]. Due to the limited number of sampling points in MRSI, a less than optimal placement of even a few samples might lead to an inaccurate reconstruction.

The *a priori* mask was extracted from the k-space of the anatomical scout that was acquired using the same FOV as the MRSI data. The k-space was cropped to match the size of the MRSI grid (16x16) and the highest energy locations were selected to design a mask at the desired undersampling factor. The *a priori* mask is simple to implement as an accompanying anatomical reference is always acquired prior to the MRSI scan. Thus, this mask can be prospectively implemented on the scanner and offers the added advantage of being tailored to the acquired MRSI data.

In conclusion, a preliminary attempt was made to identify an optimal sampling mask in MRSI. More extensive simulations and quantitative comparisons could help determine a library of masks best suited to a particular application/dataset/anatomy. Other factors such as optimizing the regularization coefficients and the reconstruction algorithm, along with identifying an optimal sampling density for each data type could improve reconstruction accuracy in CS-MRSI.

CHAPTER 6

CONCLUSIONS & FUTURE DIRECTIONS

The development of fast data acquisition strategies can contribute to the availability of more diagnostic information in healthcare as it could help accommodate more MR sequences and protocols within the current clinical examination window. On the other hand, rapid exam protocols could potentially offer other benefits like reduced costs, increased patient throughput, less patient discomfort, and lower susceptibility to motion artifacts. The advancement of fast imaging techniques is, thus, critical for the establishment of sophisticated yet affordable patient care. This dissertation primarily focused on accelerating magnetic resonance spectroscopic imaging (MRSI) using compressed sensing (CS). CS-MRSI sequences were implemented on both preclinical and clinical scanners and both fully-sampled and accelerated MRSI data was acquired (prospective) or simulated (retrospective) in phantoms, small animals (mice), human volunteers, and patients using three different MRI scanner platforms. Both prospectively and retrospectively undersampled MRSI datasets were reconstructed offline in Matlab using a convex optimization algorithm to obtain the best estimate of the accelerated MRSI data in comparison with the fully-sampled 1X reference. The reconstruction accuracy and spectral fidelity of all CS-MRSI datasets was further assessed by making quantitative comparisons between the 1X and undersampled datasets in terms of the peak metabolite amplitudes, relative metabolite ratios, the normalized root mean square error (nRMSE), and the total acquisition time. A pilot test was also conducted to identify an optimal sampling mask for CS-MRSI at each acceleration factor.

6.1 Preclinical CS-MRSI

CS was employed to speed-up spectroscopic imaging on the Bruker 7 T small animal MRI scanner, as detailed in Chapter 3. The lactate-CS-MRSI sequence achieved rapid mapping of the lactate peak both *in vitro* and *in vivo* in mice subcutaneously implanted with H1975 tumor cells. In the phantom, accelerations up to 10X showed no statistically significant differences from the gold standard, while prospectively undersampled MRSI acquisitions in tumor mice demonstrated negligible information loss and high fidelity even when only 20% of the k-space space locations were sampled (5X acceleration). In all experiments, it was demonstrated that CS can accelerate MRSI by five-fold, with negligible reconstruction errors and having statistical equivalence ($p > 0.05$) with the 1X fully sampled reference data.

Preclinical imaging is more SNR limited as compared to clinical imaging as the acquisition parameters such as the field of view (FOV) and slice thickness are often an order of magnitude lower than those employed while imaging humans. This leads to smaller voxel sizes, thus, reducing the SNR particularly in hard to image areas that are more prone to motion or susceptibility artifacts. Higher averages are commonly required, especially *in vivo*, to achieve adequate SNR. For e.g. the acquisition of a 16 x 16 x 2048 spectroscopic grid in the mouse MRSI datasets illustrated in Chapter 3 necessitated at least 4 signal averages to obtain adequate SNR, which resulted in a total scan time of 25 min 36 s with a TR = 1500 ms at 7 T for the fully sampled 1X MRSI dataset. The selected FOV of 27.2 x 27.2 mm^2 and slice thickness of 3 mm resulted in voxels that were 1.7 mm x 1.7 mm x 3 mm. On the other hand, an *in vivo* clinical scan of the adult brain would for e.g. cover a FOV 100 x 100 x 15 mm^3, and for the same 16 x 16 spatial

grid result in voxels that are 6.25 mm x 6.25 mm x 15 mm, ~4X larger than those in small animals. Often a single signal average would suffice to achieve optimal SNR (6 min 24 s with TR = 1500 ms) for e.g. when scanning the brain, although longer scan times may be necessary in SNR limited organs such as the prostate.

Such lengthy scan times are not desirable when imaging animals that are typically anesthetized during the experiment. Particular care also needs to be taken when performing repeated measurements on the same animal at different time points. Furthermore, it is not possible to perform dynamic imaging studies and capture the subtle changes for e.g. in tumor metabolism using such lengthy acquisition protocols. In view of the above, CS accelerated MRSI can help achieve rapid mapping of important biomarkers with high fidelity. The time gained from CS-MRSI can also be utilized to improve detection of the smaller metabolites like 2-hydroxyglutarate (2HG), glycine, alanine, and glutamate, which have proven to be important markers in various malignant tumors [167, 168, 175, 176]. These harder to detect metabolites typically require increased averaging to achieve sufficient SNR, due to their relatively smaller amplitudes as compared to the standard metabolites like choline, creatine and NAA. On the other hand, the improved detection of smaller metabolites that are amenable to spectral editing using an accelerated editing sequence (e.g. the lactate-CS-MRSI sequence) may not require higher averages. This would thus, not offset the time gained from CS-MRSI. The lactate-CS-MRSI sequence can be employed to capture the changes in tumor lactate metabolism in response to an imaging probe or therapy, as demonstrated in Chapter 3.

Preclinical MRI scanners facilitate non-invasive imaging at the molecular and cellular level, which is a critical tool in cancer pharmacology studies. Probing cellular

activity and dysfunction, particularly in cancer metabolism, can aid in the testing and development of new drugs and treatment strategies. Preclinical trials offer greater insights as compared to *in vitro* studies and can help in tumor phenotyping and longitudinal evaluations of disease progression and therapeutic outcomes. Fast data acquisition techniques have the potential to play a pivotal role in realizing the goals of preclinical imaging.

6.2 Clinical CS-MRSI

The clinical applications of CS-MRSI were detailed in Chapters 4 and 5. The retrospective application of CS to MRSI was demonstrated in 20 pediatric patients scanned for various brain related concerns, in Chapter 4. The undersampled reconstructions maintained high fidelity and statistical similarity ($p > 0.05$) with the 1X reference even at 80% undersampling, similar to that seen with the preclinical CS-MRSI datasets. The main limitation of this study was that it was performed retrospectively using the fully sampled 1X MRSI data for each patient. Future work could involve implementing a library of the best pseudo-random undersampling masks corresponding to each acceleration factor on the Philips 3 T Ingenia scanner to enable prospective CS acquisitions. More *in vitro* and *in vivo* clinical applications of CS-MRSI were discussed in Chapter 5, including phantom results from the prospective k-space undersampling implemented on the GE Discovery 3 T MRI scanner. Other aspects involved determining the best pseudo-random undersampling mask tailored to MRSI at each acceleration factor, identifying the acceleration factor at which the reconstruction algorithm failed, and optimization of the CS-MRSI reconstruction algorithm. Future work in these areas

116

would require testing more methods to determine the 'most optimal' mask for CS-MRSI depending on the application/type of dataset along with improving the cost function/functional of the non-linear iterative reconstruction algorithm, to better exploit the CS sparsity criterion.

The primary objective of this thesis was to establish the utility of fast MRSI, in particular CS accelerated MRSI, <u>in order to make a strong case for routine MRSI exams in the clinic.</u> Determination of the most optimal parameters for prospective CS-MRSI and extensive validation of the reconstruction accuracy would give the clinician confidence to exclude the 1X fully sampled MRSI scan. Extension of CS-MRSI to three spatial dimensions would enable one to exploit the sparsity along the slice direction, leading to potentially higher acceleration factors and corresponding reduction in the scan time. However, as previously discussed in Chapter 4, acquisition of 3D fully-sampled MRSI datasets in patients is not possible due to the prohibitive scan time. Prospective 3D CS-MRSI scans can, however be tested in patients if the reconstruction fidelity has been sufficiently validated in human volunteers.

Furthermore, the acquisition of MRSI data involves complicated steps like B_0 shimming and water/lipid suppression, which play a critical role in determining the quality of MRSI data. This would require specialized operator training as in most cases a manual optimization of the above parameters is required to achieve the desired spectral quality. Another aspect to be considered is the implementation of CS reconstruction routines on the scanner for immediate viewing of the spectroscopic data. This is essentially complicated by the fact that a CS reconstruction takes ~ 4 min for a 2D MRSI dataset on a 3 GHz computer (for the 16 x 16 x 2048 datasets illustrated in this thesis),

with larger grid sizes and datasets of higher dimensionality requiring more computation time [72, 78, 93]. Reconstructed MRSI data also requires a series of post-processing operations that need to be applied before presenting the final metabolite maps/spectra for interpretation. Such long processing times are not practical for routine clinical use and would necessitate high speed computing routines that are compatible with the scanner software.

The non-linear iterative CS reconstruction preserves the spectral line shapes but at the same time causes a gradual smoothing of the spectra with increasing acceleration. This is due to the denoising introduced by the wavelet and total variation terms in the functional of the CS reconstruction algorithm. CS denoising could lead to a smoothing of smaller metabolites that are close to the noise floor in the MRS spectrum, thus, presenting the disadvantage of missing these less prominent signals altogether. This dissertation focused on the larger metabolites, namely, NAA, creatine, choline, and lactate, which appear as prominent peaks in the MRS spectrum. However, there are other smaller metabolites such as alanine, glycine, glutamate, 2HG, and myo-inositol that are important biomarkers and relatively hard to detect. In such cases, the reconstruction algorithm would need to be tailored to ensure a reliable representation of low concentration metabolites at higher accelerations, especially when the acquired MRSI data is SNR limited.

In studies involving these smaller metabolites, one could also choose to offset the time gained by employing increased signal averaging to boost the SNR. Future studies could focus on investigating the true sensitivity of metabolite detection as a function of scan time to optimize various parameters in the CS reconstruction algorithm.

118

Furthermore, smaller metabolites that are amenable to spectral editing can be selectively acquired when their detection and quantification is critical. While this approach removes all other metabolite peaks in the spectrum, the biomarker of interest (for e.g. lactate) can be reliably captured with a corresponding gain in time when combined with CS acceleration. This would, however, require the development and implementation of specialized pulse sequences tailored to the metabolite of interest.

6.3 Future Directions: Multi-parametric Assessment of Cancer

Inclusion of MRSI in scan protocols is essential for a true multi-parametric assessment of cancer, on both the clinical and preclinical fronts. The information from various MRI sequences like diffusion weighed imaging (DWI), dynamic contrast enhanced imaging (DCE), and MRSI would enable the clinician to assess different parameters and variations from voxel-to-voxel, leading to potentially improved diagnosis and treatment strategies. The non-invasive extraction of various quantitative parameters like the tumor perfusion, pO_2, apparent diffusion coefficient (ADC), and metabolite concentrations necessitates a multi-modality approach that achieves a differential gain in information from different techniques that probe cancer metabolism. An optimal trade-off between various parameters like the resolution, SNR, sensitivity, penetration depth, artifacts, imaging speed, and costs will facilitate a more comprehensive multi-parametric assessment in cancer targeting and therapeutics.

REFERENCES

[1]   T. R. Brown, B. M. Kincaid, and K. Ugurbil, "NMR chemical shift imaging in three dimensions," *Proc Natl Acad Sci U S A,* vol. 79, pp. 3523-6, Jun 1982.

[2]   A. A. Maudsley, S. K. Hilal, W. H. Perman, and H. E. Simon, "Spatially Resolved High-Resolution Spectroscopy by 4-Dimensional Nmr," *Journal of Magnetic Resonance,* vol. 51, pp. 147-152, 1983.

[3]   A. Skoch, F. Jiru, and J. Bunke, "Spectroscopic imaging: basic principles," *Eur J Radiol,* vol. 67, pp. 230-9, Aug 2008.

[4]   M. van der Graaf, "In vivo magnetic resonance spectroscopy: basic methodology and clinical applications," *Eur Biophys J,* vol. 39, pp. 527-40, Mar 2010.

[5]   J. R. Roebuck, K. M. Cecil, M. D. Schnall, and R. E. Lenkinski, "Human breast lesions: characterization with proton MR spectroscopy," *Radiology,* vol. 209, pp. 269-75, Oct 1998.

[6]   E. O. Aboagye and Z. M. Bhujwalla, "Malignant transformation alters membrane choline phospholipid metabolism of human mammary epithelial cells," *Cancer Res,* vol. 59, pp. 80-4, Jan 1 1999.

[7]   S. J. Nelson, D. B. Vigneron, and W. P. Dillon, "Serial evaluation of patients with brain tumors using volume MRI and 3D 1H MRSI," *NMR Biomed,* vol. 12, pp. 123-38, May 1999.

[8]   J. Kurhanewicz, D. B. Vigneron, and S. J. Nelson, "Three-dimensional magnetic resonance spectroscopic imaging of brain and prostate cancer," *Neoplasia,* vol. 2, pp. 166-89, Jan-Apr 2000.

[9]   P. J. Bolan, S. Meisamy, E. H. Baker, J. Lin, T. Emory, M. Nelson, L. I. Everson, D. Yee, and M. Garwood, "In vivo quantification of choline compounds in the breast with 1H MR spectroscopy," *Magn Reson Med,* vol. 50, pp. 1134-43, Dec 2003.

[10]   H. M. Baik, M. Y. Su, H. Yu, R. Mehta, and O. Nalcioglu, "Quantification of choline-containing compounds in malignant breast tumors by 1H MR spectroscopy using water as an internal reference at 1.5 T," *MAGMA,* vol. 19, pp. 96-104, May 2006.

[11]   A. Shukla-Dave, H. Hricak, C. Moskowitz, N. Ishill, O. Akin, K. Kuroiwa, J. Spector, M. Kumar, V. E. Reuter, J. A. Koutcher, and K. L. Zakian, "Detection of prostate cancer with MR spectroscopic imaging: an expanded paradigm incorporating polyamines," *Radiology,* vol. 245, pp. 499-506, Nov 2007.

[12]   J. M. Duarte, H. Lei, V. Mlynarik, and R. Gruetter, "The neurochemical profile quantified by in vivo 1H NMR spectroscopy," *Neuroimage,* vol. 61, pp. 342-62, Jun 2012.

[13]   E. M. Spur, E. A. Decelle, and L. L. Cheng, "Metabolomic imaging of prostate cancer with magnetic resonance spectroscopy and mass spectrometry," *Eur J Nucl Med Mol Imaging,* vol. 40 Suppl 1, pp. S60-71, Jul 2013.

[14]   T. Kobus, A. J. Wright, T. W. Scheenen, and A. Heerschap, "Mapping of prostate cancer by 1H MRSI," *NMR Biomed,* vol. 27, pp. 39-52, Jan 2014.

[15]   S. J. Nelson, E. Ozhinsky, Y. Li, I. Park, and J. Crane, "Strategies for rapid in vivo 1H and hyperpolarized 13C MR spectroscopic imaging," *J Magn Reson,* vol. 229, pp. 187-97, Apr 2013.

[16]   M. Chmelik, A. I. Schmid, S. Gruber, J. Szendroedi, M. Krssak, S. Trattnig, E. Moser, and M. Roden, "Three-dimensional high-resolution magnetic resonance spectroscopic imaging for absolute quantification of 31P metabolites in human liver," *Magn Reson Med,* vol. 60, pp. 796-802, Oct 2008.

[17]   D. W. Klomp, B. L. van de Bank, A. Raaijmakers, M. A. Korteweg, C. Possanzini, V. O. Boer, C. A. van de Berg, M. A. van de Bosch, and P. R. Luijten, "31P MRSI and 1H MRS at 7 T: initial results in human breast cancer," *NMR Biomed,* vol. 24, pp. 1337-42, Dec 2011.

[18]   E. N. Aguor, C. W. van de Kolk, F. Arslan, M. G. Nederhoff, P. A. Doevendans, G. Pasterkamp, G. J. Strijkers, and C. J. van Echteld, "23Na chemical shift imaging and Gd enhancement of myocardial edema," *Int J Cardiovasc Imaging,* vol. 29, pp. 343-54, Feb 2013.

[19]   P. E. Larson, R. E. Hurd, A. B. Kerr, J. M. Pauly, R. A. Bok, J. Kurhanewicz, and D. B. Vigneron, "Perfusion and diffusion sensitive 13C stimulated-echo MRSI for metabolic imaging of cancer," *Magn Reson Imaging,* vol. 31, pp. 635-42, Jun 2013.

[20]   M. W. Lagemaat, M. C. Maas, E. K. Vos, A. K. Bitz, S. Orzada, E. Weiland, M. J. van Uden, T. Kobus, A. Heerschap, and T. W. Scheenen, "(31) P MR spectroscopic imaging of the human prostate at 7 T: T1 relaxation times, Nuclear Overhauser Effect, and spectral characterization," *Magn Reson Med,* vol. 73, pp. 909-20, Mar 2015.

[21]   N. Salibi and M. A. Brown, *Clinical MR Spectroscopy First Principles*: John Wiley & Sons, Inc., 1998.

[22]   H. Zhu and P. B. Barker, "MR spectroscopy and spectroscopic imaging of the brain," *Methods Mol Biol,* vol. 711, pp. 203-26, 2011.

[23]   A. A. Maudsley, A. Darkazanli, J. R. Alger, L. O. Hall, N. Schuff, C. Studholme, Y. Yu, A. Ebel, A. Frew, D. Goldgof, Y. Gu, R. Pagare, F. Rousseau, K. Sivasankaran, B. J. Soher, P. Weber, K. Young, and X. Zhu, "Comprehensive processing, display and analysis for in vivo MR spectroscopic imaging," *NMR Biomed,* vol. 19, pp. 492-503, Jun 2006.

[24]   R. A. d. Graaf, *In Vivo NMR Spectroscopy: Principles and Techniques*, 2nd ed.: John Wiley & Sons Ltd., 2007.

[25]   D. P. Soares and M. Law, "Magnetic resonance spectroscopy of the brain: review of metabolites and clinical applications," *Clin Radiol,* vol. 64, pp. 12-21, Jan 2009.

[26]   R. N. Al-Okaili, J. Krejza, S. Wang, J. H. Woo, and E. R. Melhem, "Advanced MR imaging techniques in the diagnosis of intraaxial brain tumors in adults," *Radiographics,* vol. 26 Suppl 1, pp. S173-89, Oct 2006.

[27]   M. Dezortova, F. Jiru, J. Petrasek, V. Malinova, J. Zeman, M. Jirsa, and M. Hajek, "1H MR spectroscopy as a diagnostic tool for cerebral creatine deficiency," *MAGMA,* vol. 21, pp. 327-32, Sep 2008.

[28]   P. R. Carroll, F. V. Coakley, and J. Kurhanewicz, "Magnetic resonance imaging and spectroscopy of prostate cancer," *Rev Urol,* vol. 8 Suppl 1, pp. S4-S10, 2006.

[29]   V. Govindaraju, K. Young, and A. A. Maudsley, "Proton NMR chemical shifts and coupling constants for brain metabolites," *NMR Biomed,* vol. 13, pp. 129-53, May 2000.

[30]   J. R. Doherty and J. L. Cleveland, "Targeting lactate metabolism for cancer therapeutics," *J Clin Invest,* vol. 123, pp. 3685-92, Sep 2013.

[31]   W. W. F. Pijnappel, A. Van Den Boogart, R. De Beer, and D. Van Ormondt, "SVD-Based Quantification of Magnetic Resonance Signals," *Journal of Magnetic Resonance,* vol. 97, p. 13, 1992.

[32]   L. Vanhamme, A. van den Boogaart, and S. Van Huffel, "Improved method for accurate and efficient quantification of MRS data with use of prior knowledge," *J Magn Reson,* vol. 129, pp. 35-43, Nov 1997.

[33]   S. Van Huffel, H. Chen, C. Decanniere, and P. Van Hecke, "Algorithm for Time-Domain NMR Data Fitting Based on Total Least Squares," *Journal of Magnetic Resonance, Series A,* vol. 110, p. 10, 1994.

[34]   H. Ratiney, Y. Coenradie, S. Cavassila, D. van Ormondt, and D. Graveron-Demilly, "Time-domain quantitation of 1H short echo-time signals: background accommodation," *MAGMA,* vol. 16, pp. 284-96, May 2004.

[35]   H. Ratiney, M. Sdika, Y. Coenradie, S. Cavassila, D. van Ormondt, and D. Graveron-Demilly, "Time-domain semi-parametric estimation based on a metabolite basis set," *NMR Biomed,* vol. 18, pp. 1-13, Feb 2005.

[36]   J. H. Duyn and C. T. Moonen, "Fast proton spectroscopic imaging of human brain using multiple spin-echoes," *Magn Reson Med,* vol. 30, pp. 409-14, Oct 1993.

[37]   P. B. Barker and D. D. M. Lin, "In vivo proton MR spectroscopy of the human brain," *Progress in Nuclear Magnetic Resonance Spectroscopy,* vol. 49, pp. 99-128, Sep 30 2006.

[38]   D. G. Norris and W. Dreher, "Fast proton spectroscopic imaging using the sliced k-space method," *Magn Reson Med,* vol. 30, pp. 641-5, Nov 1993.

[39]   W. Dreher and D. Leibfritz, "Improved proton spectroscopic U-FLARE imaging for the detection of coupled resonances in the rat brain in vivo," *Magn Reson Imaging,* vol. 17, pp. 611-21, May 1999.

[40]   W. Dreher and D. Leibfritz, "A new method for fast proton spectroscopic imaging: spectroscopic GRASE," *Magn Reson Med,* vol. 44, pp. 668-72, Nov 2000.

[41]   D. G. Norris, "Ultrafast low-angle RARE: U-FLARE," *Magn Reson Med,* vol. 17, pp. 539-42, Feb 1991.

[42]   K. Oshio and D. A. Feinberg, "GRASE (Gradient- and spin-echo) imaging: a novel fast MRI technique," *Magn Reson Med,* vol. 20, pp. 344-9, Aug 1991.

[43]   P. Mansfield, "Spatial mapping of the chemical shift in NMR," *Magn Reson Med,* vol. 1, pp. 370-86, Sep 1984.

[44]   S. Posse, C. DeCarli, and D. Le Bihan, "Three-dimensional echo-planar MR spectroscopic imaging at short echo times in the human brain," *Radiology,* vol. 192, pp. 733-8, Sep 1994.

[45]   S. Posse, G. Tedeschi, R. Risinger, R. Ogg, and D. Le Bihan, "High speed 1H spectroscopic imaging in human brain by echo planar spatial-spectral encoding," *Magn Reson Med,* vol. 33, pp. 34-40, Jan 1995.

[46]   S. Posse, R. Otazo, A. Caprihan, J. Bustillo, H. Chen, P. G. Henry, M. Marjanska, C. Gasparovic, C. Zuo, V. Magnotta, B. Mueller, P. Mullins, P. Renshaw, K. Ugurbil, K. O. Lim, and J. R. Alger, "Proton echo-planar spectroscopic imaging of J-coupled resonances in human brain at 3 and 4 Tesla," *Magn Reson Med,* vol. 58, pp. 236-44, Aug 2007.

[47] A. A. Maudsley, S. K. Hilal, W. H. Perman, and H. E. Simon, "Spatially Resolved High-Resolution Spectroscopy by 4-Dimensional Nmr," *J Magn Reson,* vol. 51, pp. 147-152, 1983.

[48] R. E. Gordon, P. E. Hanley, D. Shaw, D. G. Gadian, G. K. Radda, P. Styles, P. J. Bore, and L. Chan, "Localization of metabolites in animals using 31P topical magnetic resonance," *Nature,* vol. 287, pp. 736-8, Oct 23 1980.

[49] R. Otazo, B. Mueller, K. Ugurbil, L. Wald, and S. Posse, "Signal-to-noise ratio and spectral linewidth improvements between 1.5 and 7 Tesla in proton echo-planar spectroscopic imaging," *Magn Reson Med,* vol. 56, pp. 1200-10, Dec 2006.

[50] R. V. Mulkern and L. P. Panych, "Echo planar spectroscopic imaging," *Concepts in Magnetic Resonance,* vol. 13, pp. 213-237, 2001.

[51] A. Ebel, A. A. Maudsley, M. W. Weiner, and N. Schuff, "Achieving sufficient spectral bandwidth for volumetric 1H echo-planar spectroscopic imaging at 4 Tesla," *Magn Reson Med,* vol. 54, pp. 697-701, Sep 2005.

[52] P. E. Larson, R. Bok, A. B. Kerr, M. Lustig, S. Hu, A. P. Chen, S. J. Nelson, J. M. Pauly, J. Kurhanewicz, and D. B. Vigneron, "Investigation of tumor hyperpolarized [1-13C]-pyruvate dynamics using time-resolved multiband RF excitation echo-planar MRSI," *Magn Reson Med,* vol. 63, pp. 582-91, Mar 2010.

[53] M. Ulrich, T. Wokrina, G. Ende, M. Lang, and P. Bachert, "31P-{1H} echo-planar spectroscopic imaging of the human brain in vivo," *Magn Reson Med,* vol. 57, pp. 784-90, Apr 2007.

[54] E. Adalsteinsson, P. Irarrazabal, S. Topp, C. Meyer, A. Macovski, and D. M. Spielman, "Volumetric spectroscopic imaging with spiral-based k-space trajectories," *Magn Reson Med,* vol. 39, pp. 889-98, Jun 1998.

[55] S. Uribe, A. Guesalaga, R. Mir, M. Guarini, and P. Irarrazaval, "A 3D trajectory for undersampling k-space in MRSI applications," *Magn Reson Imaging,* vol. 25, pp. 350-8, Apr 2007.

[56] C. V. Schirda, C. Tanase, and F. E. Boada, "Rosette spectroscopic imaging: optimal parameters for alias-free, high sensitivity spectroscopic imaging," *J Magn Reson Imaging,* vol. 29, pp. 1375-85, Jun 2009.

[57] M. Seeger, H. Nickisch, R. Pohmann, and B. Scholkopf, "Optimization of k-space trajectories for compressed sensing by Bayesian experimental design," *Magn Reson Med,* vol. 63, pp. 116-26, Jan 2010.

[58] J. K. Furuyama, N. E. Wilson, and M. A. Thomas, "Spectroscopic imaging using concentrically circular echo-planar trajectories in vivo," *Magn Reson Med,* vol. 67, pp. 1515-22, Jun 2012.

[59]   A. A. Maudsley, G. B. Matson, J. W. Hugg, and M. W. Weiner, "Reduced phase encoding in spectroscopic imaging," *Magn Reson Med,* vol. 31, pp. 645-51, Jun 1994.

[60]   S. L. Ponder and D. B. Twieg, "A novel sampling method for 31P spectroscopic imaging with improved sensitivity, resolution, and sidelobe suppression," *J Magn Reson B,* vol. 104, pp. 85-8, May 1994.

[61]   K. P. Pruessmann, M. Weiger, M. B. Scheidegger, and P. Boesiger, "SENSE: sensitivity encoding for fast MRI," *Magn Reson Med,* vol. 42, pp. 952-62, Nov 1999.

[62]   U. Dydak, M. Weiger, K. P. Pruessmann, D. Meier, and P. Boesiger, "Sensitivity-encoded spectroscopic imaging," *Magn Reson Med,* vol. 46, pp. 713-22, Oct 2001.

[63]   M. Blaimer, F. Breuer, M. Mueller, R. M. Heidemann, M. A. Griswold, and P. M. Jakob, "SMASH, SENSE, PILS, GRAPPA: how to choose the optimal method," *Top Magn Reson Imaging,* vol. 15, pp. 223-36, Aug 2004.

[64]   M. A. Griswold, P. M. Jakob, R. M. Heidemann, M. Nittka, V. Jellus, J. Wang, B. Kiefer, and A. Haase, "Generalized autocalibrating partially parallel acquisitions (GRAPPA)," *Magn Reson Med,* vol. 47, pp. 1202-10, Jun 2002.

[65]   F. Breuer, D. Ebel, J. Ruff, M. Blaimer, N. Seiberlich, M. Griswold, and P. Jakob, "Parallel 2D and 3D Spectroscopic Imaging using GRAPPA," in *Proc. Intl. Soc. Mag. Reson. Med.*, 2006.

[66]   R. S. Raghavan, A. Panda, J. Valette, J. R. James, K. Heberlein, U. Boettcher, P. G. Henry, N. Bansal, and U. Dydak, "31P Spectrocopic Imaging with GRAPPA," in *Proc. Intl. Soc. Mag. Reson. Med.*, 2009.

[67]   S. Banerjee, E. Ozturk-Isik, S. J. Nelson, and S. Majumdar, "Elliptical magnetic resonance spectroscopic imaging with GRAPPA for imaging brain tumors at 3 T," *Magn Reson Imaging,* vol. 27, pp. 1319-25, Dec 2009.

[68]   H. Serrai and L. Senhadji, "Acquisition time reduction in magnetic resonance spectroscopic imaging using discrete wavelet encoding," *J Magn Reson,* vol. 177, pp. 22-30, Nov 2005.

[69]   R. Young and H. Serrai, "Implementation of three-dimensional wavelet encoding spectroscopic imaging: in vivo application and method comparison," *Magn Reson Med,* vol. 61, pp. 6-15, Jan 2009.

[70]   M. Lustig, D. Donoho, and J. M. Pauly, "Sparse MRI: The application of compressed sensing for rapid MR imaging," *Magn Reson Med,* vol. 58, pp. 1182-95, Dec 2007.

[71] S. Geethanath, H. M. Baek, S. K. Ganji, Y. Ding, E. A. Maher, R. D. Sims, C. Choi, M. A. Lewis, and V. D. Kodibagkar, "Compressive sensing could accelerate 1H MR metabolic imaging in the clinic," *Radiology,* vol. 262, pp. 985-94, Mar 2012.

[72] P. Cao and E. X. Wu, "Accelerating phase-encoded proton MR spectroscopic imaging by compressed sensing," *J Magn Reson Imaging,* vol. 41, pp. 487-95, Feb 2015.

[73] E. J. Candes, J. Romberg, and T. Tao, "Robust uncertainty principles: Exact signal reconstruction from highly incomplete frequency information," *Ieee Transactions on Information Theory,* vol. 52, pp. 489-509, Feb 2006.

[74] S. Geethanath, R. Reddy, A. S. Konar, S. Imam, R. Sundaresan, R. R. D, and R. Venkatesan, "Compressed sensing MRI: a review," *Crit Rev Biomed Eng,* vol. 41, pp. 183-204, 2013.

[75] J. L. Starck, M. Elad, and D. L. Donoho, "Image decomposition via the combination of sparse representations and a variational approach," *IEEE Trans Image Process,* vol. 14, pp. 1570-82, Oct 2005.

[76] D. S. Taubman and M. W. Marcellin, *JPEG2000 : image compression fundamentals, standards, and practice.* Boston: Kluwer Academic Publishers, 2002.

[77] J. K. Furuyama, N. E. Wilson, B. L. Burns, R. Nagarajan, D. J. Margolis, and M. A. Thomas, "Application of compressed sensing to multidimensional spectroscopic imaging in human prostate," *Magn Reson Med,* vol. 67, pp. 1499-505, Jun 2012.

[78] R. Nagarajan, Z. Iqbal, B. Burns, N. E. Wilson, M. K. Sarma, D. A. Margolis, R. E. Reiter, S. S. Raman, and M. A. Thomas, "Accelerated echo planar J-resolved spectroscopic imaging in prostate cancer: a pilot validation of non-linear reconstruction using total variation and maximum entropy," *NMR Biomed,* Sep 7 2015.

[79] M. K. Sarma, R. Nagarajan, P. M. Macey, R. Kumar, J. P. Villablanca, J. Furuyama, and M. A. Thomas, "Accelerated echo-planar J-resolved spectroscopic imaging in the human brain using compressed sensing: a pilot validation in obstructive sleep apnea," *AJNR Am J Neuroradiol,* vol. 35, pp. S81-9, Jun 2014.

[80] S. Hu, M. Lustig, A. P. Chen, J. Crane, A. Kerr, D. A. Kelley, R. Hurd, J. Kurhanewicz, S. J. Nelson, J. M. Pauly, and D. B. Vigneron, "Compressed sensing for resolution enhancement of hyperpolarized 13C flyback 3D-MRSI," *J Magn Reson,* vol. 192, pp. 258-64, Jun 2008.

[81] S. Hu, M. Lustig, A. Balakrishnan, P. E. Larson, R. Bok, J. Kurhanewicz, S. J. Nelson, A. Goga, J. M. Pauly, and D. B. Vigneron, "3D compressed sensing for highly accelerated hyperpolarized (13)C MRSI with in vivo applications to transgenic mouse models of cancer," *Magn Reson Med,* vol. 63, pp. 312-21, Feb 2010.

[82] P. E. Larson, S. Hu, M. Lustig, A. B. Kerr, S. J. Nelson, J. Kurhanewicz, J. M. Pauly, and D. B. Vigneron, "Fast dynamic 3D MR spectroscopic imaging with compressed sensing and multiband excitation pulses for hyperpolarized 13C studies," *Magn Reson Med,* vol. 65, pp. 610-9, Mar 2011.

[83] N. C. Askin, B. Atis, and E. Ozturk-Isik, "Accelerated phosphorus magnetic resonance spectroscopic imaging using compressed sensing," *Conf Proc IEEE Eng Med Biol Soc,* vol. 2012, pp. 1106-9, 2012.

[84] T. Kampf, A. Fischer, T. C. Basse-Lusebrink, G. Ladewig, F. Breuer, G. Stoll, P. M. Jakob, and W. R. Bauer, "Application of compressed sensing to in vivo 3D (1)(9)F CSI," *J Magn Reson,* vol. 207, pp. 262-73, Dec 2010.

[85] M. L. Maguire, S. Geethanath, C. A. Lygate, V. D. Kodibagkar, and J. E. Schneider, "Compressed sensing to accelerate magnetic resonance spectroscopic imaging: evaluation and application to 23Na-imaging of mouse hearts," *J Cardiovasc Magn Reson,* vol. 17, p. 45, 2015.

[86] F. H. Lin, S. Y. Tsai, R. Otazo, A. Caprihan, L. L. Wald, J. W. Belliveau, and S. Posse, "Sensitivity-encoded (SENSE) proton echo-planar spectroscopic imaging (PEPSI) in the human brain," *Magn Reson Med,* vol. 57, pp. 249-57, Feb 2007.

[87] D. Mayer, D. H. Kim, D. M. Spielman, and R. Bammer, "Fast parallel spiral chemical shift imaging at 3T using iterative SENSE reconstruction," *Magn Reson Med,* vol. 59, pp. 891-7, Apr 2008.

[88] S. Y. Tsai, R. Otazo, S. Posse, Y. R. Lin, H. W. Chung, L. L. Wald, G. C. Wiggins, and F. H. Lin, "Accelerated proton echo planar spectroscopic imaging (PEPSI) using GRAPPA with a 32-channel phased-array coil," *Magn Reson Med,* vol. 59, pp. 989-98, May 2008.

[89] C. Schuster, W. Dreher, J. Stadler, J. Bernarding, and D. Leibfritz, "Fast three-dimensional 1H MR spectroscopic imaging at 7 Tesla using "spectroscopic missing pulse--SSFP"," *Magn Reson Med,* vol. 60, pp. 1243-9, Nov 2008.

[90] M. Gu, C. Liu, and D. M. Spielman, "Parallel spectroscopic imaging reconstruction with arbitrary trajectories using k-space sparse matrices," *Magn Reson Med,* vol. 61, pp. 267-72, Feb 2009.

[91] M. Medved, M. K. Ivancevic, O. I. Olopade, G. M. Newstead, and G. S. Karczmar, "Echo-planar spectroscopic imaging (EPSI) of the water resonance

structure in human breast using sensitivity encoding (SENSE)," *Magn Reson Med,* vol. 63, pp. 1557-63, Jun 2010.

[92] O. C. Andronesi, B. A. Gagoski, and A. G. Sorensen, "Neurologic 3D MR spectroscopic imaging with low-power adiabatic pulses and fast spiral acquisition," *Radiology,* vol. 262, pp. 647-61, Feb 2012.

[93] N. E. Wilson, Z. Iqbal, B. L. Burns, M. Keller, and M. A. Thomas, "Accelerated five-dimensional echo planar J-resolved spectroscopic imaging: Implementation and pilot validation in human brain," *Magn Reson Med,* vol. 75, pp. 42-51, Jan 2016.

[94] F. Hirschhaeuser, U. G. Sattler, and W. Mueller-Klieser, "Lactate: a metabolic key player in cancer," *Cancer Res,* vol. 71, pp. 6921-5, Nov 15 2011.

[95] M. C. Brahimi-Horn, J. Chiche, and J. Pouyssegur, "Hypoxia signalling controls metabolic demand," *Curr Opin Cell Biol,* vol. 19, pp. 223-9, Apr 2007.

[96] M. G. V. Heiden, L. C. Cantley, and C. B. Thompson, "Understanding the Warburg Effect: The Metabolic Requirements of Cell Proliferation," *Science,* vol. 324, pp. 1029-1033, May 22 2009.

[97] G. Schwickert, S. Walenta, K. Sundfor, E. K. Rofstad, and W. Mueller-Klieser, "Correlation of high lactate levels in human cervical cancer with incidence of metastasis," *Cancer Res,* vol. 55, pp. 4757-9, Nov 1 1995.

[98] S. Walenta, A. Salameh, H. Lyng, J. F. Evensen, M. Mitze, E. K. Rofstad, and W. Mueller-Klieser, "Correlation of high lactate levels in head and neck tumors with incidence of metastasis," *Am J Pathol,* vol. 150, pp. 409-15, Feb 1997.

[99] E. O. Aboagye, Z. M. Bhujwalla, Q. He, and J. D. Glickson, "Evaluation of lactate as a 1H nuclear magnetic resonance spectroscopy index for noninvasive prediction and early detection of tumor response to radiation therapy in EMT6 tumors," *Radiat Res,* vol. 150, pp. 38-42, Jul 1998.

[100] S. Walenta, M. Wetterling, M. Lehrke, G. Schwickert, K. Sundfor, E. K. Rofstad, and W. Mueller-Klieser, "High lactate levels predict likelihood of metastases, tumor recurrence, and restricted patient survival in human cervical cancers," *Cancer Res,* vol. 60, pp. 916-21, Feb 15 2000.

[101] V. Quennet, A. Yaromina, D. Zips, A. Rosner, S. Walenta, M. Baumann, and W. Mueller-Klieser, "Tumor lactate content predicts for response to fractionated irradiation of human squamous cell carcinomas in nude mice," *Radiother Oncol,* vol. 81, pp. 130-5, Nov 2006.

[102] U. G. Sattler, S. S. Meyer, V. Quennet, C. Hoerner, H. Knoerzer, C. Fabian, A. Yaromina, D. Zips, S. Walenta, M. Baumann, and W. Mueller-Klieser,

"Glycolytic metabolism and tumour response to fractionated irradiation," *Radiother Oncol,* vol. 94, pp. 102-9, Jan 2010.

[103]   P. F. Daly and J. S. Cohen, "Magnetic resonance spectroscopy of tumors and potential in vivo clinical applications: a review," *Cancer Res,* vol. 49, pp. 770-9, Feb 15 1989.

[104]   R. J. Gillies and D. L. Morse, "In vivo magnetic resonance spectroscopy in cancer," *Annu Rev Biomed Eng,* vol. 7, pp. 287-326, 2005.

[105]   K. Glunde, D. Artemov, M. F. Penet, M. A. Jacobs, and Z. M. Bhujwalla, "Magnetic resonance spectroscopy in metabolic and molecular imaging and diagnosis of cancer," *Chem Rev,* vol. 110, pp. 3043-59, May 12 2010.

[106]   Q. He, D. C. Shungu, P. C. van Zijl, Z. M. Bhujwalla, and J. D. Glickson, "Single-scan in vivo lactate editing with complete lipid and water suppression by selective multiple-quantum-coherence transfer (Sel-MQC) with application to tumors," *J Magn Reson B,* vol. 106, pp. 203-11, Mar 1995.

[107]   S. B. Thakur, J. Yaligar, and J. A. Koutcher, "In vivo lactate signal enhancement using binomial spectral-selective pulses in selective MQ coherence (SS-SelMQC) spectroscopy," *Magn Reson Med,* vol. 62, pp. 591-8, Sep 2009.

[108]   E. A. Mellon, S. C. Lee, S. Pickup, S. Kim, S. C. Goldstein, T. F. Floyd, H. Poptani, E. J. Delikatny, R. Reddy, and J. D. Glickson, "Detection of lactate with a hadamard slice selected, selective multiple quantum coherence, chemical shift imaging sequence (HDMD-SelMQC-CSI) on a clinical MRI scanner: Application to tumors and muscle ischemia," *Magn Reson Med,* vol. 62, pp. 1404-13, Dec 2009.

[109]   J. F. Jansen, W. H. Backes, K. Nicolay, and M. E. Kooi, "1H MR spectroscopy of the brain: absolute quantification of metabolites," *Radiology,* vol. 240, pp. 318-32, Aug 2006.

[110]   D. L. Donoho, "Compressed Sensing," *IEEE Transactions on Information Theory,* vol. 52, p. 18, 2006.

[111]   A. Naressi, C. Couturier, I. Castang, R. de Beer, and D. Graveron-Demilly, "Java-based graphical user interface for MRUI, a software package for quantitation of in vivo/medical magnetic resonance spectroscopy signals," *Comput Biol Med,* vol. 31, pp. 269-86, Jul 2001.

[112]   G. R. Pettit, S. B. Singh, E. Hamel, C. M. Lin, D. S. Alberts, and D. Garcia-Kendall, "Isolation and structure of the strong cell growth and tubulin inhibitor combretastatin A-4," *Experientia,* vol. 45, pp. 209-11, Feb 15 1989.

[113] G. G. Dark, S. A. Hill, V. E. Prise, G. M. Tozer, G. R. Pettit, and D. J. Chaplin, "Combretastatin A-4, an agent that displays potent and selective toxicity toward tumor vasculature," *Cancer Res,* vol. 57, pp. 1829-34, May 15 1997.

[114] M. M. Cooney, J. Ortiz, R. M. Bukowski, and S. C. Remick, "Novel vascular targeting/disrupting agents: combretastatin A4 phosphate and related compounds," *Curr Oncol Rep,* vol. 7, pp. 90-5, Mar 2005.

[115] G. M. Tozer, V. E. Prise, J. Wilson, M. Cemazar, S. Shan, M. W. Dewhirst, P. R. Barber, B. Vojnovic, and D. J. Chaplin, "Mechanisms associated with tumor vascular shut-down induced by combretastatin A-4 phosphate: intravital microscopy and measurement of vascular permeability," *Cancer Res,* vol. 61, pp. 6413-22, Sep 1 2001.

[116] M. Kragh, B. Quistorff, M. R. Horsman, and P. E. Kristjansen, "Acute effects of vascular modifying agents in solid tumors assessed by noninvasive laser Doppler flowmetry and near infrared spectroscopy," *Neoplasia,* vol. 4, pp. 263-7, May-Jun 2002.

[117] H. L. Anderson, J. T. Yap, M. P. Miller, A. Robbins, T. Jones, and P. M. Price, "Assessment of pharmacodynamic vascular response in a phase I trial of combretastatin A4 phosphate," *J Clin Oncol,* vol. 21, pp. 2823-30, Aug 1 2003.

[118] D. Zhao, L. Jiang, E. W. Hahn, and R. P. Mason, "Tumor physiologic response to combretastatin A4 phosphate assessed by MRI," *Int J Radiat Oncol Biol Phys,* vol. 62, pp. 872-80, Jul 1 2005.

[119] Q. S. Ng, V. Goh, D. Carnell, K. Meer, A. R. Padhani, M. I. Saunders, and P. J. Hoskin, "Tumor antivascular effects of radiotherapy combined with combretastatin a4 phosphate in human non-small-cell lung cancer," *Int J Radiat Oncol Biol Phys,* vol. 67, pp. 1375-80, Apr 1 2007.

[120] D. Zhao, E. Richer, P. P. Antich, and R. P. Mason, "Antivascular effects of combretastatin A4 phosphate in breast cancer xenograft assessed using dynamic bioluminescence imaging and confirmed by MRI," *FASEB J,* vol. 22, pp. 2445-51, Jul 2008.

[121] D. Zhao, C. H. Chang, J. G. Kim, H. Liu, and R. P. Mason, "In vivo near-infrared spectroscopy and magnetic resonance imaging monitoring of tumor response to combretastatin A-4-phosphate correlated with therapeutic outcome," *Int J Radiat Oncol Biol Phys,* vol. 80, pp. 574-81, Jun 1 2011.

[122] T. Nielsen, L. Bentzen, M. Pedersen, T. Tramm, P. F. Rijken, J. Bussink, M. R. Horsman, and L. Ostergaard, "Combretastatin A-4 phosphate affects tumor vessel volume and size distribution as assessed using MRI-based vessel size imaging," *Clin Cancer Res,* vol. 18, pp. 6469-77, Dec 1 2012.

[123] L. Liu, R. P. Mason, and B. Gimi, "Dynamic bioluminescence and fluorescence imaging of the effects of the antivascular agent Combretastatin-A4P (CA4P) on brain tumor xenografts," *Cancer Lett,* vol. 356, pp. 462-9, Jan 28 2015.

[124] D. A. Beauregard, S. A. Hill, D. J. Chaplin, and K. M. Brindle, "The susceptibility of tumors to the antivascular drug combretastatin A4 phosphate correlates with vascular permeability," *Cancer Res,* vol. 61, pp. 6811-5, Sep 15 2001.

[125] S. E. Bohndiek, M. I. Kettunen, D. E. Hu, T. H. Witney, B. W. Kennedy, F. A. Gallagher, and K. M. Brindle, "Detection of tumor response to a vascular disrupting agent by hyperpolarized 13C magnetic resonance spectroscopy," *Mol Cancer Ther,* vol. 9, pp. 3278-88, Dec 2010.

[126] G. M. Tozer, C. Kanthou, C. S. Parkins, and S. A. Hill, "The biology of the combretastatins as tumour vascular targeting agents," *Int J Exp Pathol,* vol. 83, pp. 21-38, Feb 2002.

[127] S. J. Bensinger and H. R. Christofk, "New aspects of the Warburg effect in cancer cell biology," *Semin Cell Dev Biol,* vol. 23, pp. 352-61, Jun 2012.

[128] G. J. Kelloff, J. M. Hoffman, B. Johnson, H. I. Scher, B. A. Siegel, E. Y. Cheng, B. D. Cheson, J. O'Shaughnessy, K. Z. Guyton, D. A. Mankoff, L. Shankar, S. M. Larson, C. C. Sigman, R. L. Schilsky, and D. C. Sullivan, "Progress and promise of FDG-PET imaging for cancer patient management and oncologic drug development," *Clin Cancer Res,* vol. 11, pp. 2785-808, Apr 15 2005.

[129] K. Golman, R. in 't Zandt, and M. Thaning, "Real-time metabolic imaging," *Proc Natl Acad Sci U S A,* vol. 103, pp. 11270-5, Jul 25 2006.

[130] K. Golman and J. S. Petersson, "Metabolic imaging and other applications of hyperpolarized 13C1," *Acad Radiol,* vol. 13, pp. 932-42, Aug 2006.

[131] T. B. Rodrigues, E. M. Serrao, B. W. Kennedy, D. E. Hu, M. I. Kettunen, and K. M. Brindle, "Magnetic resonance imaging of tumor glycolysis using hyperpolarized 13C-labeled glucose," *Nat Med,* vol. 20, pp. 93-7, Jan 2014.

[132] J. H. Ardenkjaer-Larsen, B. Fridlund, A. Gram, G. Hansson, L. Hansson, M. H. Lerche, R. Servin, M. Thaning, and K. Golman, "Increase in signal-to-noise ratio of > 10,000 times in liquid-state NMR," *Proc Natl Acad Sci U S A,* vol. 100, pp. 10158-63, Sep 2 2003.

[133] S. J. Nelson, J. Kurhanewicz, D. B. Vigneron, P. E. Larson, A. L. Harzstark, M. Ferrone, M. van Criekinge, J. W. Chang, R. Bok, I. Park, G. Reed, L. Carvajal, E. J. Small, P. Munster, V. K. Weinberg, J. H. Ardenkjaer-Larsen, A. P. Chen, R. E. Hurd, L. I. Odegardstuen, F. J. Robb, J. Tropp, and J. A. Murray, "Metabolic

imaging of patients with prostate cancer using hyperpolarized [1-(1)(3)C]pyruvate," *Sci Transl Med,* vol. 5, p. 198ra108, Aug 14 2013.

[134] B. Madhu, J. C. Waterton, J. R. Griffiths, A. J. Ryan, and S. P. Robinson, "The response of RIF-1 fibrosarcomas to the vascular-disrupting agent ZD6126 assessed by in vivo and ex vivo 1H magnetic resonance spectroscopy," *Neoplasia,* vol. 8, pp. 560-7, Jul 2006.

[135] A. Panigrahy, M. D. Nelson, Jr., and S. Bluml, "Magnetic resonance spectroscopy in pediatric neuroradiology: clinical and research applications," *Pediatr Radiol,* vol. 40, pp. 3-30, Jan 2010.

[136] D. Xu and D. Vigneron, "Magnetic resonance spectroscopy imaging of the newborn brain--a technical review," *Semin Perinatol,* vol. 34, pp. 20-7, Feb 2010.

[137] G. J. Moore, "Proton magnetic resonance spectroscopy in pediatric neuroradiology," *Pediatr Radiol,* vol. 28, pp. 805-14, Nov 1998.

[138] L. G. Astrakas, D. Zurakowski, A. A. Tzika, M. K. Zarifi, D. C. Anthony, U. De Girolami, N. J. Tarbell, and P. M. Black, "Noninvasive magnetic resonance spectroscopic imaging biomarkers to predict the clinical grade of pediatric brain tumors," *Clin Cancer Res,* vol. 10, pp. 8220-8, Dec 15 2004.

[139] A. Laprie, A. Pirzkall, D. A. Haas-Kogan, S. Cha, A. Banerjee, T. P. Le, Y. Lu, S. Nelson, and T. R. McKnight, "Longitudinal multivoxel MR spectroscopy study of pediatric diffuse brainstem gliomas treated with radiotherapy," *Int J Radiat Oncol Biol Phys,* vol. 62, pp. 20-31, May 1 2005.

[140] R. Hourani, A. Horska, S. Albayram, L. J. Brant, E. Melhem, K. J. Cohen, P. C. Burger, J. D. Weingart, B. Carson, M. D. Wharam, and P. B. Barker, "Proton magnetic resonance spectroscopic imaging to differentiate between nonneoplastic lesions and brain tumors in children," *J Magn Reson Imaging,* vol. 23, pp. 99-107, Feb 2006.

[141] S. B. Thakur, S. Karimi, I. J. Dunkel, J. A. Koutcher, and W. Huang, "Longitudinal MR spectroscopic imaging of pediatric diffuse pontine tumors to assess tumor aggression and progression," *AJNR Am J Neuroradiol,* vol. 27, pp. 806-9, Apr 2006.

[142] K. J. Marcus, L. G. Astrakas, D. Zurakowski, M. K. Zarifi, D. Mintzopoulos, T. Y. Poussaint, D. C. Anthony, U. De Girolami, P. M. Black, N. J. Tarbell, and A. A. Tzika, "Predicting survival of children with CNS tumors using proton magnetic resonance spectroscopic imaging biomarkers," *Int J Oncol,* vol. 30, pp. 651-7, Mar 2007.

[143] A. A. Tzika, "Proton magnetic resonance spectroscopic imaging as a cancer biomarker for pediatric brain tumors (Review)," *Int J Oncol,* vol. 32, pp. 517-26, Mar 2008.

[144] O. Gonen, Z. J. Wang, A. K. Viswanathan, P. T. Molloy, and R. A. Zimmerman, "Three-dimensional multivoxel proton MR spectroscopy of the brain in children with neurofibromatosis type 1," *AJNR Am J Neuroradiol,* vol. 20, pp. 1333-41, Aug 1999.

[145] W. E. Wu, Kirov, II, A. Tal, J. S. Babb, S. Milla, J. Oved, H. L. Weiner, O. Devinsky, and O. Gonen, "Brain MR spectroscopic abnormalities in "MRI-negative" tuberous sclerosis complex patients," *Epilepsy Behav,* vol. 27, pp. 319-25, May 2013.

[146] S. P. Rincon, M. B. Blitstein, P. A. Caruso, R. G. Gonzalez, R. L. Thibert, and E. M. Ratai, "The Use of Magnetic Resonance Spectroscopy in the Evaluation of Pediatric Patients With Seizures," *Pediatr Neurol,* vol. 58, pp. 57-66, May 2016.

[147] R. A. Zimmerman and Z. J. Wang, "The value of proton MR spectroscopy in pediatric metabolic brain disease," *AJNR Am J Neuroradiol,* vol. 18, pp. 1872-9, Nov-Dec 1997.

[148] D. H. Kim, M. Gu, C. Cunningham, A. Chen, F. Baumer, O. A. Glenn, D. B. Vigneron, D. M. Spielman, and A. J. Barkovich, "Fast 3D (1)H MRSI of the corticospinal tract in pediatric brain," *J Magn Reson Imaging,* vol. 29, pp. 1-6, Jan 2009.

[149] S. S. Vasanawala, M. T. Alley, B. A. Hargreaves, R. A. Barth, J. M. Pauly, and M. Lustig, "Improved pediatric MR imaging with compressed sensing," *Radiology,* vol. 256, pp. 607-16, Aug 2010.

[150] A. Hsiao, M. Lustig, M. T. Alley, M. Murphy, F. P. Chan, R. J. Herfkens, and S. S. Vasanawala, "Rapid pediatric cardiac assessment of flow and ventricular volume with compressed sensing parallel imaging volumetric cine phase-contrast MRI," *AJR Am J Roentgenol,* vol. 198, pp. W250-9, Mar 2012.

[151] T. Zhang, S. Chowdhury, M. Lustig, R. A. Barth, M. T. Alley, T. Grafendorfer, P. D. Calderon, F. J. Robb, J. M. Pauly, and S. S. Vasanawala, "Clinical performance of contrast enhanced abdominal pediatric MRI with fast combined parallel imaging compressed sensing reconstruction," *J Magn Reson Imaging,* vol. 40, pp. 13-25, Jul 2014.

[152] T. Zhang, J. Y. Cheng, A. G. Potnick, R. A. Barth, M. T. Alley, M. Uecker, M. Lustig, J. M. Pauly, and S. S. Vasanawala, "Fast pediatric 3D free-breathing abdominal dynamic contrast enhanced MRI with high spatiotemporal resolution," *J Magn Reson Imaging,* vol. 41, pp. 460-73, Feb 2015.

[153] J. Y. Cheng, T. Zhang, N. Ruangwattanapaisarn, M. T. Alley, M. Uecker, J. M. Pauly, M. Lustig, and S. S. Vasanawala, "Free-breathing pediatric MRI with nonrigid motion correction and acceleration," *J Magn Reson Imaging,* vol. 42, pp. 407-20, Aug 2015.

[154] Q. T. Ostrom, H. Gittleman, P. Farah, A. Ondracek, Y. Chen, Y. Wolinsky, N. E. Stroup, C. Kruchko, and J. S. Barnholtz-Sloan, "CBTRUS statistical report: Primary brain and central nervous system tumors diagnosed in the United States in 2006-2010," *Neuro Oncol,* vol. 15 Suppl 2, pp. ii1-56, Nov 2013.

[155] F. Knoll, C. Clason, C. Diwoky, and R. Stollberger, "Adapted random sampling patterns for accelerated MRI," *MAGMA,* vol. 24, pp. 43-50, Feb 2011.

[156] F. Zijlstra, M. A. Viergever, and P. R. Seevinck, "Evaluation of Variable Density and Data-Driven K-Space Undersampling for Compressed Sensing Magnetic Resonance Imaging," *Invest Radiol,* Dec 15 2015.

[157] A. Lin, B. D. Ross, K. Harris, and W. Wong, "Efficacy of proton magnetic resonance spectroscopy in neurological diagnosis and neurotherapeutic decision making," *NeuroRx,* vol. 2, pp. 197-214, Apr 2005.

[158] R. A. Moats and T. Shonk, "Evaluation of automated MR spectroscopy: application in Alzheimer disease," *AJNR Am J Neuroradiol,* vol. 16, pp. 1779-82, Oct 1995.

[159] F. Gao and P. B. Barker, "Various MRS application tools for Alzheimer disease and mild cognitive impairment," *AJNR Am J Neuroradiol,* vol. 35, pp. S4-11, Jun 2014.

[160] S. N. Breiter, S. Arroyo, V. P. Mathews, R. P. Lesser, R. N. Bryan, and P. B. Barker, "Proton MR spectroscopy in patients with seizure disorders," *AJNR Am J Neuroradiol,* vol. 15, pp. 373-84, Feb 1994.

[161] M. Castillo, J. K. Smith, and L. Kwock, "Proton MR spectroscopy in patients with acute temporal lobe seizures," *AJNR Am J Neuroradiol,* vol. 22, pp. 152-7, Jan 2001.

[162] D. E. Saunders, "MR spectroscopy in stroke," *Br Med Bull,* vol. 56, pp. 334-45, 2000.

[163] R. Hourani, L. J. Brant, T. Rizk, J. D. Weingart, P. B. Barker, and A. Horska, "Can proton MR spectroscopic and perfusion imaging differentiate between neoplastic and nonneoplastic brain lesions in adults?," *AJNR Am J Neuroradiol,* vol. 29, pp. 366-72, Feb 2008.

[164] M. Law, S. Yang, H. Wang, J. S. Babb, G. Johnson, S. Cha, E. A. Knopp, and D. Zagzag, "Glioma grading: sensitivity, specificity, and predictive values of

perfusion MR imaging and proton MR spectroscopic imaging compared with conventional MR imaging," *AJNR Am J Neuroradiol,* vol. 24, pp. 1989-98, Nov-Dec 2003.

[165] G. Oz, J. R. Alger, P. B. Barker, R. Bartha, A. Bizzi, C. Boesch, P. J. Bolan, K. M. Brindle, C. Cudalbu, A. Dincer, U. Dydak, U. E. Emir, J. Frahm, R. G. Gonzalez, S. Gruber, R. Gruetter, R. K. Gupta, A. Heerschap, A. Henning, H. P. Hetherington, F. A. Howe, P. S. Huppi, R. E. Hurd, K. Kantarci, D. W. Klomp, R. Kreis, M. J. Kruiskamp, M. O. Leach, A. P. Lin, P. R. Luijten, M. Marjanska, A. A. Maudsley, D. J. Meyerhoff, C. E. Mountford, S. J. Nelson, M. N. Pamir, J. W. Pan, A. C. Peet, H. Poptani, S. Posse, P. J. Pouwels, E. M. Ratai, B. D. Ross, T. W. Scheenen, C. Schuster, I. C. Smith, B. J. Soher, I. Tkac, D. B. Vigneron, and R. A. Kauppinen, "Clinical proton MR spectroscopy in central nervous system disorders," *Radiology,* vol. 270, pp. 658-79, Mar 2014.

[166] O. C. Andronesi, G. S. Kim, E. Gerstner, T. Batchelor, A. A. Tzika, V. R. Fantin, M. G. Vander Heiden, and A. G. Sorensen, "Detection of 2-hydroxyglutarate in IDH-mutated glioma patients by in vivo spectral-editing and 2D correlation magnetic resonance spectroscopy," *Sci Transl Med,* vol. 4, p. 116ra4, Jan 11 2012.

[167] S. K. Ganji, Z. An, V. Tiwari, S. McNeil, M. C. Pinho, E. Pan, B. E. Mickey, E. A. Maher, and C. Choi, "In vivo detection of 2-hydroxyglutarate in brain tumors by optimized point-resolved spectroscopy (PRESS) at 7T," *Magn Reson Med,* Mar 16 2016.

[168] S. K. Ganji, E. A. Maher, and C. Choi, "In vivo (1)H MRSI of glycine in brain tumors at 3T," *Magn Reson Med,* vol. 75, pp. 52-62, Jan 2016.

[169] A. D. Harris, N. A. Puts, P. B. Barker, and R. A. Edden, "Spectral-editing measurements of GABA in the human brain with and without macromolecule suppression," *Magn Reson Med,* vol. 74, pp. 1523-9, Dec 2015.

[170] H. K. Lee, A. Yaman, and O. Nalcioglu, "Homonuclear J-refocused spectral editing technique for quantification of glutamine and glutamate by 1H NMR spectroscopy," *Magn Reson Med,* vol. 34, pp. 253-9, Aug 1995.

[171] J. Shen, J. Yang, I. Y. Choi, S. S. Li, and Z. Chen, "A new strategy for in vivo spectral editing. Application to GABA editing using selective homonuclear polarization transfer spectroscopy," *J Magn Reson,* vol. 170, pp. 290-8, Oct 2004.

[172] D. D. Liu, D. Liang, X. Liu, and Y. T. Zhang, "Under-sampling trajectory design for compressed sensing MRI," *Conf Proc IEEE Eng Med Biol Soc,* vol. 2012, pp. 73-6, 2012.

[173] S. Ravishankar and Y. Bresler, "Adaptive sampling design for compressed sensing MRI," *Conf Proc IEEE Eng Med Biol Soc,* vol. 2011, pp. 3751-5, 2011.

[174]   S. Geethanath, P. K. Gulaka, and V. D. Kodibagkar, "Acceleration of conventional data acquisition in dynamic contrast enhancement: comparing keyhole approaches with compressive sensing," *Crit Rev Biomed Eng,* vol. 42, pp. 437-50, 2014.

[175]   F. A. Howe, S. J. Barton, S. A. Cudlip, M. Stubbs, D. E. Saunders, M. Murphy, P. Wilkins, K. S. Opstad, V. L. Doyle, M. A. McLean, B. A. Bell, and J. R. Griffiths, "Metabolic profiles of human brain tumors using quantitative in vivo 1H magnetic resonance spectroscopy," *Magn Reson Med,* vol. 49, pp. 223-32, Feb 2003.

[176]   Y. Kinoshita and A. Yokota, "Absolute concentrations of metabolites in human brain tumors using in vitro proton magnetic resonance spectroscopy," *NMR Biomed,* vol. 10, pp. 2-12, Jan 1997.

[177]   C. Beynon, K. L. Kiening, B. Orakcioglu, A. W. Unterberg, and O. W. Sakowitz, "Brain tissue oxygen monitoring and hyperoxic treatment in patients with traumatic brain injury," *J Neurotrauma,* vol. 29, pp. 2109-23, Aug 10 2012.

[178]   P. K. Narotam, J. F. Morrison, and N. Nathoo, "Brain tissue oxygen monitoring in traumatic brain injury and major trauma: outcome analysis of a brain tissue oxygen-directed therapy," *J Neurosurg,* vol. 111, pp. 672-82, Oct 2009.

[179]   J. Nortje and A. K. Gupta, "The role of tissue oxygen monitoring in patients with acute brain injury," *Br J Anaesth,* vol. 97, pp. 95-106, Jul 2006.

[180]   B. B. Allen, C. E. Hoffman, C. S. Traube, S. L. Weinstein, and J. P. Greenfield, "Continuous brain tissue oxygenation monitoring in the management of pediatric stroke," *Neurocrit Care,* vol. 15, pp. 529-36, Dec 2011.

[181]   F. Moreau, R. Yang, V. Nambiar, A. M. Demchuk, and J. F. Dunn, "Near-infrared measurements of brain oxygenation in stroke," *Neurophotonics,* vol. 3, p. 031403, Jul 2016.

[182]   H. Hou, O. Grinberg, B. Williams, S. Grinberg, H. Yu, D. L. Alvarenga, H. Wallach, J. Buckey, and H. M. Swartz, "The effect of oxygen therapy on brain damage and cerebral pO(2) in transient focal cerebral ischemia in the rat," *Physiol Meas,* vol. 28, pp. 963-76, Aug 2007.

[183]   H. Hou, O. Y. Grinberg, S. A. Grinberg, E. Demidenko, and H. M. Swartz, "Cerebral tissue oxygenation in reversible focal ischemia in rats: multi-site EPR oximetry measurements," *Physiol Meas,* vol. 26, pp. 131-41, Feb 2005.

[184]   N. Khan, H. Hou, C. J. Eskey, K. Moodie, S. Gohain, G. Du, S. Hodge, W. C. Culp, P. Kuppusamy, and H. M. Swartz, "Deep-tissue oxygen monitoring in the brain of rabbits for stroke research," *Stroke,* vol. 46, pp. e62-6, Mar 2015.

[185] N. Khan, H. Hou, H. M. Swartz, and P. Kuppusamy, "Direct and Repeated Measurement of Heart and Brain Oxygenation Using In Vivo EPR Oximetry," *Methods Enzymol,* vol. 564, pp. 529-52, 2015.

[186] K. J. Liu, G. Bacic, P. J. Hoopes, J. Jiang, H. Du, L. C. Ou, J. F. Dunn, and H. M. Swartz, "Assessment of cerebral pO2 by EPR oximetry in rodents: effects of anesthesia, ischemia, and breathing gas," *Brain Res,* vol. 685, pp. 91-8, Jul 10 1995.

[187] C. E. Fife, D. R. Smart, P. J. Sheffield, H. W. Hopf, G. Hawkins, and D. Clarke, "Transcutaneous oximetry in clinical practice: consensus statements from an expert panel based on evidence," *Undersea Hyperb Med,* vol. 36, pp. 43-53, Jan-Feb 2009.

[188] E. T. Ahrens and J. W. Bulte, "Tracking immune cells in vivo using magnetic resonance imaging," *Nat Rev Immunol,* vol. 13, pp. 755-63, Oct 2013.

[189] D. K. Kadayakkara, J. M. Janjic, L. K. Pusateri, W. B. Young, and E. T. Ahrens, "In vivo observation of intracellular oximetry in perfluorocarbon-labeled glioma cells and chemotherapeutic response in the CNS using fluorine-19 MRI," *Magn Reson Med,* vol. 64, pp. 1252-9, Nov 2010.

[190] J. U. Menon, P. K. Gulaka, M. A. McKay, S. Geethanath, L. Liu, and V. D. Kodibagkar, "Dual-modality, dual-functional nanoprobes for cellular and molecular imaging," *Theranostics,* vol. 2, pp. 1199-207, 2012.

[191] C. P. Addington, A. Cusick, R. V. Shankar, S. Agarwal, S. E. Stabenfeldt, and V. D. Kodibagkar, "Siloxane Nanoprobes for Labeling and Dual Modality Functional Imaging of Neural Stem Cells," *Ann Biomed Eng,* vol. 44, pp. 816-27, Mar 2016.

[192] P. Boehm-Sturm, L. Mengler, S. Wecker, M. Hoehn, and T. Kallur, "In vivo tracking of human neural stem cells with 19F magnetic resonance imaging," *PLoS One,* vol. 6, p. e29040, 2011.

[193] J. J. Wan, M. J. Cohen, G. Rosenthal, I. K. Haitsma, D. J. Morabito, N. Derugin, M. M. Knudson, and G. T. Manley, "Refining resuscitation strategies using tissue oxygen and perfusion monitoring in critical organ beds," *J Trauma,* vol. 66, pp. 353-7, Feb 2009.

[194] C. Diepart, J. Magat, B. F. Jordan, and B. Gallez, "In vivo mapping of tumor oxygen consumption using (19)F MRI relaxometry," *NMR Biomed,* vol. 24, pp. 458-63, Jun 2011.

[195] S. Hunjan, D. Zhao, A. Constantinescu, E. W. Hahn, P. P. Antich, and R. P. Mason, "Tumor oximetry: demonstration of an enhanced dynamic mapping procedure using fluorine-19 echo planar magnetic resonance imaging in the

Dunning prostate R3327-AT1 rat tumor," *Int J Radiat Oncol Biol Phys,* vol. 49, pp. 1097-108, Mar 15 2001.

[196] B. F. Jordan, G. O. Cron, and B. Gallez, "Rapid monitoring of oxygenation by 19F magnetic resonance imaging: Simultaneous comparison with fluorescence quenching," *Magn Reson Med,* vol. 61, pp. 634-8, Mar 2009.

[197] M. Hockel and P. Vaupel, "Tumor hypoxia: definitions and current clinical, biologic, and molecular aspects," *J Natl Cancer Inst,* vol. 93, pp. 266-76, Feb 21 2001.

[198] W. R. Wilson and M. P. Hay, "Targeting hypoxia in cancer therapy," *Nat Rev Cancer,* vol. 11, pp. 393-410, Jun 2011.

[199] J. L. Tatum, G. J. Kelloff, R. J. Gillies, J. M. Arbeit, J. M. Brown, K. S. Chao, J. D. Chapman, W. C. Eckelman, A. W. Fyles, A. J. Giaccia, R. P. Hill, C. J. Koch, M. C. Krishna, K. A. Krohn, J. S. Lewis, R. P. Mason, G. Melillo, A. R. Padhani, G. Powis, J. G. Rajendran, R. Reba, S. P. Robinson, G. L. Semenza, H. M. Swartz, P. Vaupel, D. Yang, B. Croft, J. Hoffman, G. Liu, H. Stone, and D. Sullivan, "Hypoxia: importance in tumor biology, noninvasive measurement by imaging, and value of its measurement in the management of cancer therapy," *Int J Radiat Biol,* vol. 82, pp. 699-757, Oct 2006.

[200] S. M. Evans, K. D. Judy, I. Dunphy, W. T. Jenkins, P. T. Nelson, R. Collins, E. P. Wileyto, K. Jenkins, S. M. Hahn, C. W. Stevens, A. R. Judkins, P. Phillips, B. Geoerger, and C. J. Koch, "Comparative measurements of hypoxia in human brain tumors using needle electrodes and EF5 binding," *Cancer Res,* vol. 64, pp. 1886-92, Mar 1 2004.

[201] B. Movsas, J. D. Chapman, A. L. Hanlon, E. M. Horwitz, R. E. Greenberg, C. Stobbe, G. E. Hanks, and A. Pollack, "Hypoxic prostate/muscle pO2 ratio predicts for biochemical failure in patients with prostate cancer: preliminary findings," *Urology,* vol. 60, pp. 634-9, Oct 2002.

[202] P. Vaupel, K. Schlenger, C. Knoop, and M. Hockel, "Oxygenation of human tumors: evaluation of tissue oxygen distribution in breast cancers by computerized O2 tension measurements," *Cancer Res,* vol. 51, pp. 3316-22, Jun 15 1991.

[203] V. A. Bourke, D. Zhao, J. Gilio, C. H. Chang, L. Jiang, E. W. Hahn, and R. P. Mason, "Correlation of radiation response with tumor oxygenation in the Dunning prostate R3327-AT1 tumor," *Int J Radiat Oncol Biol Phys,* vol. 67, pp. 1179-86, Mar 15 2007.

[204] J. A. O'Hara, F. Goda, E. Demidenko, and H. M. Swartz, "Effect on regrowth delay in a murine tumor of scheduling split-dose irradiation based on direct pO2 measurements by electron paramagnetic resonance oximetry," *Radiat Res,* vol. 150, pp. 549-56, Nov 1998.

[205] D. Zhao, A. Constantinescu, C. H. Chang, E. W. Hahn, and R. P. Mason, "Correlation of tumor oxygen dynamics with radiation response of the dunning prostate R3327-HI tumor," *Radiat Res,* vol. 159, pp. 621-31, May 2003.

[206] J. M. Brown, "The hypoxic cell: a target for selective cancer therapy--eighteenth Bruce F. Cain Memorial Award lecture," *Cancer Res,* vol. 59, pp. 5863-70, Dec 1 1999.

[207] J. D. Chapman, C. C. Stobbe, M. R. Arnfield, R. Santus, J. Lee, and M. S. McPhee, "Oxygen dependency of tumor cell killing in vitro by light-activated Photofrin II," *Radiat Res,* vol. 126, pp. 73-9, Apr 1991.

[208] V. D. Kodibagkar, X. Wang, J. Pacheco-Torres, P. Gulaka, and R. P. Mason, "Proton imaging of siloxanes to map tissue oxygenation levels (PISTOL): a tool for quantitative tissue oximetry," *NMR Biomed,* vol. 21, pp. 899-907, Oct 2008.

[209] V. D. Kodibagkar, W. Cui, M. E. Merritt, and R. P. Mason, "Novel 1H NMR approach to quantitative tissue oximetry using hexamethyldisiloxane," *Magn Reson Med,* vol. 55, pp. 743-8, Apr 2006.

[210] P. K. Gulaka, U. Rastogi, M. A. McKay, X. Wang, R. P. Mason, and V. D. Kodibagkar, "Hexamethyldisiloxane-based nanoprobes for (1) H MRI oximetry," *NMR Biomed,* vol. 24, pp. 1226-34, Dec 2011.

[211] P. Gowland and P. Mansfield, "Accurate measurement of T1 in vivo in less than 3 seconds using echo-planar imaging," *Magn Reson Med,* vol. 30, pp. 351-4, Sep 1993.

[212] D. C. Look and D. R. Locker, "Time Saving in Measurement of NMR and EPR Relaxation Times," *The Review of Scientific Instruments,* vol. 41, p. 2, 1970.

[213] K. H. Chuang and A. Koretsky, "Improved neuronal tract tracing using manganese enhanced magnetic resonance imaging with fast T(1) mapping," *Magn Reson Med,* vol. 55, pp. 604-11, Mar 2006.

[214] R. Deichmann and A. Haase, "Quantification of T1 Values by Snapshot-Flash Nmr Imaging," *Journal of Magnetic Resonance,* vol. 96, pp. 608-612, Feb 15 1992.

[215] P. K. Gulaka, and Kodibagkar, V. D., "New bullets for PISTOL: linear and cyclic reporter molecules for 1H MR oximetry," *Proceedings of the International Society for Magnetic Resonance in Medicine,* vol. 18, p. 1, 2010.

[216] P. K. Gulaka, F. Rojas-Quijano, Z. Kovacs, R. P. Mason, A. D. Sherry, and V. D. Kodibagkar, "GdDO3NI, a nitroimidazole-based T1 MRI contrast agent for imaging tumor hypoxia in vivo," *J Biol Inorg Chem,* vol. 19, pp. 271-9, Feb 2014.

[217] F. A. Rojas-Quijano, G. Tircso, E. Tircsone Benyo, Z. Baranyai, H. Tran Hoang, F. K. Kalman, P. K. Gulaka, V. D. Kodibagkar, S. Aime, Z. Kovacs, and A. D. Sherry, "Synthesis and characterization of a hypoxia-sensitive MRI probe," *Chemistry,* vol. 18, pp. 9669-76, Jul 27 2012.

[218] S. Liu, S. J. Shah, L. J. Wilmes, J. Feiner, V. D. Kodibagkar, M. F. Wendland, R. P. Mason, N. Hylton, H. W. Hopf, and M. D. Rollins, "Quantitative tissue oxygen measurement in multiple organs using 19F MRI in a rat model," *Magn Reson Med,* vol. 66, pp. 1722-30, Dec 2011.

[219] S. P. Robinson and J. R. Griffiths, "Current issues in the utility of 19F nuclear magnetic resonance methodologies for the assessment of tumour hypoxia," *Philos Trans R Soc Lond B Biol Sci,* vol. 359, pp. 987-96, Jun 29 2004.

[220] M. Xia, V. Kodibagkar, H. Liu, and R. P. Mason, "Tumour oxygen dynamics measured simultaneously by near-infrared spectroscopy and 19F magnetic resonance imaging in rats," *Phys Med Biol,* vol. 51, pp. 45-60, Jan 7 2006.

[221] D. Zhao, L. Jiang, E. W. Hahn, and R. P. Mason, "Comparison of 1H blood oxygen level-dependent (BOLD) and 19F MRI to investigate tumor oxygenation," *Magn Reson Med,* vol. 62, pp. 357-64, Aug 2009.

[222] H. Zhou, R. R. Hallac, R. Lopez, R. Denney, M. T. MacDonough, L. Li, L. Liu, E. E. Graves, M. L. Trawick, K. G. Pinney, and R. P. Mason, "Evaluation of tumor ischemia in response to an indole-based vascular disrupting agent using BLI and (19)F MRI," *Am J Nucl Med Mol Imaging,* vol. 5, pp. 143-53, 2015.

[223] D. Zhao, A. Constantinescu, E. W. Hahn, and R. P. Mason, "Tumor oxygen dynamics with respect to growth and respiratory challenge: investigation of the Dunning prostate R3327-HI tumor," *Radiat Res,* vol. 156, pp. 510-20, Nov 2001.

[224] R. P. Mason, W. Rodbumrung, and P. P. Antich, "Hexafluorobenzene: a sensitive 19F NMR indicator of tumor oxygenation," *NMR Biomed,* vol. 9, pp. 125-34, May 1996.

[225] T. K. Hitchens, Q. Ye, D. F. Eytan, J. M. Janjic, E. T. Ahrens, and C. Ho, "19F MRI detection of acute allograft rejection with in vivo perfluorocarbon labeling of immune cells," *Magn Reson Med,* vol. 65, pp. 1144-53, Apr 2011.

[226] K. C. Partlow, J. Chen, J. A. Brant, A. M. Neubauer, T. E. Meyerrose, M. H. Creer, J. A. Nolta, S. D. Caruthers, G. M. Lanza, and S. A. Wickline, "19F magnetic resonance imaging for stem/progenitor cell tracking with multiple unique perfluorocarbon nanobeacons," *FASEB J,* vol. 21, pp. 1647-54, Jun 2007.

[227] M. Srinivas, A. Heerschap, E. T. Ahrens, C. G. Figdor, and I. J. de Vries, "(19)F MRI for quantitative in vivo cell tracking," *Trends Biotechnol,* vol. 28, pp. 363-70, Jul 2010.

[228] S. Temme, F. Bonner, J. Schrader, and U. Flogel, "19F magnetic resonance imaging of endogenous macrophages in inflammation," *Wiley Interdiscip Rev Nanomed Nanobiotechnol,* vol. 4, pp. 329-43, May-Jun 2012.

[229] M. Modo, K. Mellodew, D. Cash, S. E. Fraser, T. J. Meade, J. Price, and S. C. Williams, "Mapping transplanted stem cell migration after a stroke: a serial, in vivo magnetic resonance imaging study," *Neuroimage,* vol. 21, pp. 311-7, Jan 2004.

APPENDIX A

A FASTER PISTOL FOR ^{1}H MR-BASED QUANTITATIVE TISSUE OXIMETRY

This section is based on the paper – "A Faster PISTOL for ^{1}H MR-based quantitative tissue oximetry", R. Vidya Shankar and V. D. Kodibagkar, in submission to *NMR in Biomedicine*.

A.1 Introduction

The normal functioning of various tissues and organs in the human body is dependent on the efficient delivery of oxygen. Tissue oximetry techniques are increasingly playing an important role in the assessment and monitoring of various pathologies such as in traumatic brain injury [177-179], ischemic stroke [180-186], wound healing [187], in cellular tracking and imaging the health of labeled cells [188-192], resuscitation approaches in critical organ beds [193], and for monitoring oxygen dynamics in cancer [194-196]. Numerous factors can cause tissue to develop hypoxic (low oxygen tension, pO_2) regions such as impaired perfusion, breakdown in diffusion processes, reduced oxygen transport functionality of blood in conditions like anemia, increased cellular cytotoxicity, and low blood oxygen tension commonly seen in pulmonary diseases [197, 198]. Solid tumors tend to have hypoxic foci that contribute to malignant progression and poor therapeutic response [199]. Histological studies have revealed extensive hypoxic regions in various tumors of the brain, breast, and prostate [200-202], with very high resistance to radiotherapy identified in severely hypoxic tumors [203-205]. The mapping of tissue pO_2 *in vivo* may be critical in furthering investigations of the mechanisms that underlie tissue function, particularly in predicting therapeutic outcomes for individual patients as well as in the design of efficacious therapeutic combinations [206, 207]. Furthermore, fast routine tissue oxygenation

143

measurements in individual organs will enable the clinician to evaluate and prescribe defined endpoints for medical interventions, along with an optimized use of hyperoxic oxygen in various medical therapies.

PISTOL (Proton Imaging of Siloxanes to map Tissue Oxygenation Levels) is a recently developed oximetry technique in proton MRI that is based on the relaxometry of siloxanes such as hexamethyldisiloxane (HMDSO) [208]. HMDSO has been identified as a promising ^{1}H pO_2 reporter molecule as its spin-lattice relaxation rate R_1 tends to exhibit a linear dependence on the pO_2, particularly in the temperature range $26 - 46$ ^{o}C [209]. The PISTOL sequence has been designed to selectively excite and map the T_1 of the siloxane ^{1}H resonance (~ 0 ppm), while simultaneously suppressing the peaks from water and fat. One can subsequently use PISTOL to map the tissue pO_2 at various locations where siloxanes (neat or emulsified) have been exogenously administered or accumulated after endogenous administration. This sequence can also be used to record the dynamic changes in the tissue pO_2 in response to intervention [208, 210] or for imaging and oximetry of siloxane labelled cells [190, 191].

The PISTOL sequence requires 3 minutes 45 seconds to map the T_1, and hence pO_2, of exogenously administered HMDSO at 7 T. A faster oximetry sequence could be particularly useful in studies where dynamic changes in the tissue pO_2 need to be rapidly recorded in response to gas intervention. Hence the primary objective of this study was to develop a faster siloxane-selective relaxometry sequence and to compare it, *in vitro* and *in vivo*, with the PISTOL sequence using metrics such as the total imaging time and fidelity of the acquired relaxometry data.

A.2 Materials and Methods

PISTOL-LL Pulse Sequence for pO₂ measurement

A new oximetry sequence, henceforth referred to as PISTOL-LL (Figure A.1), was developed by modifying the PISTOL pulse sequence [208] where the ARDVARC magnetization preparation scheme was replaced by a frequency-selective version of the Look-Locker [211, 212] approach. The PISTOL-LL sequence, depicted in Figure A.1, consists of a frequency-selective π inversion recovery preparation pulse, followed by a sequence of 55 low flip-angle α^o pulses, with a delay τ between two successive pulses. The small flip angle α pulses are also frequency selective for the HMDSO resonance. Each α pulse is immediately followed by an EPI readout/module, thus, enabling multiple (in this case 55) image acquisitions within the same TR. An excitation angle of $\alpha = 5^o$ was employed. The magnetization recovery curve was sampled linearly using 55 equally spaced α^o pulses, with the spacing between two subsequent α^o pulses being $\tau = 1000$ ms (TR = 55 s). Thus, the PISTOL-LL sequence enabled T_1 mapping of HMDSO in ~55s.

For the PISTOL acquisitions, the T_1 measurements were obtained using the ARDVARC (alternating relaxation delays with variable acquisitions for reduction of clearance effects) protocol, as employed previously [208]. The total scan time for each T_1 map acquired using PISTOL was 3 minutes 45 seconds. PISTOL and PISTOL-LL were implemented on a horizontal-bore Bruker BioSpec® 7 T preclinical MRI scanner with actively shielded gradients and all *in vitro* and *in vivo* experiments were conducted on this scanner. An HMDSO-selective chemical-shift selective spin-echo sequence was initially used to locate the HMDSO resonance. Both PISTOL and PISTOL-LL were subsequently run to measure the T_1 of HMDSO at the chosen slice location.
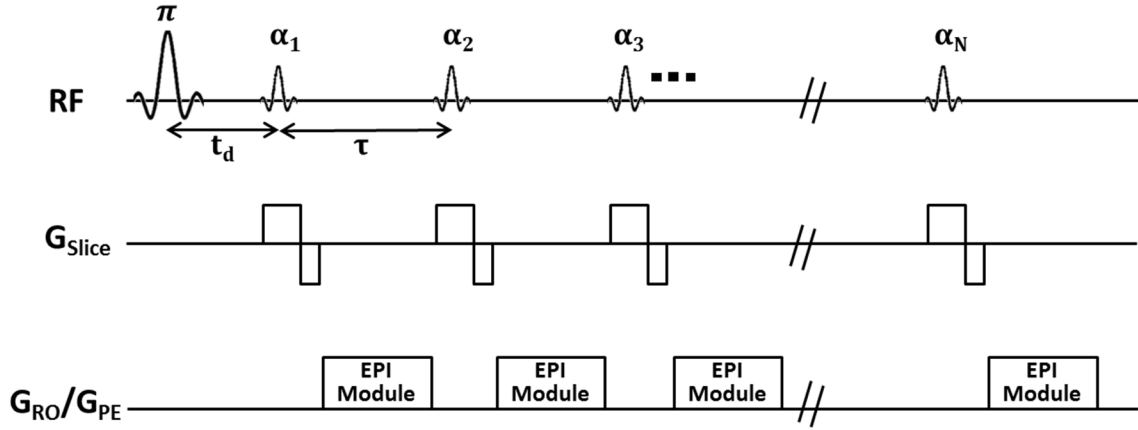
Figure A.1 Pulse sequence diagram for HMDSO-selective oximetry using PISTOL-LL. The sequence consists of a frequency-selective π inversion recovery preparation pulse, followed by N = 55 α = 5º pulses (also HMDSO selective), with a delay τ = 1s between two successive αº pulses. An EPI readout follows each αº pulse, enabling a linear sampling of the magnetization recovery curve within the same TR (55 s).

Both the PISTOL and PISTOL-LL datasets were processed offline using home-built algorithms in Matlab to compute T_1, R_1 (=1/T_1), and pO$_2$ maps using calibration curves corresponding to PISTOL and PISTOL-LL at 7 T, respectively (Figure A.2 (a)) on a voxel-by-voxel basis. For the PISTOL measurements, the T_1 values were computed for each voxel by appling a three-parameter least-squares curve fit to the measured signal intensities from 16 τ values using the Levenberg-Marquardt algorithm.

For the PISTOL-LL measurements, the curve-fitting procedure corresponding to inversion recovery was applied to the measured signal intensities from 55 τ values, for each voxel. A three parameter fit was applied to the recovery curve $M(t) = A - Bexp(-t/T_1^*)$ to obtain A, B, and T_1*. It is difficult to directly obtain T_1 from T_1* as the RF coil profile and B$_1$ field inhomogeneities lead to imperfections in the flip angle α at each pixel location, causing it to differ within the sample [213, 214]. When α is small (5º in our experiments), $T_1 = T_1^*(B/A - 1)$ can be employed to correct for the longitudinal

146

relaxation time [214]. Lastly, the R_1 maps from both sequences were then converted into pO_2 maps using the calibration curves for HMDSO at 7 T.

In Vitro Calibration and Phantom Experiments

For the calibration experiments, a second phantom consisting of four gas-tight John Young NMR tubes (Wilmad Labglass, Buena, NJ, USA) was constructed. Each of these four tubes housed 1 ml of HMDSO bubbled with different concentrations of oxygen (0%, 5%, 10%, and 21% calibrated gases). The phantom was placed on a warm heating pad connected to a circulating water bath and the temperature was monitored using a fiber-optic temperature probe (FISO Technologies Inc., Quebec City, Quebec, Canada). Both the PISTOL and PISTOL-LL sequences were run to obtain the calibration constants for HMDSO at 7 T. Mean T_1 values were measured from the region of interest corresponding to each tube. Mean R_1 values were obtained from repeated measurements and plotted versus pO_2 to generate the calibration curve for HMDSO.

A test phantom was constructed to evaluate and optimize the PISTOL-LL oximetry sequence. The phantom consisted of three tubes containing HMDSO, mineral oil (to represent fat), and water. A 5 mm NMR tube containing HMDSO was placed inside a 15 mm tube containing mineral oil, and this setup was in turn placed inside a larger 50 ml tube housing deionized (DI) water; all three tubes were tightly sealed to ensure no leakage. Both the PISTOL and PISTOL-LL oximetry sequences were tested on the phantom to compare the ability to selectively excite the HMDSO resonance, while suppressing the peaks from water and fat. R_1 maps were generated from the T_1 maps that were obtained by fitting the data on a pixel-by-pixel basis as described previously. The

147

mean T_1 (and R_1) values over the region of interest were obtained and the pO_2 values over the selected region were subsequently calculated using the calibration constants obtained as described above.

In Vivo Experiments

Approval was obtained from the Institutional Animal Care and Use committee of Arizona State University for all *in vivo* experiments. A cohort of six (n = 6) healthy Fischer F344 rats was used for the pO_2 experiments. The rats were anesthesized via isoflurane gas inhalation (air and 2% isoflurane) and remained passively restrained during the imaging experiment. 30-50 µL of HMDSO was injected along two to three directions in the same plane into the left thigh muscle of each rat for the *in vivo* pO_2 measurements. A 72 mm volume transmit coil combined with a surface receive coil was employed for the *in vivo* studies. The rats were placed in a prone position inside the magnet and the left thigh muscle along with the hind leg was carefully positioned under the surface coil. The rats were kept warm by placing them on a heating pad connected to a circulating water bath operating at 37º C.

A siloxane-selective echo planar imaging (EPI) sequence was initially used to locate the reporter molecule and a cross section through the thigh at the desired slice location was subsequently imaged. The rats were subjected to respiratory challenge by supplying air (~20 min) – oxygen (~30 min) – air (~30 min), as employed previously [208], to introduce modulation in the tissue oxygenation. A set of T_1 datasets was collected every 5 min by running both the PISTOL (3 min 45 s) and PISTOL-LL imaging (55 s) sequences in an interleaved manner. The datasets were processed offline using in

148

house Matlab fitting routines to generate pO_2 maps from the R_1 values. Sixteen pO_2 maps were obtained for each of the PISTOL and PISTOL-LL oximetry sequences over a time interval of ~80 minutes.

A.3   Results

Phantom Experiments

Figures A.2 and A.3 illustrate the results from the phantom experiments. The PISTOL-LL sequence was able to successfully eliminate the signals from water and mineral oil as well as the siloxane-selective spin-echo and PISTOL sequences. A linear fit to the pO_2 calibration phantom data from the PISTOL sequence generated a calibration curve $R_1 = (0.125 \pm 0.001) + (0.109 \pm 0.002) X10^{-2}$ x pO_2 while that from the PISTOL-LL sequence generated a calibration curve $R_1 = (0.124 \pm 0.002) + (0.113 \pm 0.004) X10^{-2}$ x pO_2 at 37 °C at 7 T, as illustrated in Figure A.2 (a).

As seen from the figure, both sequences generate similar calibration constants for neat HMDSO at 7 T. In Figures A.2 (c), A.2 (d), and A.2 (e), the SNR of HMDSO was 356.96 (siloxane-selective spin echo sequence), 1600 (PISTOL at TR = 55 s), and 88.59 (PISTOL-LL at TR = 55 s), respectively. The CNR for the frequency selective images in Figures A.2 (c), A.2 (d), and A.2 (e) with respect to water was calculated to be 343.29, 1597.4, and 85.16, respectively, while that with respect to fat was determined to be 337.17, 1573.7, and 83.78, respectively.

(a)

T₁-weighted image of the phantom **(b)**   HMDSO-selective spin-echo image **(c)**
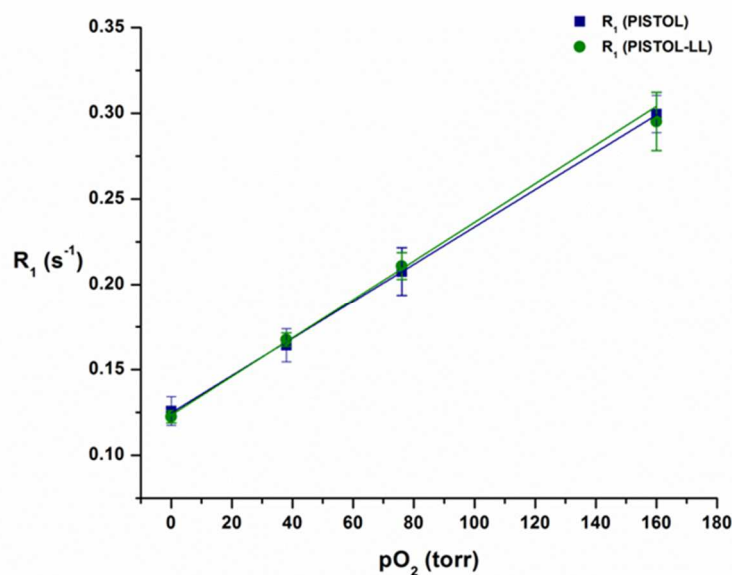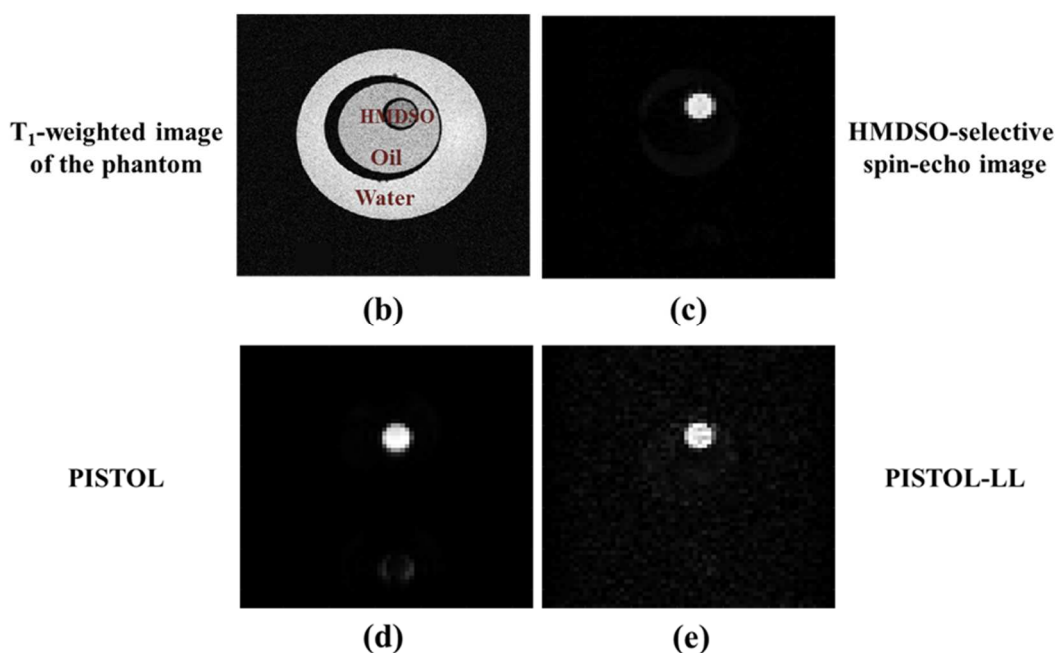
PISTOL **(d)**   PISTOL-LL **(e)**

Figure A.2 Comparison of calibration curves and siloxane selectivity between PISTOL and PISTOL-LL. **(a)** The calibration curve obtained from a linear fit of the PISTOL data is given by $R_1 = (0.125 \pm 0.001) + (0.00109 \pm 0.00002) \times pO_2$, while that from the PISTOL-LL sequence is given by $R_1 = (0.124 \pm 0.002) + (0.00113 \pm 0.00004) \times pO_2$ at 37 °C and 7 T. **(b)** Phantom consisting of sealed tubes of water/oil/HMDSO. HMDSO images from the **(c)** frequency-selective spin-echo sequence, **(d)** PISTOL (TR=55s), and **(e)** PISTOL-LL (TR=55s) show complete fat and water suppression.
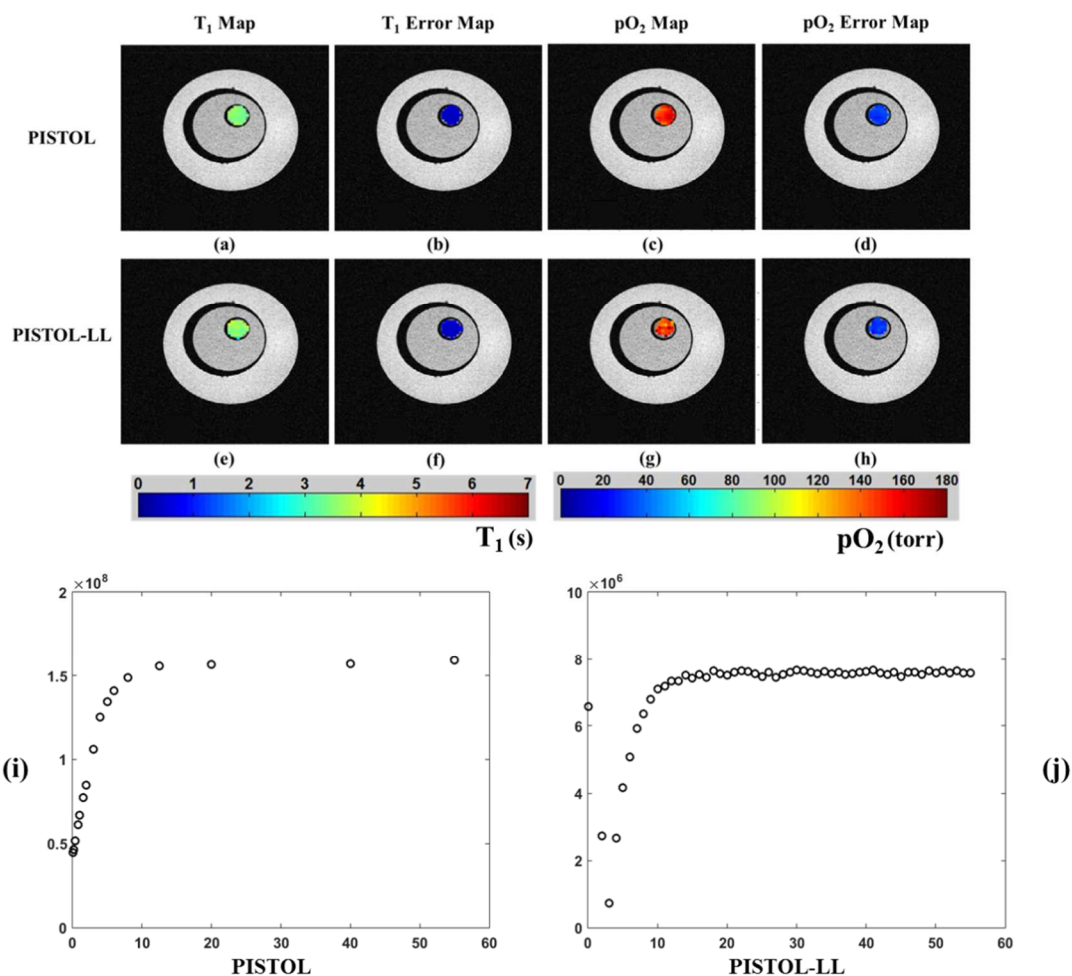
Figure A.3 PISTOL and PISTOL-LL sequences run on the water/oil/HMDSO phantom: T_1 maps in (a) and (e), and T_1 error maps in (b) and (f) for the PISTOL and PISTOL-LL sequences, respectively. Figures (c) and (g) depict the corresponding pO_2 maps and the pO_2 error maps for **(d)** PISTOL and **(h)** PISTOL-LL, respectively. The magnetization recovery curves from the two sequences are depicted in **(i)** and **(j)** for PISTOL (saturation-recovery) and PISTOL-LL (inversion recovery), respectively.

     PISTOL and PISTOL-LL sequences were both run on the water/mineral oil/HMDSO phantom described earlier to map the T_1 of HMDSO and the results obtained at 7 T are as illustrated in Figure A.3. The mean T_1 of HMDSO in air i.e. 21% oxygen concentration at 7 T determined from the PISTOL sequence is 3.47 ± 0.12 s, while that

from the PISTOL-LL sequence is 3.61 ± 0.29 s. The mean T_1 error from the PISTOL fit routine is 0.41 ± 0.05 s, while that from PISTOL-LL is 0.46 ± 0.13 s. The mean pO_2 as determined from the PISTOL sequence is 150.6 ± 8.8 torr, while that from the PISTOL-LL sequence is 145.6 ± 22.7 torr. The resulting pO_2 error from the PISTOL fit was found to be 31.43 ± 2.62 torr, while that from the PISTOL-LL sequence was 30.09 ± 2.62 torr.

In Vivo Studies

HMDSO was readily detected by both the PISTOL and PISTOL-LL sequences, along with complete fat and water suppression *in vivo*, as seen in Figure A.4. Frequency-selective spin-echo and EPI sequences were initially employed to identify the distribution of the HMDSO reporter molecule, as seen in Figure A.4 (b). In Figures A.4 (b), A.4 (c), and A.4 (d), the SNR of HMDSO was 541.31 (siloxane-selective spin echo sequence), 407.98 (PISTOL at TR = 55 s), and 23.37 (PISTOL-LL at TR = 55 s), respectively. The T_1 and pO_2 maps generated from the data acquired by the PISTOL and PISTOL-LL sequences show the same distribution of HMDSO, as illustrated in Figure A.5. The effect of breathing oxygen on the changes in the muscle pO_2 was evaluated during the *in vivo* experiments for both the sequences under consideration. In the rat thigh muscle (n = 6), the baseline pO_2 value for the imaging data recorded using the PISTOL sequence ranged from 41 to 78 torr (mean 58 ± 10 torr), while the baseline pO_2 value for the data acquired by the PISTOL-LL sequence ranged from 40 to 76 torr (mean 59 ± 9 torr) within the pooled cohort.

A significant increase ($p < 0.05$, compared to baseline) in the pO_2 values was recorded by the first measurement (5 min) after the gas inhaled by the rats was switched

to 100% oxygen breathing; the pO_2 values continued to rise over a 30 minute time interval during which pure oxygen was supplied. At the end of 30 minutes of oxygen breathing, the pO_2 values ranged from 112 to 284 torr (mean 192 ± 66 torr) as recorded by the PISTOL sequence, while those for the PISTOL-LL sequence ranged from 86 to 277 torr (mean 184 ± 67 torr). When the inhaled gas was switched back to air, a rapid drop in the pO_2 values was observed (as expected), with the detected values settling down to near baseline measurements after approximately 30 minutes of switching back to air breathing. At the end of the last 30 minute interval, the pO_2 values recorded by the PISTOL sequence ranged from 63 to 82 torr (mean 74 ± 8 torr), while the pO_2 measurements mapped by the PISTOL-LL sequence ranged from 70 to 86 torr (mean 76 $\pm$ 6 torr). Figure A.6 shows the mean pO_2 values mapped from the PISTOL and PISTOL-LL sequences for the entire time course of air – oxygen - air breathing over a time interval of ~80 minutes.
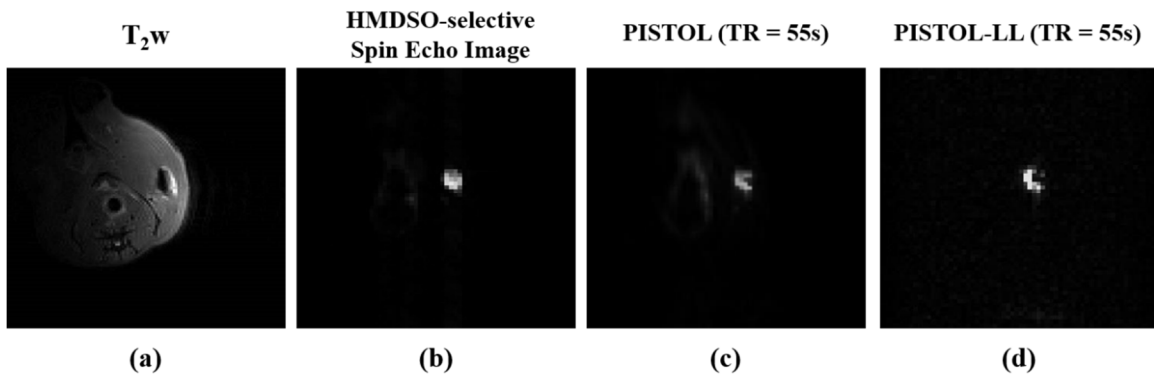
Figure A.4 HMDSO-selective oximetry *in vivo* **(a)** T_2-weighted image of a representative rat thigh muscle, **(b)** Frequency-selective spin-echo image of the HMDSO injected into the thigh muscle, **(c)** PISTOL image at TR = 55s, and **(d)** PISTOL-LL image at TR = 55s.
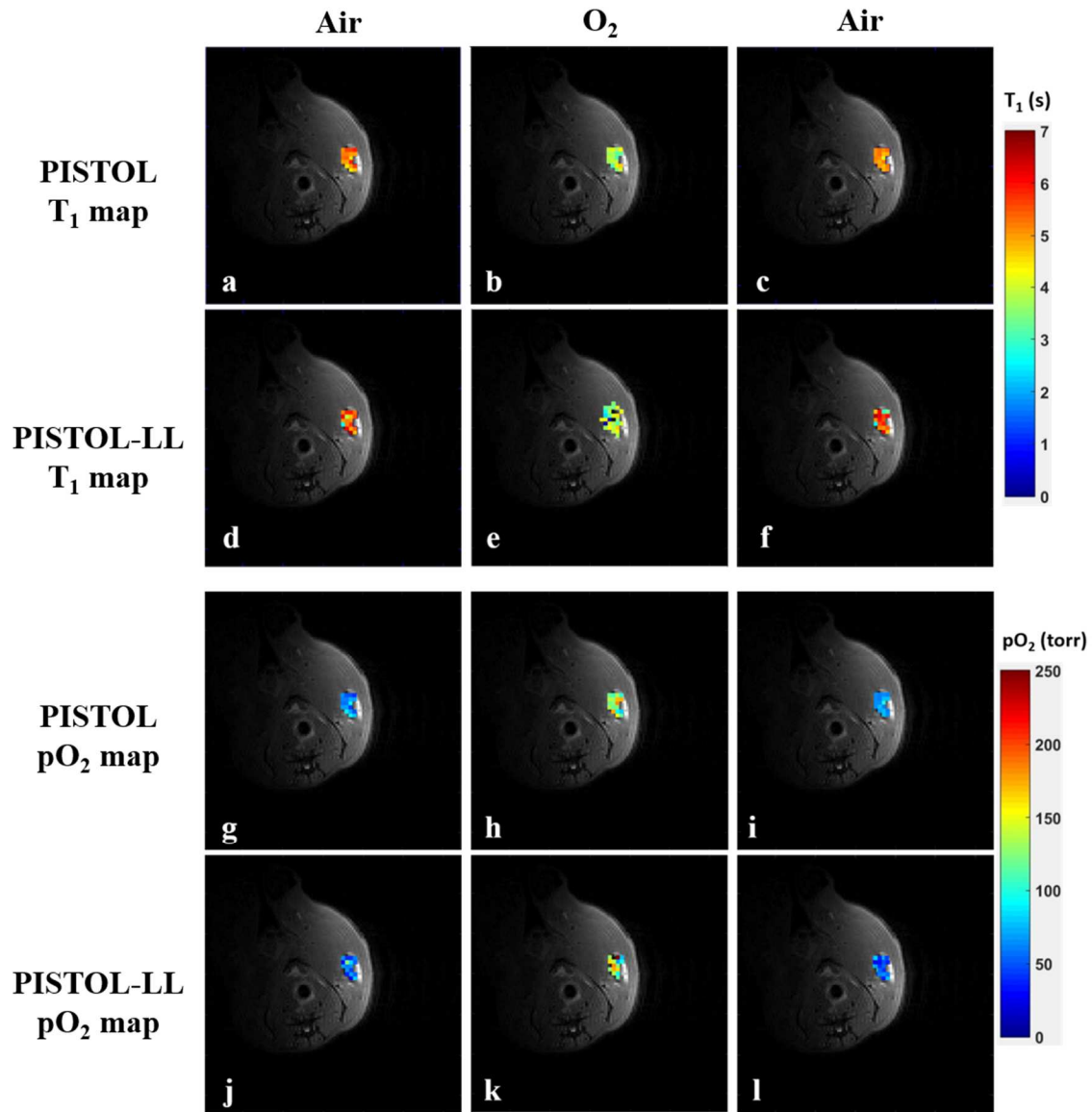
Figure A.5 T_1 and pO_2 maps from PISTOL and PISTOL-LL. Time course PISTOL (**a**, **b**, **c**) and PISTOL-LL (**d**, **e**, **f**) T_1 maps, respectively, in response to gas intervention: baseline air breathing (**a**, **d**), after 30 mins of oxygen breathing (**b**, **e**), and 30 mins after returning to breathing air (**c**, **f**). Corresponding time course PISTOL (**g**, **h**, **i**) and PISTOL-LL (**j**, **k**, **l**) pO_2 maps, respectively, in response to gas intervention: baseline air breathing (**g**, **j**), after 30 mins of oxygen breathing (**h**, **k**), 30 mins after returning back to breathing air (**i**. **l**).
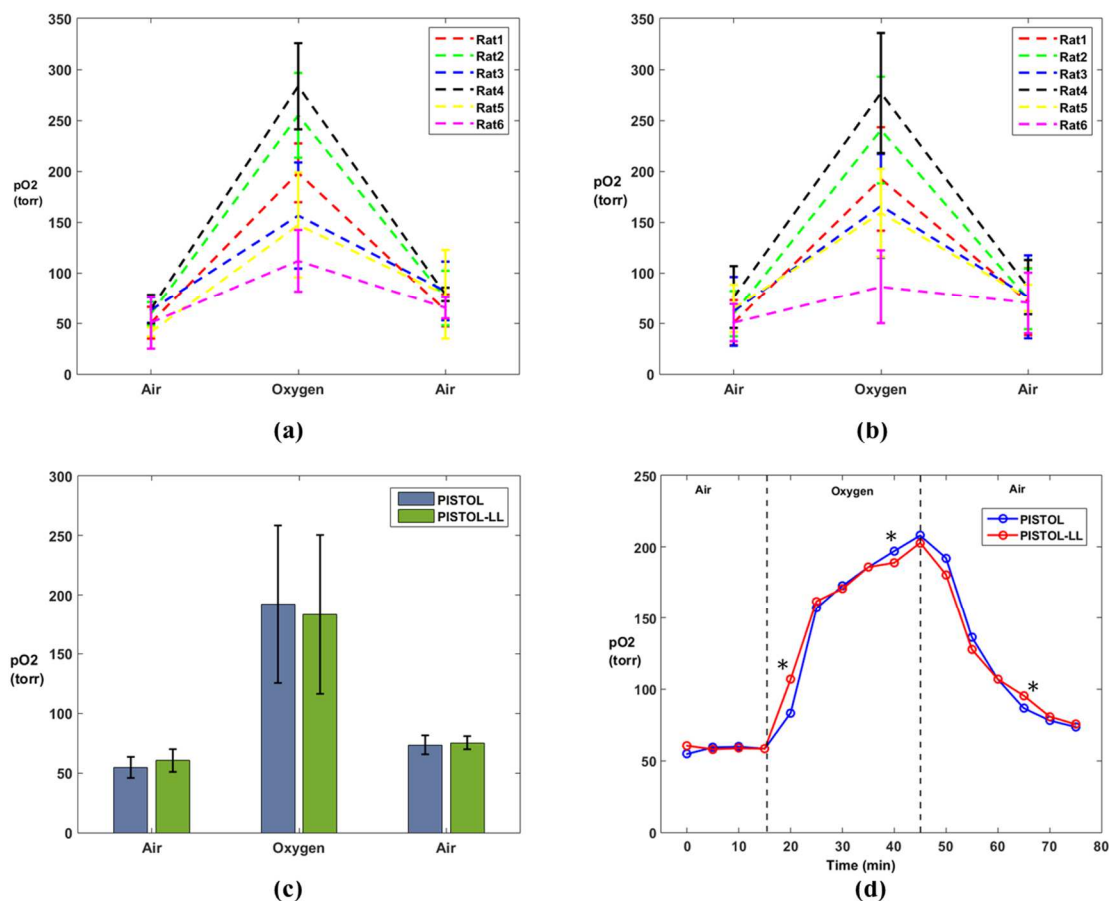
Figure A.6 Dynamic changes in the rat thigh muscle pO2 values in response to gas intervention – (**a**) From PISTOL, and (**b**) From the PISTOL-LL sequence. The three time points depicted correspond to the start of air breathing, 30 mins after switching to oxygen breathing, and 30 mins after switching back to air. (**c**) Mean pO_2 values for all the rats (n=6) over the time course air-O_2-air. The two methods give similar results (p > 0.05) when compared under air and oxygen. (**d**) Mean pO_2 values for all the rats (n=6) over the entire 80 min time course air (20 min) - O_2 (30 mins) – air (20 mins). (* = p < 0.05 between PISTOL and PISTOL-LL measurements).

A.4 Discussion & Conclusions

PISTOL-LL, enables T_1 and subsequently pO_2 mapping of the HMDSO ^{1}H resonance in under one minute at 7 T. This results in the speeding-up of ^{1}H MR tissue oximetry by ~4X compared to PISTOL. The new oximetry technique could be particularly useful as the T_1 of HMDSO ranges from ~2.5 s (160 torr, hyperoxic

conditions) to ~11 s (0 torr, anoxic conditions). This results in relatively long scan times in MR oximetry as the minimum TR for the pulse sequence has to be chosen to equal at least five times the T_1 of the reporter molecule under investigation. PISTOL-LL will also further accelerate the mapping of tissue pO_2 changes when using siloxanes with T_1 recovery times that are shorter than HMDSO.

The results demonstrate that both the PISTOL and PISTOL-LL sequences give statistically similar ($p > 0.05$) results during baseline air breathing and at the end of the 30 minute interval after switching the inhaled gas back to air. The mean pO_2 values recorded by both these sequences were slightly different in the 30 minute time interval when the rats were subjected to 100% oxygen breathing. This difference in mean pO_2 values is expected as both sequences were run in an interleaved manner and the dynamic changes in the muscle pO_2 at any particular instant cannot be captured by both sequences simultaneously. However, it is fair to expect comparable mean pO_2 values from the two sequences at the beginning (during 20 minutes of baseline air breathing) and end (30 minutes after return to air breathing) of the experiment. This is indeed the case as discussed before and is illustrated in Figures A.6 (a) – A.6 (d).

There are minor differences in the T_1 values measured by the two sequences under consideration also due to the fact that the data is acquired using two separate sequences that employ two different recovery mechanisms - PISTOL is essentially a saturation recovery T_1 mapping sequence while PISTOL-LL samples the inversion recovery curve using small flip angle pulses to achieve T_1 mapping. The datasets acquired by the two sequences differ in SNR with the PISTOL-LL sequence having lower SNR due to the low tip angle excitation pulses ($\alpha = 90^{\circ}$ for PISTOL and a series of

α = 5° pulses for PISTOL-LL). The PISTOL-LL selective images at TR = 55s (Figures A.2 (e) and A.4 (d)) have a SNR that is ~18x lower than that of the corresponding PISTOL images (Figures A.2 (d) and A.4 (c)). Different fit routines employed to post process the datasets from the two sequences also contribute to minor differences in the reported T_1, R_1, and pO_2 values. However, the T_1 values from both fit routines are very similar, with only minor differences even in the curve fit errors, as noted previously in the results. This suggests that the PISTOL-LL sequence achieves accurate T_1 (and pO_2) mapping that is comparable to the PISTOL sequence, in spite of having an ~18x lower SNR.

It has been demonstrated that the new oximetry sequence PISTOL-LL has an improved performance with the PISTOL sequence; PISTOL-LL preserves the fidelity of the acquired relaxometry data, while accelerating data acquisition by ~4X. PISTOL-LL could be employed to image other siloxanes [215] that offer superior performance and have shorter T_1 relaxation times as compared to HMDSO, thus, resulting in even faster acquisition times in MR oximetry. This sequence also has applications for *in vivo* tumor hypoxia imaging using nitromidazole-based T_1 contrast agents like GdDO3NI [216, 217] to aid in validation. This technique could potentially be translated to the clinic, given the availability of state-of-the-art MR hardware and excellent fat and water suppression routines in clinical scanners.

Furthermore, PISTOL-LL can also be adopted in ^{19}F tissue oximetry [195, 196, 218-222] with minor modifications. Perfluorocarbons (PFCs) have been employed in ^{19}F NMR to quantitate the pO_2, using the reporter molecule hexaflurobenzene (HFB) [195, 218, 223, 224], wherein the R_1 of these PFC nano emulsions exhibits a linear dependence

157

on the pO_2. Cell labeling and tracking in the past few years has also been successfully achieved using PFC nano emulsions [192, 225-228]. PISTOL-LL can thus facilitate fast and dynamic pO_2 mapping in various tracking and cellular labeling applications, such as those in neural stem cells, in both ^{19}F and ^{1}H oximetry studies involving dual-modality MRI-fluorescence probes [190, 191, 229]. Given the speed of acquisition, the PISTOL-LL sequence can be easily incorporated into existing clinical protocols, thus, providing a valuable tool for fast quantitative oximetry.

In summary, a fast MRI pulse sequence based on the Look-Locker approach was presented for accelerating the acquisition of T_1 datasets in ^{1}H MR tissue oximetry. The new oximetry sequence, PISTOL-LL, enables rapid T_1 and pO_2 mapping of the HMDSO reporter molecule in less than one minute, resulting in a four-fold acceleration as compared to PISTOL. The PISTOL-LL technique can serve as a faster tool for probing oxygen dynamics in tissue oximetry studies.

APPENDIX B

TABLES FROM CHAPTER 4

This section includes tables containing patient demographic information and MRI/MRSI parameters for the 20 pediatric brain MRSI cases discussed in Chapter 4.

Table B.1 Patient demographics and related information from MRI and MRSI for 14 non-tumor pediatric cases, scanned for other brain related concerns. (WM - white matter, NAA – N-acetyl aspartate, Cr – creatine, Cho – choline, Lac – lactate)

Case	Gender	Age (years)	Reason for MRI	NAA/Cr (Mean ± SD)	Cho/NAA (Mean ± SD)	Cho/Cr (Mean ± SD)
1	M	5	optic atrophy, hypoplasia of anterior corpus callosum and optic nerves	1X: 1.85 ± 1.30 2X: 1.88 ± 1.78 3X: 1.84 ± 1.17 4X: 1.90 ± 1.23 5X: 1.95 ± 1.42	1X: 0.40 ± 0.34 2X: 0.40 ± 0.35 3X: 0.44 ± 0.54 4X: 0.40 ± 0.35 5X: 0.36 ± 0.15	1X: 0.55 ± 0.14 2X: 0.55 ± 0.15 3X: 0.54 ± 0.15 4X: 0.55 ± 0.15 5X: 0.59 ± 0.14
2	M	1	seizures	1X: 2.44 ± 1.74 2X: 2.45 ± 1.85 3X: 2.56 ± 2.36 4X: 2.46 ± 1.83 5X: 2.60 ± 2.20	1X: 0.55 ± 0.42 2X: 0.54 ± 0.46 3X: 0.57 ± 0.54 4X: 0.59 ± 0.59 5X: 0.57 ± 0.52	1X: 0.91 ± 0.24 2X: 0.87 ± 0.20 3X: 0.89 ± 0.22 4X: 0.91 ± 0.27 5X: 0.98 ± 0.26
3	F	16	concussion	1X: 1.80 ± 1.43 2X: 1.91 ± 1.90 3X: 1.80 ± 1.39 4X: 2.00 ± 1.84 5X: 1.71 ± 1.10	1X: 0.61 ± 0.41 2X: 0.62 ± 0.40 3X: 0.60 ± 0.39 4X: 0.64 ± 0.40 5X: 0.61 ± 0.37	1X: 0.72 ± 0.15 2X: 0.76 ± 0.24 3X: 0.76 ± 0.23 4X: 0.81 ± 0.30 5X: 0.77 ± 0.24

Case	Gender	Age (years)	Reason for MRI	NAA/Cr (Mean ± SD)	Cho/NAA (Mean ± SD)	Cho/Cr (Mean ± SD)
4	M	4	Rathke's cleft cyst or pituitary macroadenoma	1X: 2.25 ± 2.00 2X: 2.48 ± 2.31 3X: 2.62 ± 2.87 4X: 2.55 ± 2.50 5X: 2.45 ± 2.13	1X: 0.40 ± 0.19 2X: 0.36 ± 0.14 3X: 0.35 ± 0.14 4X: 0.35 ± 0.14 5X: 0.34 ± 0.15	1X: 0.67 ± 0.19 2X: 0.67 ± 0.22 3X: 0.65 ± 0.16 4X: 0.65 ± 0.17 5X: 0.65 ± 0.16
5	F	3	neurofibromatosis type 1 and lesion in optic pathway/chiasm	1X: 2.79 ± 1.19 2X: 2.84 ± 1.19 3X: 2.82 ± 1.16 4X: 2.81 ± 1.13 5X: 2.80 ± 1.07	1X: 0.55 ± 0.69 2X: 0.53 ± 0.62 3X: 0.47 ± 0.32 4X: 0.46 ± 0.33 5X: 0.63 ± 0.47	1X: 1.10 ± 0.39 2X: 1.12 ± 0.44 3X: 1.12 ± 0.48 4X: 1.10 ± 0.41 5X: 1.12 ± 0.42
6	F	9	seizures, temporal arachnoid cyst	1X: 2.40 ± 1.17 2X: 2.47 ± 1.47 3X: 2.44 ± 1.36 4X: 2.60 ± 1.76 5X: 2.83 ± 2.26	1X: 0.47 ± 0.18 2X: 0.46 ± 0.19 3X: 0.47 ± 0.20 4X: 0.45 ± 0.19 5X: 0.43 ± 0.19	1X: 1.00 ± 0.25 2X: 0.95 ± 0.25 3X: 0.96 ± 0.25 4X: 0.93 ± 0.20 5X: 0.92 ± 0.20
7	F	10	encephalopathy	1X: 2.49 ± 1.33 2X: 2.70 ± 1.70 3X: 2.69 ± 1.46 4X: 2.70 ± 1.62 5X: 2.65 ± 1.35	1X: 0.44 ± 0.46 2X: 0.38 ± 0.19 3X: 0.37 ± 0.14 4X: 0.37 ± 0.14 5X: 0.38 ± 0.14	1X: 0.87 ± 0.33 2X: 0.84 ± 0.25 3X: 0.84 ± 0.20 4X: 0.85 ± 0.20 5X: 0.83 ± 0.20

Case	Gender	Age (years)	Reason for MRI	NAA/Cr (Mean ± SD)	Cho/NAA (Mean ± SD)	Cho/Cr (Mean ± SD)
8	M	4	neurofibromatosis type 1 - von Recklinghausen's disease	1X: 2.58 ± 1.91 2X: 2.82 ± 2.40 3X: 2.95 ± 2.73 4X: 2.87 ± 2.30 5X: 2.83 ± 2.37	1X: 0.34 ± 0.17 2X: 0.33 ± 0.18 3X: 0.35 ± 0.17 4X: 0.40 ± 0.16 5X: 0.38 ± 0.19	1X: 0.66 ± 0.11 2X: 0.66 ± 0.13 3X: 0.63 ± 0.14 4X: 0.60 ± 0.11 5X: 0.55 ± 0.12
9	F	3	incomplete whitel matter myelination in subcortical areas	1X: 1.90 ± 0.65 2X: 1.89 ± 0.64 3X: 1.89 ± 0.63 4X: 1.91 ± 0.64 5X: 1.89 ± 0.61	1X: 0.49 ± 0.14 2X: 0.48 ± 0.15 3X: 0.47 ± 0.15 4X: 0.47 ± 0.14 5X: 0.47 ± 0.15	1X: 0.85 ± 0.16 2X: 0.83 ± 0.16 3X: 0.82 ± 0.15 4X: 0.83 ± 0.13 5X: 0.82 ± 0.12
10	F	1.1	Moyamoya disease	1X: 1.57 ± 0.33 2X: 1.61 ± 0.35 3X: 1.63 ± 0.32 4X: 1.63 ± 0.32 5X: 1.66 ± 0.34	1X: 0.62 ± 0.15 2X: 0.62 ± 0.14 3X: 0.61 ± 0.12 4X: 0.60 ± 0.11 5X: 0.56 ± 0.09	1X: 0.93 ± 0.13 2X: 0.95 ± 0.13 3X: 0.96 ± 0.13 4X: 0.86 ± 0.14 5X: 0.90 ± 0.12
11	F	7	Rathke's cleft cyst near the pituitaries	1X: 3.06 ± 2.66 2X: 3.12 ± 3.08 3X: 3.17 ± 2.59 4X: 3.42 ± 3.04 5X: 3.42 ± 3.35	1X: 0.41 ± 0.39 2X: 0.39 ± 0.38 3X: 0.40 ± 0.41 4X: 0.38 ± 0.26 5X: 0.37 ± 0.26	1X: 0.89 ± 0.16 2X: 0.88 ± 0.21 3X: 0.88 ± 0.22 4X: 0.85 ± 0.19 5X: 0.78 ± 0.20

Case	Gender	Age (years)	Reason for MRI	NAA/Cr (Mean ± SD)	Cho/NAA (Mean ± SD)	Cho/Cr (Mean ± SD)
12	M	0.5	Tuberous sclerosis	1X: 2.07 ± 1.04 2X: 2.20 ± 1.38 3X: 2.34 ± 1.77 4X: 2.45 ± 2.21 5X: 2.45 ± 2.16	1X: 0.89 ± 1.19 2X: 0.80 ± 0.82 3X: 0.71 ± 0.41 4X: 0.72 ± 0.52 5X: 0.71 ± 0.41	1X: 1.24 ± 0.17 2X: 1.27 ± 0.21 3X: 1.28 ± 0.22 4X: 1.28 ± 0.23 5X: 1.29 ± 0.24
13	M	2.5	decreased WM volume, demyelination	1X: 1.33 ± 0.42 2X: 1.33 ± 0.40 3X: 1.31 ± 0.39 4X: 1.31 ± 0.37 5X: 1.31 ± 0.36	1X: 0.69 ± 0.22 2X: 0.69 ± 0.23 3X: 0.70 ± 0.24 4X: 0.69 ± 0.22 5X: 0.70 ± 0.22	1X: 0.84 ± 0.12 2X: 0.85 ± 0.13 3X: 0.84 ± 0.12 4X: 0.84 ± 0.11 5X: 0.84 ± 0.13
14	M	3 day	posterior parietal cephalohematoma	1X: 1.54 ± 1.80 2X: 1.45 ± 2.21 3X: 1.32 ± 1.51 4X: 1.26 ± 1.12 5X: 1.36 ± 1.47	1X: 2.01 ± 2.62 2X: 2.25 ± 3.15 3X: 2.28 ± 3.47 4X: 2.26 ± 3.48 5X: 2.28 ± 3.13	1X: 1.55 ± 0.63 2X: 1.67 ± 1.09 3X: 1.66 ± 0.91 4X: 1.65 ± 0.90 5X: 1.58 ± 0.72

Table B.2 Patient demographics and related information from MRI and MRSI for 6 pediatric cases with brain tumors (includes resected cases). (NAA – N-acetyl aspartate, Cr – creatine, Cho – choline, Lac – lactate)

Case	Gender	Age (years)	Reason for MRI	NAA/Cr (Mean ± SD)	Cho/NAA (Mean ± SD)	Cho/Cr (Mean ± SD)
1	M	10	Ewing's sarcoma	1X: 1.73 ± 0.55 1.48 ± 0.41 (Tumor) 3.37 ± 2.87 (Lac/Cr) 2X: 1.73 ± 0.6 1.53 ± 0.51 (Tumor) 3.48 ± 3.21 (Lac/Cr) 3X: 1.71 ± 0.52 1.62 ± 0.45 (Tumor) 4.05 ± 3.38 (Lac/Cr) 4X: 1.7 ± 0.51 1.62 ± 0.44 (Tumor) 4.09 ± 4.08 (Lac/Cr) 5X: 1.71 ± 0.48 1.45 ± 0.25 (Tumor) 2.87 ± 2.25 (Lac/Cr)	1X: 0.60 ± 0.58 0.77 ± 0.39 (Tumor) 2.31 ± 1.95 (Lac/NAA) 2X: 0.60 ± 0.38 0.79 ± 0.40 (Tumor) 2.23 ± 1.88 (Lac/NAA) 3X: 0.58 ± 0.46 0.81 ± 0.31 (Tumor) 2.23 ± 2.00 (Lac/NAA) 4X: 0.57 ± 0.38 0.81 ± 0.30 (Tumor) 2.23 ± 2.03 (Lac/NAA) 5X: 0.53 ± 0.26 0.83 ± 0.33 (Tumor) 2.11 ± 1.68 (Lac/NAA)	1X: 0.82 ± 0.25 1.06 ± 0.36 (Tumor) 3.00 ± 2.49 (Lac/Cho) 2X: 0.84 ± 0.30 1.12 ± 0.43 (Tumor) 2.88 ± 2.68 (Lac/Cho) 3X: 0.90 ± 0.48 1.37 ± 0.86 (Tumor) 2.72 ± 2.30 (Lac/Cho) 4X: 0.89 ± 0.49 1.38 ± 0.88 (Tumor) 2.36 ± 1.40 (Lac/Cho) 5X: 0.85 ± 0.32 1.19 ± 0.49 (Tumor) 2.17 ± 1.12 (Lac/Cho)
2	M	13	meningioma	1X: 2.73 ± 2.44 2X: 2.29 ± 2.48 3X: 3.22 ± 3.13 4X: 3.17 ± 3.90 5X: 3.28 ± 3.95	1X: 0.71 ± 0.79 2X: 0.68 ± 0.80 3X: 0.62 ± 0.60 4X: 0.57 ± 0.34 5X: 0.53 ± 0.35	1X: 1.08 ± 0.35 2X: 1.12 ± 0.49 3X: 1.10 ± 0.35 4X: 1.10 ± 0.38 5X: 1.20 ± 0.40

Case	Gender	Age (years)	Reason for MRI	NAA/Cr (Mean ± SD)	Cho/NAA (Mean ± SD)	Cho/Cr (Mean ± SD)
3	M	1.5	hemophagocytic lymphohistiocytosis	1X: 1.72 ± 0.47 1.42 ± 0.45 (Tumor) 0.80 ± 0.36 (Lac/Cr) 2X: 1.72 ± 0.48 1.41 ± 0.43 (Tumor) 0.76 ± 0.32 (Lac/Cr) 3X: 1.81 ± 0.52 1.40 ± 0.38 (Tumor) 0.78 ± 0.22 (Lac/Cr) 4X: 1.83 ± 0.51 1.39 ± 0.40 (Tumor) 0.75 ± 0.19 (Lac/Cr) 5X: 1.82 ± 0.52 1.38 ± 0.40 (Tumor) 0.73 ± 0.29 (Lac/Cr)	1X: 0.64 ± 0.30 1.20 ± 0.50 (Tumor) 0.63 ± 0.42 (Lac/NAA) 2X: 0.66 ± 0.32 1.23 ± 0.47 (Tumor) 0.59 ± 0.32 (Lac/NAA) 3X: 0.63 ± 0.32 1.25 ± 0.47 (Tumor) 0.60 ± 0.24 (Lac/NAA) 4X: 0.61 ± 0.31 1.24 ± 0.44 (Tumor) 0.59 ± 0.25 (Lac/NAA) 5X: 0.63 ± 0.32 1.23 ± 0.44 (Tumor) 0.53 ± 0.24 (Lac/NAA)	1X: 1.02 ± 0.32 1.60 ± 0.47 (Tumor) 0.49 ± 0.14 (Lac/Cho) 2X: 1.03 ± 0.31 1.61 ± 0.45 (Tumor) 0.46 ± 0.10 (Lac/Cho) 3X: 1.03 ± 0.29 1.61 ± 0.30 (Tumor) 0.49 ± 0.11 (Lac/Cho) 4X: 1.02 ± 0.29 1.58 ± 0.30 (Tumor) 0.47 ± 0.07 (Lac/Cho) 5X: 1.03 ± 0.30 1.57 ± 0.29 (Tumor) 0.47 ± 0.24 (Lac/Cho)
4	F	5	neurofibromatosis 1 and astrocytoma	1X: 1.36 ± 0.71 0.55 ± 0.38 (Lac/Cr) 2X: 1.32 ± 0.56 0.51 ± 0.35 (Lac/Cr) 3X: 1.32 ± 0.55 0.52 ± 0.41 (Lac/Cr) 4X: 1.35 ± 0.58 0.52 ± 0.43 (Lac/Cr) 5X: 1.27 ± 0.62 0.52 ± 0.47 (Lac/Cr)	1X: 1.29 ± 0.79 0.44 ± 0.26 (Lac/NAA) 2X: 1.19 ± 0.57 0.39 ± 0.18 (Lac/NAA) 3X: 1.18 ± 0.52 0.38 ± 0.17 (Lac/NAA) 4X: 1.16 ± 0.52 0.39 ± 0.28 (Lac/NAA) 5X: 1.10 ± 0.50 0.37 ± 0.28 (Lac/NAA)	1X: 1.33 ± 0.30 0.43 ± 0.34 (Lac/Cho) 2X: 1.32 ± 0.28 0.40 ± 0.29 (Lac/Cho) 3X: 1.32 ± 0.27 0.37 ± 0.17 (Lac/Cho) 4X: 1.30 ± 0.27 0.40 ± 0.29 (Lac/Cho) 5X: 1.25 ± 0.21 0.39 ± 0.25 (Lac/Cho)

Case	Gender	Age (years)	Reason for MRI	NAA/Cr (Mean ± SD)	Cho/NAA (Mean ± SD)	Cho/Cr (Mean ± SD)
5	F	10	left optic nerve glioma	1X: 1.56 ±1.73 2X: 1.42 ± 1.23 3X: 1.35 ± 0.70 4X: 1.45 ± 0.94 5X: 1.38 ± 0.62	1X: 0.66 ± 0.58 2X: 0.73 ± 0.67 3X: 0.77 ± 0.79 4X: 0.74 ± 0.85 5X: 0.76 ± 1.06	1X: 0.70 ± 0.18 2X: 0.70 ± 0.20 3X: 0.69 ± 0.19 4X: 0.67 ± 0.18 5X: 0.68 ± 0.14
6	M	3	grade 2 astrocytoma	1X: 2.18 ± 1.49 2X: 2.31 ± 1.95 3X: 2.19 ± 1.55 4X: 2.16 ± 1.54 5X: 2.18 ± 1.52	1X: 0.49 ± 0.18 2X: 0.48 ± 0.20 3X: 0.50 ± 0.25 4X: 0.51 ± 0.23 5X: 0.50 ± 0.24	1X: 0.86 ± 0.17 2X: 0.84 ± 0.17 3X: 0.83 ± 0.16 4X: 0.84 ± 0.20 5X: 0.82 ± 0.17

APPENDIX C

PUBLICATIONS & CONFERENCE ABSTRACTS

Journal Papers

(1) Addington CP, Cusick A, **Shankar RV**, Agarwal S, Stabenfeldt SE, and Kodibagkar VD, "Siloxane Nanoprobes for Labeling and Dual Modality Functional Imaging of Neural Stem Cells", *Annals of Biomedical Engineering*, **44**(3), 816-827, 2015.

Submitted Journal Papers

(1) **Shankar RV**, Chang JC, Hu HH, and Kodibagkar VD, "Fast Data Acquisition Techniques in Magnetic Resonance Spectroscopic Imaging" (*NMR in Biomedicine*, revisions in progress).

(2) Medina DX, Householder KT, Ceton R, Kovalik T, Heffernan, JM, **Shankar RV**, Bowser RP, Wechsler-Reya RJ, Sirianni RW, "Optical Barcoding Of PLGA for Multispectral Analysis of Nanoparticle Fate In Vivo" (*Journal of Controlled Release*).

(3) Chauhan M, **Shankar RV**, Kumar NA, Kodibagkar VD, and Sadleir R, "Multishot Echo-Planar MREIT for fast imaging of conductivity, current density and electric field distributions" (*Magnetic Resonance in Medicine*).

Journal Papers in Preparation

(1) **Shankar RV** and Kodibagkar VD, "A faster PISTOL for ^{1}H MR-based Quantitative Tissue Oximetry" (in submission to *NMR in Biomedicine*).

(2) **<u>Shankar RV</u>**, Hu HH, Chang JC, and Kodibagkar VD, "2D MR Spectroscopic Imaging of the Pediatric Brain using Compressed Sensing" (in preparation for submission to *Radiology*).

(3) **<u>Shankar RV</u>**, Agarwal S, and Kodibagkar VD, "Compressed Sensing Accelerated MR Spectroscopic Imaging of Lactate" (in preparation for submission to *Magnetic Resonance in Medicine*).

 (4) Agarwal S, Kozlowski T, **<u>Shankar RV</u>**, Inge LJ, and Kodibagkar VD, "MRI assessment of changes in tumor oxygenation post hypoxia-targeted therapy" (in preparation).

<div align="center">Conference Papers</div>

(1) **<u>Shankar RV</u>** and Kodibagkar VD, "A rapid Look-Locker imaging sequence for quantitative tissue oximetry", *Proceedings of the SPIE 9417,* Medical Imaging 2015: Biomedical Applications in Molecular, Structural, and Functional Imaging, 94170F 2015.

(2) **<u>Shankar RV</u>**, Agarwal S, Geethanath S, and Kodibagkar VD, "Rapid MR spectroscopic imaging of lactate using compressed sensing", *Proceedings of the SPIE 9417,* Medical Imaging 2015: Biomedical Applications in Molecular, Structural, and Functional Imaging, 94171J 2015.

(3) Agarwal S, **<u>Shankar RV</u>**, Inge LJ, and Kodibagkar VD, "MRI assessment of changes in tumor oxygenation post hypoxia-targeted therapy", *Proceedings of the SPIE 9417,* Medical Imaging 2015: Biomedical Applications in Molecular, Structural, and Functional Imaging, 941714 2015.

Conference Abstracts

(1) **Shankar RV**, Agarwal S, and Kodibagkar VD, "Rapid In Vivo MR Spectroscopic Imaging of Lactate using Compressed Sensing", *World Molecular Imaging Conference*, New York, September 7th-10th 2016. (Poster presentation)

(2) **Shankar RV**, Agarwal S, and Kodibagkar VD, "Compressed Sensing Accelerated MR Spectroscopic Imaging of Lactate", *International Society for Magnetic Resonance in Medicine*, Singapore, May 7th -13th 2016. (Oral presentation, *Magna Cum Laude*)

(3) **Shankar RV**, Hu HH, Chang JC, and Kodibagkar VD, "2D MR Spectroscopic Imaging of the Pediatric Brain using Compressed Sensing", *International Society for Magnetic Resonance in Medicine*, Singapore, May 7th -13th 2016. (E-Poster presentation)

(4) Agarwal S, Kozlowski T, **Shankar RV**, Inge LJ, and Kodibagkar VD, "MRI assessment of changes in tumor oxygenation post hypoxia-targeted therapy", *International Society for Magnetic Resonance in Medicine*, Singapore, May 7th -13th 2016.

(5) **Shankar RV** and Kodibagkar VD, "A Fast Look-Locker Imaging Technique for Quantitative Tissue Oximetry", *ISMRM*, Toronto, Canada, June 2015. (E-Poster presentation)

(6) **Shankar RV**, Agarwal S, Chang JC, and Kodibagkar VD, "Fast ^{1}H Magnetic Resonance Spectroscopic Imaging using Compressed Sensing", *GAP Conference*, Houston April 2015. (Poster presentation)

(7) Hemzacek K, **<u>Shankar RV</u>**, Hussain K, and Kodibagkar VD, "Development of a Temperature Sensitive MRI Contrast Agent", *BMES Annual Meeting*, San Antonio, Texas, October 22-25, 2014.

(8) Agarwal S, **<u>Shankar RV</u>**, Inge LJ, Smaill J, Patterson AV and Kodibagkar VD, "MRI assessment of changes in tumor oxygenation post hypoxia-targeted therapy", *World Molecular Imaging Conference*, Seoul Korea, September 17th-20th 2014.

(9) **<u>Shankar RV</u>**, Agarwal S, Geethanath S, and Kodibagkar VD, "Fast MR Spectroscopic Imaging of Lactate using Compressed Sensing", *Gordon In Vivo Magnetic Resonance*, Proctor Academy Andover NH, July 27th-Aug 1st 2014. (Poster presentation)

(10) Agarwal S, **<u>Shankar RV</u>**, Inge LJ, and Kodibagkar VD, "MRI assessment of changes in tumor oxygenation post hypoxia-targeted therapy", *Gordon In Vivo Magnetic Resonance*, Proctor Academy Andover NH, July 27th-Aug 1st 2014.

APPENDIX D

APPROVAL DOCUMENTS FOR STUDIES INVOLVING ANIMAL SUBJECTS

Office of Research Integrity and Assurance
Arizona State University
660 South Mill Avenue, Suite 315
Tempe, Arizona 85287-6111
Phone: (480) 965-4387 *FAX:* (480) 965-7772

Animal Protocol Review

ASU Protocol Number:	15-1433R
Protocol Title:	Probes for Imaging Tumor Vulnerability
Principal Investigator:	Vikram Kodibagkar
Date of Action:	04/23/2015

The animal protocol review was considered by the Committee and the following decisions were made:

The protocol was approved by Full Committee Review as presented.

If you have not already done so, documentation of Level III Training (i.e., procedure-specific training) will need to be provided to the IACUC office before participants can perform procedures independently. For more information on Level III requirements see https://researchintegrity.asu.edu/training/animals/levelthree.

Total # of Animals:	456		
Species:	Mice	**Pain Level:**	D-382
Species:	Rats	**Pain Level:**	D-74
Protocol Approval Period:	04/23/2015 – 04/22/2018		

Sponsor:	N/A
ASU Proposal/Award #:	N/A
Title:	N/A

Signature: *C. Johnson*
IACUC Chair or Designee

Date: 4/30/15

Cc: IACUC Office
        IACUC Chair

173

Institutional Animal Care and Use Committee (IACUC)
Office of Research Integrity and Assurance
Arizona State University
660 South Mill Avenue, Suite 315
Tempe, Arizona 85287-6111
Phone: (480) 965-4387 *FAX:* (480) 965-7772

Animal Protocol Review

ASU Protocol Number:	**15-1433R Amendment #1**
Protocol Title:	**Probes for Imaging Tumor Vulnerability**
Principal Investigator:	**Vikram Kodibagkar**
Date of Action:	**5/28/2015**

The animal protocol review was considered by the Committee and the following decisions were made:

The amendment was approved by Full Committee Review to add new procedures to the protocol.

If you have not already done so, documentation of Level III Training (i.e., procedure-specific training) will need to be provided to the IACUC office before participants can perform procedures independently. For more information on Level III requirements see https://researchintegrity.asu.edu/training/animals/levelthree.

Total # of Animals:	456	
Species:	Rats	Pain Level: D-74
Species:	Mice	Pain Level: D-382

Protocol Approval Period:	4/23/2015 – 4/22/2018

Sponsor:	N/A
ASU Proposal/Award #:	N/A
Title:	N/A

Signature: *Augustowski for C Johnson*   Date: 6/3/2015
IACUC Chair or Designee

Cc: IACUC Office
             IACUC Chair